Diss. ETH N° 20780

Design of ablation cells for LA-ICP-MS: from modeling to high spatial resolution analysis applications

A dissertation submitted to

ETH ZURICH

for the degree of

Doctor of Sciences (Dr. sc. ETH Zurich)

presented by

MATTIAS BENJAMIN FRICKER

Dipl. Chem., ETH Zurich

born 14. July 1981

citizen of Zug (ZG) and Zurich (ZH)

accepted on the recommendation of

Prof. Dr. Detlef Günther, examiner

Prof. Dr. Wendelin Stark, co-examiner

2012

Acknowledgements

First of all I would like to express my thanks to **Detlef Günther** for letting me work in his group on so many interesting projects and for guidance.

I would also like to thank Wendelin Stark for being the co-examiner of my thesis and for careful review of the manuscript.

ETH Zurich is acknowledged for funding and excellent equipment and a perfect environment to acquire my diploma and the doctorate.

The reviewers of my thesis chapters are thanked for valuable comments improving the manuscript:

Matthieu Brunner, Daniel Frick, **Daniel Tabersky**, **Paolo Garofalo**, **Sebastian Breitenbach**, **Julien Mercadier**, **Luca Flamigni**.

I'd like to thank **Roland Mäder** and the entire **ETH workshop team** for excellent work in building all versions and modifications of the large ablation cell that was developed in this study.

Beni Aeschlimann für Anleitung und Unterstützung.

The following persons are thanked for extraordinary collaboration:

Rolf Dietiker for the CFD modeling.

Daniel Kutscher for testing the ablation cell with electrophoresis gel ablation.

Thomas Philippe for writing the Python code of STALQUANT. All of the **beta-tester** are thanked for comments and wishes that improved capabilities and handling of STALQUANT.

Paolo Garofalo for introducing me to the Naica project.

Sebastian Breitenbach for the stalagmite samples and time in the lab.

Beni Aeschlimann, **Steffen Allner**, **Nicole Bachmann**, **Karin Birbaum**, **Robert Brogioli**, **Brokkoli**, **Olga Borovinskaya**, **Ladina Dorta**, **Tatiana Egorova**, **Nataliya Fedotova**, **Luca Flamigni**, **Dominik Fleitmann** and everyone from the STALCLIM sinergia project, **Daniel Fliegel**, **Gisela Fontaine**, **Christian Frei**, **Daniel Frick**, **Dominik Fricker**, **Silvia Fröhli**, **Reto Glaus**, **Sabrina Gschwind**, **Kathrin Hametner**, **Bodo Hattendorf**, **Dustin Hofstetter**, **Reinhard Kissner**, **Joachim Koch**, **Robert Kovacs**, **Daniel Kutscher**, **Lech Kwiecien**, **Ola Kwiecien**, **Giovanni Lotito**, **Big Mama**, **Eli Männel**, **Julien Mercadier**, **Caroline Münsterer**, **Masaki Ohata**, **Jorge Pisonero**, **Tabasco**, **Daniel Tabersky**, **Martin Tanner**, **Mohamed Tarik**, **Rebeca Valledor**, **Markus Wälle**, **Hao Wang**, **Helmar Wiltsche, Armin Zürcher**

Thanks to my family and friends, I have very much enjoyed working on my thesis!

Herzlichen Dank an meine Familie und Freunde. Danke für Eure Unterstützung!

Danke, Alexandra...

Contents

Abstract

Within the last 27 years laser ablation-inductively coupled plasma-mass spectrometry (LA-ICP-MS) has become one of the most widely used analytical techniques for high spatial resolution and quantitative major, minor and trace element analyses and isotope ratio determinations. A wide variety of lasers and ICP-MS instruments provide quantification capabilities with limits of detection in the ng/g range and crater diameters of less than 10 µm.

The analysis of larger objects, such as sediment cores, stalagmites, pearls and other climate archives has been limited by the transport systems used for laser-generated aerosols, depending mainly on the size of the ablation cell.

Therefore, the washout characteristics of a commercially available ablation cell were studied on fluid inclusions analyses, which generate signals of few seconds duration. The direct combination of gas inlet and gas outlet is suitable for small objects and leads to aerosol mixing. However, the gas flow dynamics calculated for this type of application showed that the aerosol transport is a function of the position of the sample within the cell.

The use of computational fluid dynamics (CFD) on different cell geometries provided insights into the gas flow pattern within ablation cells, which were optimized in detail within this work. It was shown that an indirect and homogeneous gas flow above the sample surface is crucial for reduced mixing of the laser-generated aerosol. Increasing the volume accompanied with minimal changes in the geometry of the effective volume improved the homogeneity of the gas flow at the ablation site. This leads to an aerosol washout time in the order of few seconds and allows detection of concentration changes within a spatial resolution of few µm. Furthermore, the size of the sample holder is uncritical as long as the effective volume for the aerosol expansion remains free of turbulences. A fast flushing of the sample holder was achieved by applying two gas inlets, one on each side of the cell. The experimental test of the transport efficiency showed minimal effects when changing the position of the ablation within the cell.

The newly developed cell allows hosting samples as long as 230 mm and 34 mm wide and is therefore well suited to hold sediment and stalagmite cores. The overall sensitivity was similar when compared to standard ablation cells with a smaller volume.

Based on the capabilities of analyzing 230 mm continuously, large data files were acquired. Since the data evaluation and reduction was very time-consuming, a new software program *STALQUANT* was developed. The program allows rapid signal selection and automated integration and calculation of concentrations and combines time domains with the actual sample position. Furthermore, the calculation scheme allows the

estimation of sensitivity, concentration, relative standard deviation and provides limits of detection based on the 3σ criterion and Poisson counting statistics. Furthermore, different external and internal standards can be used for quantification.

The experimental test of the ablation cell and the software were carried out on an electrophoresis gel, a sediment core from lake Zurich, a stalagmite from NE India and a pearl from the republic of Fiji.

The analyses on the lake sediment showed that the data acquired using the developed setup leads to good agreement for major and minor elements between qualitative µ-XRF and quantitative LA-ICP-MS. However, the application of LA-ICP-MS is, for similar spatial resolution, three orders of magnitude more sensitive thus providing access to trace element concentrations. The limits of detection were in the order of ng/g. Furthermore it was shown that external calibration combined with the 100 wt-% normalization procedure allows the quantification of laminated and heterogeneous samples.

Carbonates, such as the stalagmite and the pearl were quantified using a multi-element NIST glass as external calibration material and using Ca as internal standard. Normalization to 100 wt % corrected for concentration changes of the Ca in the laminated sample. The advantage of the fast washout of the cell was demonstrated by the generation of spatially resolved element images on a pearl and the annual element distribution pattern on the stalagmites.

Zusammenfassung

Während der letzten 27 Jahre wurde Induktiv Gekoppelte Plasma Massenspektrometrie mit Laserabtrag als Probenzufuhr (LA-ICP-MS) zu einer der am häufigsten angewendeten analytischen Methoden zur quantitativen Bestimmung von Haupt-, Neben- und Spurenelementen in Festkörperproben mit hoher räumlichen Auflösung. Eine grosse Vielfalt von verschiedenen Lasern und Massenspektrometern ermöglichen Nachweisgrenzen im ng/g Bereich für Ablationskraterdurchmesser von ca. 10 µm.

Die Analyse von grösseren Objekten, wie Sedimentkerne, Stalagmiten, Perlen und anderen Klimaarchiven war bisher limitiert durch die Grösse der Ablationszelle/Probenkammer, welche erforderlich ist, um die laser-generierten Aerosole in das Massenspektrometer zu überführen.

Um die Vor- und Nachteile der kommerziell erhältlichen Systeme zu untersuchen, wurden grundlegende Experimente zum Auswaschverhalten von Ablationszellen durchgeführt. Dazu wurden Flüssigeinschlüsse analysiert, die aufgrund der geringen Volumina zu Signallängen von von wenigen Sekunden führen. Anhand dieser Ergebnisse konnte gezeigt werden, dass die bestehenden Transportsysteme noch immer zur Vermischung von Aerosolpartikeln führen, weshalb die Gasströmungsprofile für Kammern mit direktem Gasein- und auslass mittels Computermodellen berechnet wurden.

Die durch Computer Modelle (computational fluid dynamics, CFD) erhaltenen Gasströmungsprofile wurden dann auf unterschiedliche Probenkammergeometrien angewendet, wodurch ein besseres Verständnis für das Gasströmungsverhalten generiert werden konnte. Mit diesen Untersuchungen konnte gezeigt werden, dass gleichförmige und indirekt über die Probenoberfläche verlaufende Gasströme nötig sind, um die Vermischung der Aerosolpartikel zu minimieren. Durch kleine Veränderungen und eine leichte Vergrösserung der Kammergeometrie bei der Laserabtragsposition wurden die Gasstromeigenschaften so verbessert, dass eine Verkürzung der Aerosolauswaschdauer auf wenige Sekunden erreicht wurde. Dies erlaubt die Detektion von Konzentrationsveränderungen in der Probe innerhalb weniger µm, da dadurch die Aerosolvermischung minimiert werden konnte. Darüber hinaus wurde gezeigt, dass das Gesamtvolumen der Probenkammer keinen Einfluss auf die Aerosolauswaschdauer hat, solange die Gasströme am Ort des Laserabtrags frei von Turbulenzen sind. Schnelles Ausspülen der atmosphärischen Gase nach dem Verschliessen der Kammer wurde durch die Einführung eines zweiten Gaseinlasses in den Probenraum erreicht. Experimentelle Untersuchungen über die Aerosoltransporteffizienz vom Ort der Ablation zeigten nur geringe Einflüsse auf die Signalintensität, weshalb der efektive Analysenbereich über die Gesamtgrösse des Verdampfungsraums erweitert werden konnte.

Die aufgrund der Modellierung und experimentellen Tests entwickelte Probenkammer erlaubt die Analyse von Objekten, die kleiner als 230 x 34 mm sind und ist besonders für die Analyse von Sediment- und Stalagmitenkernen geeignet. Die Empfindlichkeit (Aerosoltransporteffizienz) der in dieser Arbeit entwickelten Kammer ist vergleichbar mit den Standardkammern mit kleinerem Gesamtvolumen, erlaubt jedoch die Analyse von 5 mal längeren Objekten, was zu einer signifikanten Reduktion der Probenvorbereitung führt.

Die Möglichkeit zur kontinuierlichen Analyse von 230 mm langen Proben führt zu einer extremen Menge an Rohdaten, deren Verarbeitung und Umrechnung in Konzentrationen sehr zeitintensiv ist. Deshalb wurde ein automatisches Auswerterogramm *STALQUANT* enwickelt. Mit diesem Programm werden die Signale ausgewählt und danach mittels komplexen Algorithmen in Konzentrationen umgerechnet. Desweiteren werden Empfindlichkeiten, Konzentrationen, relative Standardabweichungen und Nachweisgrenzen basierend auf dem 3σ Kriterium oder der Zählstatistik nach Poisson berechnet. Darüber hinaus können unterschiedliche externe und interne Kalibrationsstandards verwendet werden und eine direkte Zuordnung der Daten zum Ort der Analyse wird ermöglicht.

Um die neuen Möglichkeiten der entwickelten Probenkammer im Zusammenhang mit dem entwickelten Auswertungsprogramm an praktischen Beispielen zu beweisen, wurde eine Vielzahl von unterschiedlichen Proben analysiert. Neben den Standardproben wurden Elektrophoresegele auf Hg, ein Sedimentkern aus dem Zürichsee, Stalagmiten aus Nord-Ost Indien und eine Zuchtperle von der Republik Fidschi auf die Haupt-, Neben- und Spurenelemente untersucht. Alle diese Proben verlangen hochauflösenden Laserabtrag und schnellen Aerosoltransport, um die zeitliche oder räumliche Änderung der Konzentration zu detektieren, die wiederum ein entscheidendes Kriterium für die Interpretation der Daten sind.

Die Analysenresultate des Seesediments zeigten eine gute Übereinstimmung für Haupt- und Spurenelemente zwischen qualitativen Röntgenfluoreszenzanalysen (µ-XRF) und der quantitativen LA-ICP-MS Analysen mit dem in dieser Arbeit entwickelten Transportsystem. Zusätzlich konnte nachgewiesen werden, dass mit LA-ICP-MS bei ähnlicher räumlicher Auflösung drei Grössenordnungen höhere Empfindlichkeiten erreichbar sind, wodurch Analysen von Spurenelementen bis in den ng/g Bereich möglich werden. Desweiteren konnte validiert werden, dass für heterogene Systeme eine Normalisierung der Resultate auf 100 wt-% zu quantitativen Daten führt, wenn alle Hauptbestandteile gemessen werden können oder diese als stöchiometrische Oxide in der Probe vorliegen.

Die Stalagmiten und Perlen konnten mittels eines Multielement NIST Glasstandards mit interner Standardisierung quantifiziert werden. Aufgrund der geringen Wachstumsraten der Objekte konnte hier besonders der Vorteil der kurzen Aerosolauswaschzeit demonstriert werden, was aus den hochaufgelösten Elementverteilungsbildern

eines Perlenquerschnitts und der jährlichen Elementkonzentrationsänderungen im Stalagmitenwachstum ersichtlich ist.

1 Introduction

Laser Ablation-Inductively Coupled Plasma-Mass Spectrometry (LA-ICP-MS) is currently the technique of choice for elemental analysis of solid samples. Since the introduction of LA-ICP-MS in 1985 by Gray [1], the fundamental principle of the technique has not changed. However, the performance of LA-ICP-MS heavily depends upon the characteristics of the ablation cell. This is an airtight device preventing atmospheric gases from entering and disturbing the plasma, where samples and standard reference materials are hosted. The ablation cell incorporates a window made of a material that is transparent at the wavelength of the laser light, through which the beam is focused onto the sample's surface (tens to hundreds µm). Each pulse of the high-energy beam ejects particles of the sample stoichiometrically and the laser generated aerosol is transported to the ICP by a carrier gas flow (commonly He). During the short residence time (µs) in the plasma at over 6000 K, the solid aerosol is vaporized, atomized and ionized. From there the ion beam is extracted by the ICP interface, reducing the pressure from ambient conditions down to high vacuum in two steps, by passing through the sampler cone and the skimmer cone. In the high vacuum chamber the ion beam is shaped by ion optics and photons as well as negatively charged and neutrals are separated by a photon stop. The positive ions pass through the mass filter (ana-

lyzer) and finally ions with a specific mass to charge ratio are counted by the detector. The purpose of LA is generating a discontinuous or continuous flow of aerosol that is ionized in the plasma, separated by the analyzer and recorded by the detector. For bulk analysis of homogeneous samples the recorded transient signal is integrated for quantification. Whereas for performing line scans along a heterogeneous sample like a stalagmite (profiling), the transient signal shows variations corresponding to the concentration changes in the sample. The line scans can be performed parallel across an area of the sample yielding the distribution of elements, i.e. elemental imaging. Recording of such variations in transient signals requires ablation cells with fast washout of the laser generated aerosol in order to avoid mixing of aerosol from different positions of the line scan assuring high spatial resolution. Most of the commercially available ablation cells are relatively small, requiring cutting large samples into smaller segments fitting into the ablation cell. For many samples cutting and destruction is not optional, hence a large ablation cell, able to host the entire sample, is required.

First quantitative analysis of trace rare earth elements in a variety of minerals has been reported by Jackson et al [2]. Soon limited access to accurate quantitative data of volatile elements has been discovered and attributed to elemental fractionation which comes from non-stoichiometric sampling, transport and/or incomplete vaporization in the plasma [3]. The introduction of lasers (ArF excimer) with 193 nm wavelength reduced elemental fractionation due to more controlled ablation. This has been demonstrated on quartz samples when drilling out fluid inclusions in mineral thin sections [4]. Furthermore, the utilization of He as carrier gas, first reported by Eggins et al. [5], lead to the generation of smaller particles and thus to more complete vaporization in the plasma. More accessible laser systems in the UV range (213 nm and 266 nm) became available and the fundamental differences in particle size distribution of the three UV laser wavelengths have been reported by Guillong et al. [6], indicating the advantages of the low VUV wavelength in terms of particle size distribution. This has lead to studies investigating ICP-induced fractionation on aerosol generated using various laser wavelengths [7], attributed to incomplete vaporization of large particles in the plasma. Guillong et al. [6] demonstrated that certain particle sizes (in the order of a few hundred nm) are not completely vaporized within the ICP. This effect was visualized by Aeschlimann et al. [8], observing intense streaks of large particles in photographs of the plasma.

Further development in instrumentation has lead to the use of femtosecond (fs) lasers [9]. Studies utilizing fs lasers for LA of metallic samples have been published for laser-induced breakdown spectroscopy [10]. The advantages of such lasers operated at 196 nm has been demonstrated on Fe isotope ratio determinations and indicated that these types of lasers generate stoichiometric aerosol which can be vaporized and ionized within the ICP [11]. The differences between ns and fs lasers, the expansion of the plume [12–14], transport of the aerosol [15,16], visualization of the aerosol within the ablation cell [13] and within the transport tubes [17] have been reported.

Research and development of LA-ICP-MS during the last decade was dominated by a large number of applications, which is mainly based on the fact that this technique allows analyses under normal atmosphere, which makes LA-ICP-MS easier applicable than secondary ion mass spectrometry (SIMS), laser microprobe mass analysis (LAMMA), and electron probe micro analysis (EPMA), all of them requiring low pressure conditions. The possibility to obtain quantitative results of main and trace element composition of any kind of solid sample together with the ability to determine isotope ratios with high accuracy and high precision are some of the key features for the success of LA-ICP-MS. Thus, the technique is widely used in earth sciences, gemology, material sciences and industrial quality control applications [18]. Apart from bulk- and microanalysis, and depth profiling [19], more advanced applications such as fingerprinting of archeological objects [20], isotope ratio determinations [21] and elemental imaging (line scans [22–27], profiling [28] and mapping [29–31]) became popular applications and lead to new insights into various fields of research.

The most common sample introduction systems into the ICP as an ion source are schematically represented in Figure 1. The two basic sample introduction systems are generating liquid aerosol (solution nebulization) or solid state aerosols (laser ablation (Figure 1A,B)) which can be introduced and ionized in the ICP. From the wide range of different mass analyzers used in combination with ICP, the six most abundant analyzers are shown, and are explained in more detail in the following chapter. The set-up used in this thesis is represented in Figure 1B/C/E, i.e. LA-ICP-Q-MS.

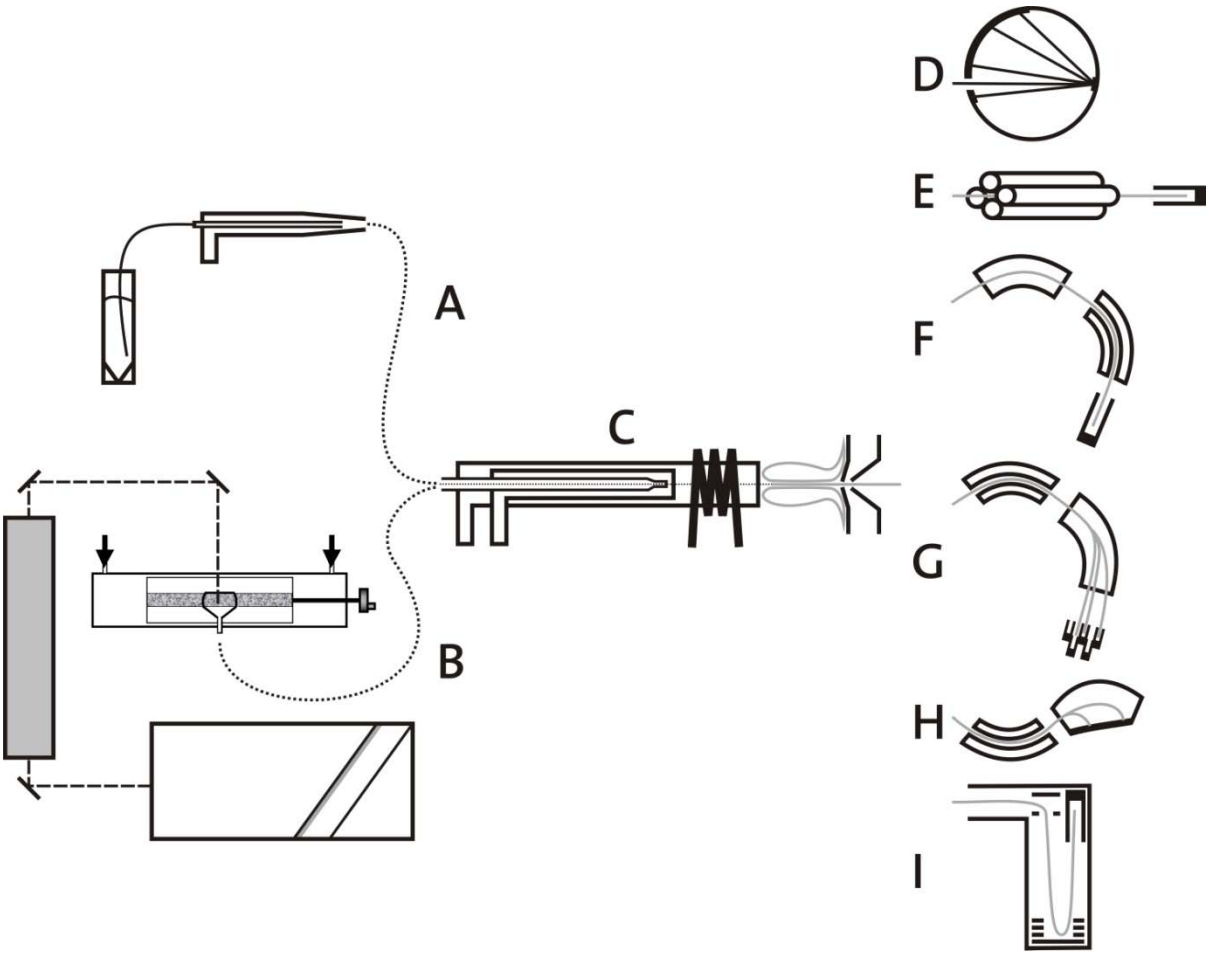

Figure 1: Schematic representation of the most common instrumentation around the ICP ion source: torch, load coil, plasma and interface (C). Aerosol generated from solution nebulization (A) or laser ablation (B) are transported (dotted line) into the ion source (C). The ions (grey solid line) can be filtered by several types of analyzers (E-I) before counted by the detector. The quadrupole (E) and the sector field (F) are sequential MS, while G (multi collector, Nier-Johnson geometry) and H (Mattauch-Herzog geometry) are simultaneous MS. The time-of-flight (I) is a pulsed MS. ICP optical emission spectrometry is represented by D. The laser beam (dashed line) in the configuration used in this work passes through the beam homogenizer (grey box) before being imaged through the ablation cell window onto the samples surface inside of the cell.

1.1 Instrumentation

1.1.1 Laser ablation

After years of solution-based ICP elemental analysis, the availability of ruby lasers has lead to experiments of introducing solid aerosols instead of liquid droplets into the ICP ion source. The development of early laser ablation was initially carried out for coupling to ICP-Optical Emission Spectroscopy (ICP-OES) [32–34], soon followed by LA-ICP-

MS [1,35,36]. The laser is used as a micro sampling device, where the laser beam is focused onto the sample surface (sub-tens to hundreds of µm of spot size diameter). The high energy pulse ablates a small amount of sample, which is transported by a carrier gas as solid aerosol through transport tubes to the ICP. In contrast to Laser Microprobe Mass Analyzer (LAMMA), which is using the laser ablation plasma as the ion source, LA depends on aerosol transport and the ICP as the ion source.

The types of available lasers can be categorized by source and wavelength of the emitted light, and pulse duration. The most common pulsed laser types used for LA-ICP-MS are solid state lasers (Nd:YAG) and gas lasers (ArF excimer) at ns pulsewidth and solid state lasers (Nd:YAG or Ti:sapphire) to generate ns and fs pulses, respectively. An overview of the available wavelength and pulse durations is given in Table 1.

Table 1: Wavelength of the first harmonic (bold type) of various lasers, frequency doubled and 3., 4. and 5. harmonic.

	IR	VIS	UV
Ti:sapphire, ~150 fs	**670-1130 nm**		360-460 nm (2^{nd}), 235-330 nm (3^{rd})
Nd:YAG, <6 ns	**1064 nm**	532 nm (2^{nd})	355 nm (3^{rd}), 266 nm (4^{th}), 213 nm (5^{th})
ArF, 15-20 ns			**193 nm**

Most solid state lasers emit light in the near infrared (1064 nm) which can be frequency doubled (532 nm) or quadrupled (266 nm) using non-linear optics. However, each step in frequency change involves the loss of energy, thus using the 3^{rd}, 4^{th} or 5^{th} harmonic of a laser results in lower energy available for LA. Despite of the loss of energy, short wavelength lasers are nowadays most often used, as it has been shown that shorter wavelength LA generates aerosol with smaller particlesizes [7], which is favorable for ICP-MS due to complete vaporization of particles within the plasma. Several reports of superior qualities of UV LA compared to IR LA have been published [37–39]. The output energy of an ArF excimer laser is sufficiently high (240 mJ), which allowed the implementation of beam homogenizing optics, leading to flat top laser beam profiles and very controlled and homogeneous and flat ablation craters. Despite the loss of energy through all the optical components required, fluencies of more than 40 J/cm^2 can be reached. The use of a homogenized beam has lead to improved precision and accuracies in various analyses [4]. An advantage is the fact that the beam energy density is independent of the selected crater size, which is in contrast to Gaussian beam shapes having the highest energy density in the center of the beam. The ArF laser and homogenizer used in this thesis are depicted in Figure 2. Moreover, performing flat top ablation leads to significantly higher signal stability over a longer period of time, whereas a Gaussian profile crater quickly reach a critical depth from which no aerosol can be sampled anymore. This depends on the aspect ratio (depth/diameter) [40]. Therefore, homogenized beams have been studied using different wavelengths

(266 nm Nd:YAG and 193 nm ArF excimer) and are currently used in all commercially available systems [41].

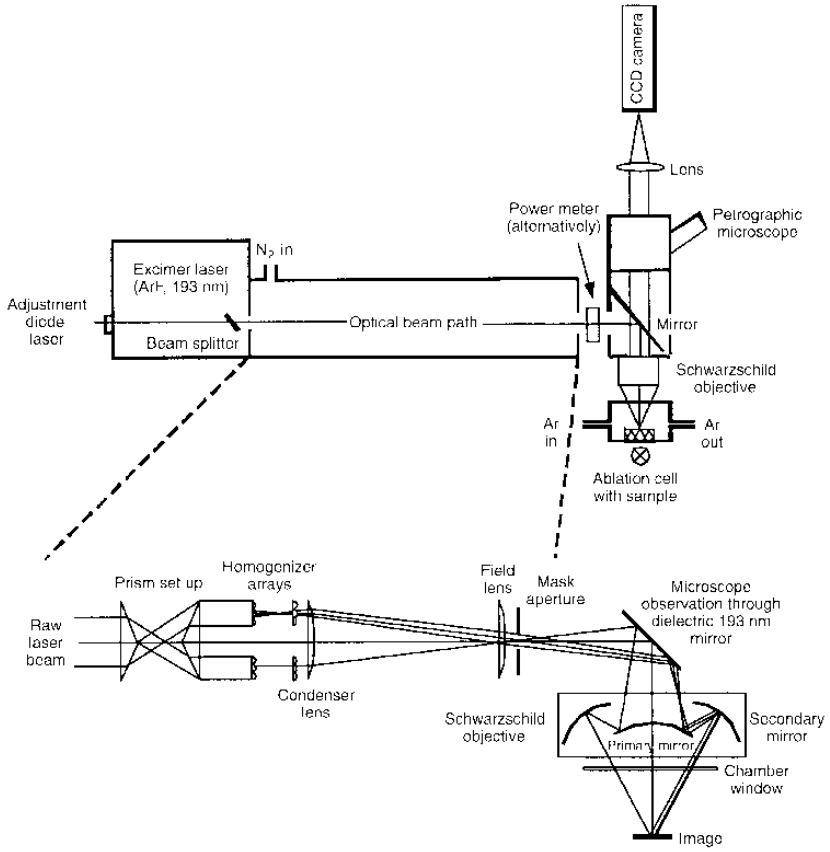

Figure 2: The ArF excimer laser and details of the beam homogenizer from [4].

Furthermore, influences on aerosol quality depending on the type of carrier gas have been reported [5,40,42]. Eggins et al. [5] proposed the use of He since He allows the transport of smaller aerosol particles and leads to reduced surface deposition around craters. Sensitivity enhancement has also been observed by the addition of small amounts of H_2 to the carrier gas, upstream of the ablation cell [43].

However, it has been reported that UV-ns laser ablation is not suitable for stoichiometric sampling of non-conducting and conducting samples. For example, Outridge [44], Chen [45], Figg et al. [46] reported temporal changes of element ratios. Fryer [3] introduced the term *elemental fractionation* (EF) for temporal changes in elemental ratios. Later, EF indices have been updated [47] with several other studies investigating fractionation effects using ns and fs LA [11,48–52] at different wavelengths [53]. It has been shown that EF was significantly reduced for non-conducting samples by the introduction of 193 nm lasers when compared to 266 nm. However, the "longer" pulse width of ns lasers leads to partial heating of conducting samples, which results in non-representative sampling. Therefore, femtosecond lasers, with pulse durations smaller

than 1 ps have been tested in LA-ICP-MS [12,54,55]. One of the major advantages of fs LA when compared to ns LA-ICP-MS has been found for the analysis of metallic samples [56,57]. The improvement has been attributed to the short pulsewidth in the order of femtoseconds being sufficiently short to reduce heat effects in the ablation zone [9,58], thereby decreasing elemental fractionation. On the other hand, for fs-LA of non-metals superiority has not been demonstrated as reported by Birbaum [59] and Glaus et al. [60].

The major advantage of elemental analysis of solids using LA is the direct solid sampling with little sample preparation, which is in contrast to solution ICP analysis for which the solid samples have to be digested and diluted prior to analysis. Digestion of solid samples is labour-intensive, involves the use of wet-chemistry, i.e. high purity acids, and every step may potentially lead to sample loss or introduce trace level contamination, altogether inferior to direct solid sampling using laser ablation [61]. Furthermore, LA is commonly considered quasi non-destructive [61,62] due to the small crater size used for sampling, which can be invisible to the naked eye. Single hole drilling mode as well as line scanning mode are commonly used. Additionally a few studies on single pulse analysis have been reported [63,64]. This lead to the successful application of LA for trace element fingerprinting of gemstones [62,65], where sampling, usually located on the girdle [20], is not degrading the value of the gemstone. Limits of detection (LODs) depend on crater size [4] and instrument sensitivity, which has improved over the years by short laser pulse length [58] and the use of He as carrier gas [5,42].

Using multi element standard reference materials (SRM) as external standard and an internal standard (correcting for different ablation rates) [2,18], which are determined by an independent analytical method or calculated from the stoichiometry of the sample, is the most applied quantification protocol introduced by Longerich et al. [66] (equations explained in detail in chapter 4.3). In the absence of a concentration for an internal standard [67], a normalization to 100wt% of all present main elements in a sample has been reported [68]. However, this procedure works only when all elements present in the sample can be and have been analyzed. Non-matrix matched calibration of $CaCO_3$ reference samples using NIST SRM has been reported [69–71], and the obtained results for trace elements agreed within 10 % with the recommended values. Several studies focused on other aspects of laser ablation, e.g. transport tube material [72] and rectangular craters [5]. The most recent fundamental study investigated the ablation behavior of carbon [73], since it is one of the most used internal standards for tissue analysis [74]. Frick and Günther found that part of the ablated sample is transported as a gas rather than solid depending on the presence or absence of oxygen in the matrix [73].

1.1.2 Ablation cells

The ablation cell is the most important part influencing the performance of LA-ICP-MS and several requirements are indispensable for a routine ablation cell. First of all, an ablation cell must be airtight preventing atmospheric gases from entering and extinguishing the ICP as well as preventing loss of carrier gas and aerosol. Second, the carrier gas flowing through the cell must transport the laser-generated aerosol as completely as possible (ideally 100%) to the ICP. Third, hosting and mounting of at least one sample and one external standard must be possible; generally a number of samples and standards are mounted simultaneously. Fourth, the laser beam must pass through the ablation window, i.e. a material which is transparent at the wavelength of the laser light and should not be too close to the ablation site to avoid aerosol deposition on the inner side of the window. Last, mounting and positioning the ablation cell at the LA system and observation of the sampling position must be assured. Most of the commercially available ablations cells meet these requirements. However, for more demanding applications than bulk analysis, such as elemental depth profiling [75,76] and/or imaging [31], the requirements particularly for aerosol washout are more stringent. The spatial resolution of transient signals generated from line scans is determined by the aerosol washout time. For bulk analysis of homogeneous samples the washout time is less critical, as the entire signal of the sample is integrated to calculate elemental concentrations. On the other hand, when performing line scans on heterogeneous samples, the transient signal should reflect the variation of element concentration within the sample. Therefore, a long washout (high dispersion) leads to mixing of aerosol originating from different laser pulses at different locations along the line scan, resulting in distorted signals. Therefore, spatial information is lost and can only be made available by using complex deconvolution algorithms. Furthermore, long washout and mixing of the aerosol may lead to cross contamination, which has a significant influence on the accuracy of the analysis.

The early ablation cells were developed for LA-GF-AAS [77] and LA-ICP-AES [32–34] but are in principle similar to those for LA-ICP-MS. An early study by Arrowsmith and Hughes [36] have reported a cell in the cell approach in order to entrain and transport the laser-generated aerosol. This approach was further developed by several groups [15,78] for the latter the authors suggested the use of an aerosol mixing device (squid), placed between the ablation cell and the ICP for smoothing the signal. Later the use of a two volume ablation cell has been reported, however it was coupled to a MS for stable isotope determination ($\delta^{13}C$ and $\delta^{18}O$) [79] and not to ICP-MS. Recently, a Volume-Optional Low Memory (VOLM) ablation cell, which is also using two cell volumes, has been published [80]. These approaches are based on sophisticated ablation cell mechanics, as the second volume cylinder moved together with the laser beam to the location where LA is performed.

Fundamental studies on the aerosol transport in the ablation cell and the transport tubing using powder deposition in the cells have been reported [81]. The observations match gas flow modelling (see following chapter 1.1.3). The authors have reported that by using very small ablation cells the transport efficiency is limited due to particle-wall interactions. Bleiner and Altorfer [82] introduced the use of a rotating nozzle minimizing the dead volume in large ablation cell, with the inlet gas sweeping the entire cell volume. A cyclonic flux cell, sweeping the carrier gas from the ablation cell walls to the center, has been presented [83]. Tangential or circular gas flows have also been reported by Pisonero et al. [84] using a so-called High Efficiency Aerosol Dispersion (HEAD) cell. This principle is based on two volumes as well, in combination with a Venturi-effect extraction. Based on the experimental work, Lindner et al. [85] described computer models suggesting improvements of the HEAD cell, which should result in very fast washout times. He proposed the entrainment of the aerosol in a directed secondary gas flow and thus reducing the particle-wall interaction in the transport tubes.

Many approaches of ablation cell design worked on the basic morphology of an enlarged transport tube resulting in a washout of less than 100 ms for relatively large samples [86]. Small ablation cells based on the same principle have been reported [25,87].

Ultimately, the fast aerosol washout of in-tube ablation can only be superseded by in-torch ablation introduced by Tanner and Günther [64,88,89], both of which constituting severe limitations in sample handling, thus averting applications in routine analysis.

After the world records of fast aerosol washout have been claimed, further efforts concentrated on ablation cell development for routine analysis and specialized applications. Analysis of large samples is only possible by cutting, in order to fit into the small ablation cells that have been developed. As the most common applications of LA-ICP-MS have been analyses of geological samples: rocks, thin sections and minerals. These samples are small enough to be hosted in the ablation cells. However, for many types of samples it is simply impractical or impossible to destroy them by taking a small section, e.g. precious objects, museum artifacts or immobile large objects. Therefore, ablation cell developments were focused on open configurations. An early approach using an open ablation cell and modelling plasticine seal to prevent carrier gas and aerosol from escaping through the aperture, has been reported by Günther and Gäckle [90] for LA-ICP-OES and by Devos et al. [91] for LA-ICP-MS. The same has been reported later by Wagner and Jedral [92], using an ablation cell without bottom and applying adhesive materials to attach the cell to an object and sealing it. Both of these designs are not truly open, as they form an airtight configuration using the sample itself as part of the cell. However, the only true open, non-contact ablation cell reported so far presented by Asogan et al. [93], uses several concentric gas curtains in order to fully exclude atmospheric gases. But even this set-up requires close proximity to the sample surface.

The future in LA-ICP-MS should allow analysis without an ablation cell. First directions have been demonstrated by using a Gas Exchange Device (GED) as reported by Kovacs et al. [94]. Such a device can exchange atmospheric gases (Air) by Ar or He without altering the laser generated aerosol, making airtight ablation cells obsolete. Although the use of a plume entrainment device, introduced by Tabersky et al. [95] significantly improves aerosol sampling. However, the approach is still accompanied with loss of intensity and further research is required.

The various applications of LA-ICP-MS request a wide variety of ablation cells. Therefore, the literature about ablation cells is extensive and a number of specialized ablation cell designs have been developed. An example is a closed cubic ablation cell with a rotating cylinder inside, onto which membranes with protein blots are attached [96]. The lanes are sequentially rotated into the effective volume for line scanning by LA. However, this promising approach is limited to bendable samples. A cooled ablation cell has been developed for the direct ablation of frozen ice core samples [97,98]. Another cooled ablation cell (a two volume cell [78] extended with Peltier elements) has been reported [99] for the same application. Finally, a cryogenic ablation cell has also been reported to be used for LA-ICP-MS of soft biological tissues [74]. The most recent publication of a new ablation cell allowed following different sampling protocols by a variable volume chamber [100].

Three companies currently offer various ablation cells with their LA systems. For example, RESONETICS [101] provides their laser ablation systems with the Laurin Technic ablation cell [78]. New Wave Research [102] currently offers four ablation cells: paper cell, super cell, cryo cell and a large format cell. CETAC [103] currently offers five ablation cells with similar names, standard cell, large format cell [104], document cell, cryo cell [74] and the sediment cell [105]. One of them, the so-called sediment cell is the cell developed during this thesis. The name 'sediment cell' is misleading, because it implies the specific use for only sediment analysis (e.g. ablation cell customized for sediment core analysis [104] only). However, many other applications became possible by using the ablation cell developed for this thesis (chapter 2.5).

1.1.3 Computational Fluid Dynamic Modeling

Computational fluid dynamic (CFD) modeling can be used to visualize physical properties of a fluid in or around a solid object. In this thesis the fluid was set to a gas (He) and the properties studied were gas velocity and direction using ANSYS CFX 11.0 [106]. The objects (the inner volumes of several ablation cells) were described numerically by a mesh representing the solid boundaries. Gas flows were defined as areas of inflow and outflow in the mesh. From a given gas pressure the modeling software iteratively

calculates the properties of each polygon volume (tetrahedral or prismatic) in the mesh. A stable solution is found when the number of changes in the mesh polygons from one to another iteration falls below a defined limit. An oscillating system will not be detected as stable and thus the iteration will not be stopped automatically. More accurate results are obtained by defining a finer mesh with a large number of polygons. However, computing time drastically increases with the number of polygons. Hence, a compromise between meshing polygon size and calculating time must be found. Detailed descriptions of numerical simulation for design analysis of LA cells have been given by Bleiner and Bogaerts [107] and Autrique et al. [108].

Many properties such as gas mixing, heat sources, particle transport, etc. can be defined to obtain a model as close to reality as possible. However, several approximations are commonly made in order to end up with reasonable computing time while still describing the system accurately. Nonetheless, it is important to be aware of the models results and its relevance to reality. Minor errors in the object mesh or approximations may produce gas flow features that can be incorrectly interpreted as a feature whereas it can also be the result of an artifact.

The standard cylindrical ablation cell [109] used in this study has already been modeled and reported in several publications [9,17,110], in which it was shown that gas flows propagate in a central channel over the sample surface and are not completely transported through the outlet. The forming vortices are trapping the laser-generated aerosol leading to long washout times. Another ablation cell, the HEAD cell published by Pisonero et al. [84], was modeled by Lindner et al. [85] reporting particle tracking and aerosol washout calculated based on these models. However, the modeled washout time has not been experimentally reached so far.

Computational studies also have been reported for other processes of LA-ICP-MS. For example, the aerosol transport in the tubing and the influence of gas type and gas velocity were reported by Bleiner and Bogaerts [111]. Others have studied the sampling interface, modeled the fundamental characteristics of an ICP to investigate gas flow velocities, plasma temperature and electron density [112]. Triglav et al. [113] have reported ICP-MS signal models for elemental imaging and found that the signal distortion of the image is mostly based on the aerosol washout of the ablation cell. Taking this concept one step further, they proposed to acquire the signals with fast line scans and corrected the output via deconvolution to remove the signal distortion, an approach that decreases measurement time but increases mathematical alteration of the acquired data. Theoretical discussions on acquisition time reduction while maintaining integrity of the image produced have also been reported [114].

1.1.4 Inductively Coupled Plasma Mass Spectrometry

Soon after the ICP-MS has been introduced, reports of elemental analysis have been published and solution nebulization remained the strongest field of application [115]. The first coupling to laser ablation [1], and later overviews [2,18,61,116] are indications for the versatility of this ionization source. ICP-MS has several advantages in comparison to the longer established ICP-OES, such as lower limits of detections, nine orders of magnitude linear dynamic range, access to isotope information, and most elements of the periodic table can be determined. Due to the sensitivity of this technique, analyte concentrations can be diluted in solution ICP-MS [117], which reduced matrix effects and contributed to the wide range of applications this technique has reached so far.

The argon plasma as the ion source vaporizes, atomizes and ionizes the aerosol, regardless whether it is liquid or solid. The ion beam is extracted by the interface passing through the sampler cone and the skimmer cone in two steps from atmospheric pressure into high vacuum. The photon stop removes negatively charged ions, neutrals and photons from the ion beam that is shaped by the ion optics before entering the mass filter. The mass filter (or analyzer) separates the ions by their mass to charge ratios that are then counted by the single detector.

The three most common types of mass analyzers in inorganic mass spectrometry are the quadrupole, the magnetic sector and the time of flight mass spectrometer, shown in Figure 1. The quadrupole is a low resolution, fast sequential mass filter consisting of four parallel rods, connected pair-wise to radio frequency (RF) voltage and direct current (DV) voltage. Depending on the applied voltages, ions of only one mass to charge ratio can pass the filter and are counted in the detector. All other ions have unstable trajectories and are ejected. ICP-MS suffers from interferences, as the mass filters separate the ions based on their mass to charge ratios, usually referring to a singly charged isotope of an element. Several isobaric interferences occur due to other ions or clusters with a similar mass per charge ratio [109,118]. The most important interferences are listed in Table 2, which occur at low mass resolution (m/Δm 300, quadrupole ICP-MS).

Table 2: List of common interferences possible in ICP-MS analysis and suggested alternatives. The formation of interferences needs to be evaluated for each analysis, as interferences depend on the matrix. Analyte (An) can be any element to be detected.

Interference form	Interference example	Isotope of interest	Alternative
An^{++}	$^{138}Ba^{+}$	$^{69}Ga^{+}$	$^{71}Ga^{+}$
$AnAr^{+}$	$^{23}Na^{40}Ar^{+}$	$^{63}Cu^{+}$	$^{65}Cu^{+}$
AnO^{+}	$^{40}Ar^{16}O^{+}$	$^{56}Fe^{+}$	$^{57}Fe^{+}$
O_2^{+}	$^{16}O_2^{+}$	$^{32}S^{+}$	$^{34}S^{+}$
An^{+}	$^{50}Cr^{+}$	$^{50}Ti^{+}$	$^{48}Ti^{+}$
$AnCl^{+}$	$^{40}Ar^{35}Cl^{+}$	$^{75}As^{+}$	HR-ICP-MS
Ar^{+}, high abundance in plasma	$^{40}Ar^{+}$, $^{80}Ar^{+}$	$^{40}Ca^{+}$, $^{80}Se^{+}$	$^{42}Ca^{+}$, $^{78}Se^{+}$

In case alternative isotopes are not available, high resolution (HR) ICP-MS can be used in order to resolve most of the interferences in ICP-MS. The most widely used HR-ICP-MS are based on various combinations of a magnetic field (mass analyzer), electrostatic analyzer (ESA, kinetic energy analyzer) with single, multiple or array detectors as shown in Figure 1. The sector field ICP-MS with single detector is using a magnetic field prior to the ESA, which is known as reverse Nier-Johnson geometry. The introduction of a sector field ICP-MS with many detectors or multi collector (MC) ICP-MS (Nier-Johnson geometry) has also been introduced and opened applications on precise isotope ratio measurements, as this instrument is not sequential, but the detectors record true simultaneous isotope ratios with high precision and applications in dating [119]. Most recent developments have been made towards simultaneous detection of all elements (from m/Z 7-250), by using the Mattauch-Herzog geometry [120] of sector field ICP-MS with an array detector [121–124]. The coupling of TOF-MS to the ICP ion source is not straight forward due to the continuous ion beam delivered by the ICP and the pulsed nature of the TOF analyzer. However, some reports using ICP-TOF-MS have been published [74,89,100,125–128].

1.2 Aim of the thesis

Laser ablation-inductively coupled plasma-mass spectrometry (LA-ICP-MS) is currently one of the most widely used analytical techniques for major, minor and trace element analysis and isotope ratio determinations. A wide variety of samples have been studied and applications have been demonstrated successfully [18,116]. However, beside a lot of technological progress in laser and ICP-MS instrumentation, the transport system for laser-generated aerosols remains one of the major challenges, especially for samples of different sizes and shapes. A wide variety of ablation cells are available and all of the geometries reported are suited to generate stable signals. However, for most of the transport systems the samples need to be cut into pieces smaller than 3x5 cm.

To describe the capabilities of existing ablation cells for analyzing short transient signals, studies on fluid inclusions using a commercially available ablation cell were carried out. Therefore, unique samples (giant crystals from Naica, Mexico) were used for analysis to contribute to the general understanding of the crystal growth.

Based on the evaluation of the commercial ablation cell on short transient signals, the major part of the work carried out within this PhD thesis was focused on the development of an ablation cell for large samples, in particular for samples where cutting or removing a small section would lead to a significant loss of the object'svalue or analytical information. The criteria for the cell development were defined by maximum size of objects while maintaining fast washout and transport of laser-generated aerosols into the ICP-MS. The development of the cell included a mathematical and theoretical description of the gas flow dynamics within a given cell geometry using Computational Fluid Dynamics (CFD). Furthermore, the most suitable geometry was realized, optimized and experimentally tested.

Analyses by LA-ICP-MS provide large data sets and only a minor part of the generated information is readily available. This is mainly due to the time-consuming data reduction and calculation. Therefore, a mathematical routine for data reduction and quantification and the implementation into a software package was aimed within this thesis. The software was planned and designed to provide fast access to quantitative elemental information at a high degree of flexibility and to be independent of type of instrumentation. Furthermore and most critical for the type of applications, the software aimed to combine transient signals with the exact position of analysis on the sample, which is an important prerequisite for imaging and mapping.

Finally, the suitability of the cell for high resolution imaging and mapping in quantitative analysis was tested on large samples, such as stalagmite cross sections, sediment cores and pearls. These applications were aimed to demonstrate enhanced capabilities of LA-ICP-MS and to provide some new insights into climate archives.

2 Modelling of gas flows within the ablation cell

The work presented in this chapter resulted from collaboration with Dr. Rolf Dietiker, (Laboratory of Inorganic Chemistry, D-CHAB, ETH Zurich) supporting the CFD modelling and Roland Mäder (Machine Shop D-CHAB, ETH Zurich) providing the CAD drawings and manufacturing the ablation cell.

2.1 Introduction

Computational fluid dynamic (CFD) modelling is currently used to study gas flow properties within the ablation cell [17,85,107,110]. The knowledge gained with these simulations can be used for the development of specialized ablation cells with novel properties. Therefore, modelling of the standard ablation cell [109] was conducted to investigate the gas flow behaviour. Based on this work, modelling of various geometries allowed selecting the most promising and build it as a prototype. Eventually, during the experimental characterisation of the prototype numerous improvements were implemented. The goal was to develop an ablation cell that can host large samples allowing the laser to access any position on the surface for fast profiling and mapping applications. A number of small volume ablation cells have been reported in the literature [82,86]. However, some samples cannot be cut or damaged to fit into the cell. Therefore, limited reports of analyses of historic artifacts, precious objects or stalagmites can be found in the literature [91,129]. Hence, a large ablation meets these requirements allowing LA-based analysis for numerous samples.

2.2 Standard cylindrical ablation cell

The standard cylindrical ablation cell [109] used with most LA systems in our laboratories offers a volume of 63 cm^3 to hold samples which can be as large as 50 mm in diameter. It is equipped with a PTFE seal that automatically closes the carrier gas outlet (to the ICP) when the cell is opened for sample replacement, preventing air from being transported to the ICP. However, such a cell exhibits high aerosol dispersion leading to aerosol washout times in the order of tens of seconds. By that, bulk analysis of homogeneous samples is not compromised, but spatial resolution is reduced when performing line scans on heterogeneous sample surfaces. The gas flow dynamics within the ablation cell were modeled using ANSYS CFX 11.0 [106]. The fluid was set to Helium at standard temperature and pressure (STP), inflow and outflow were set to a mass flow of 2.0767×10^{-3} g/s at 25°C, (standard settings 1 L/min). CFD modeling [9,17,110] revealed that a central channel region with high velocity gas is present. However, the gas flow in most parts of the cell is close to zero and does not contribute to the aerosol transport (Figure 3). Furthermore, the design leads to the formation of vortices while the carrier gas flows through the cell leading to an equilibrium state, where many gas flow vectors are pointing away from the outlet. In such a configuration laser generated aerosol is delayed within the vortices and mixes with aerosol from subsequent laser pulses. This effect reduces spatial resolution when scanning over a sample with heterogeneous composition. Additionally, it can also cause cross-contamination as settling aerosol is deposited on other sample positions or samples that are mounted at the same time within the cell. The modeling further showed that such effects are enhanced when using a nozzle gas inlet leading to higher gas velocity and even more pronounce formation of vortices, as shown in Figure 4. For example, the gas flow velocity on the surface of sample 2 is the lowest within the entire cell and aerosol transport takes hundreds of seconds. Since this configuration represents a typical placement of the samples within an ablation cell, it can be seen that such geometries are not suited for high spatial resolution profiling and mapping applications.

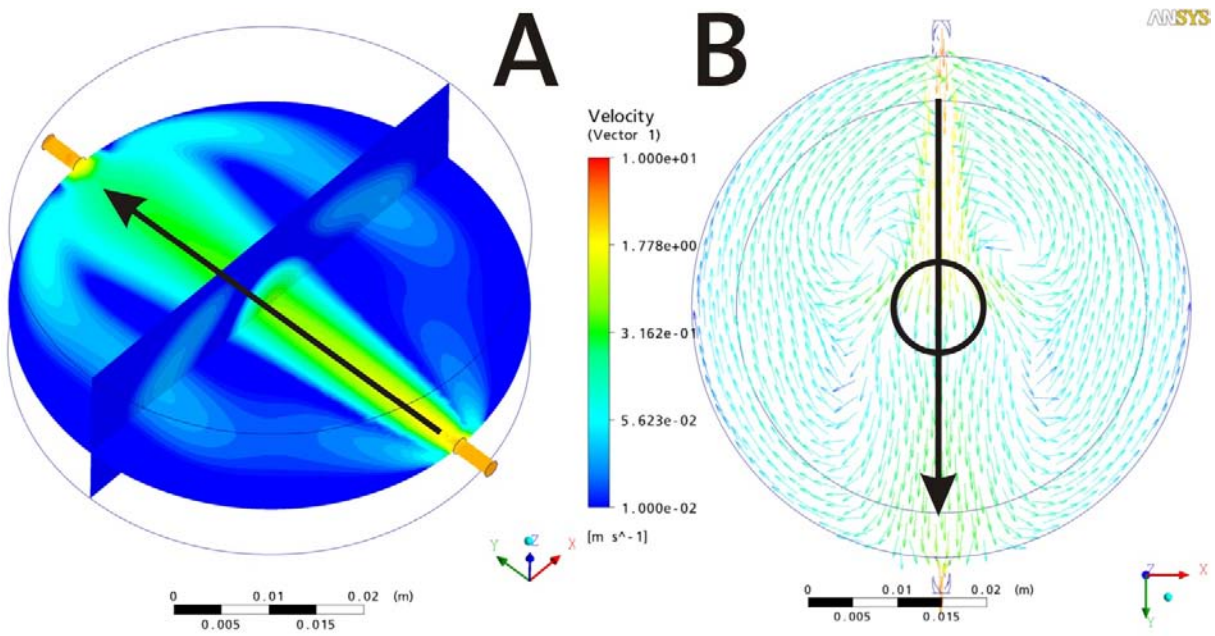

Figure 3: Modeled gas flow velocity and directional vectors of the standard cylindrical ablation cell. Some areas with slow gas velocities (A, dark blue) are present within the cell, modeled without sample. The gas flow vectors (B, with sample placed in center) is facing upstream for more than half of the available are, indeed the laser generated aerosol is carried in the circles of the gas flow until it is finally passing though the cell outlet as indicated by the relatively long washout (10-20 s) of such an ablation cell.

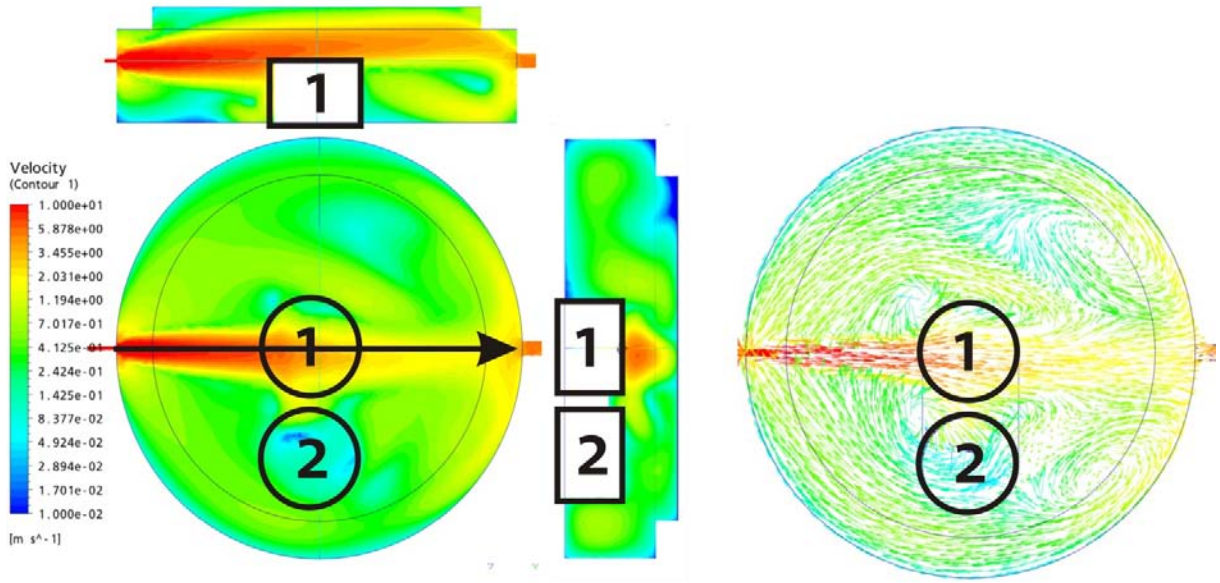

Figure 4: Modeled gas flow velocity and directional vectors for the standard cylindrical ablation cell with a nozzle gas inlet, leading to higher gas flow velocity, with two typical samples (1 and 2) mounted.

2.3 Shielded standard cylindrical ablation cell

Based on the preliminary gas flow studies, it becomes obvious that the washout of the standard cylindrical cell can only be improved by changing the geometry of the gas in- and outlet. As shown above, gas flows within the ablation cell must not rebound from the ablation cell wall, but should point to the carrier gas outlet as soon as the aerosol is gas-borne. The idea of converting the gas jet from the inlet nozzle to a gas sheet flowing over the samples and pushing the aerosol to the outlet was translated into a model and tested. A piece of thin aluminum was mounted into the cell in order to separate the direct gas jet from the samples (Figure 5) which leads to the generation of a gas sheet. The models show that for more than half of the available area in the cell all gas flow vectors are pointing towards the outlet. Thus, any sample can be placed there with all laser generated aerosol being transported directly to the outlet within a short path. This is the case regardless of the sample placement, as shown in Figure 5. The gas flow distribution within such an ablation cell improves the washout times (from 25 s to 19 s) but still leaves room for improvement as observed in the experiment. Nevertheless, the understanding of the dependence of gas flows on the ablation cell geometry was vital for the development of a much larger ablation cell capable of hosting large samples.

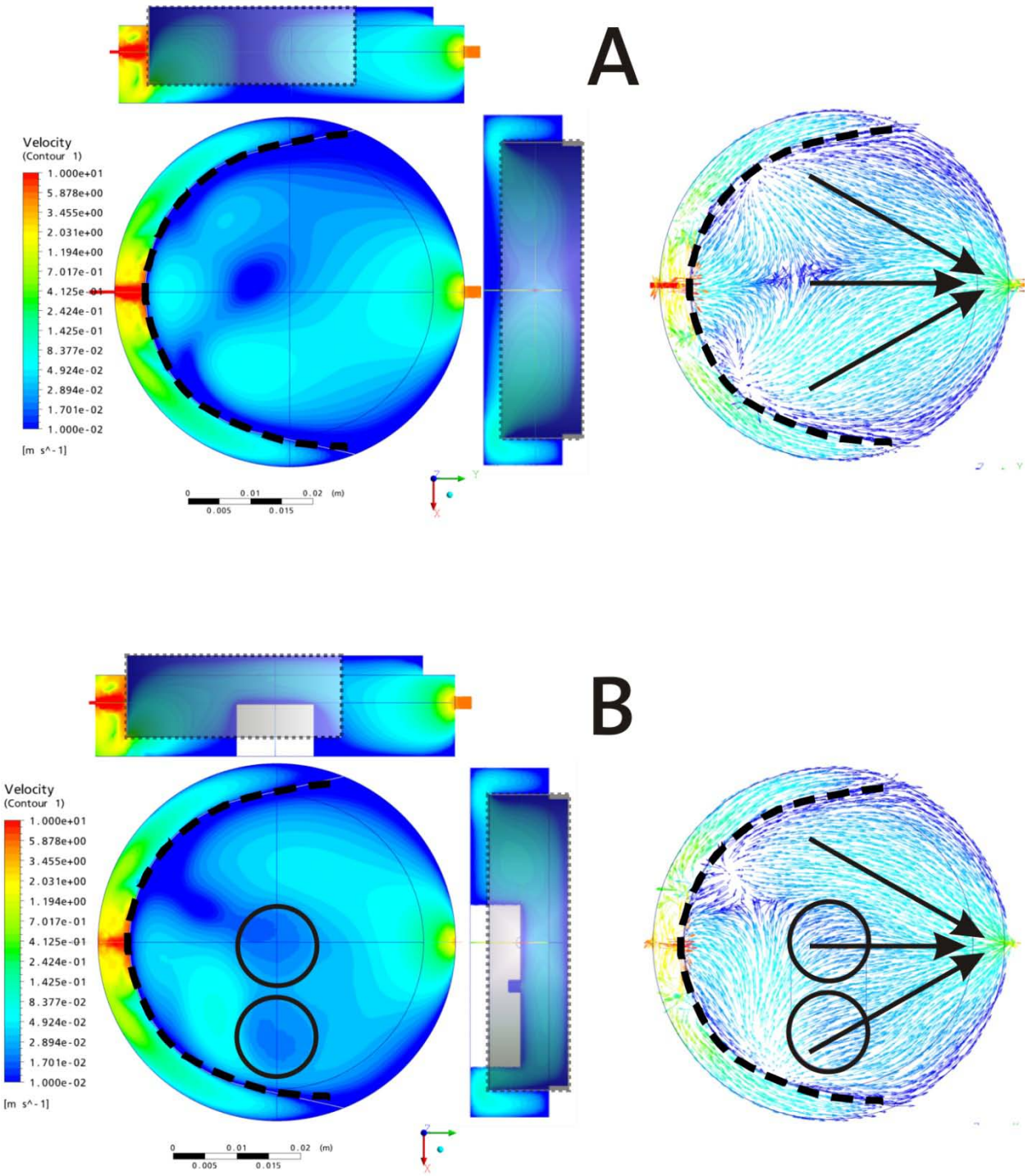

Figure 5: Modeled gas flow velocity and directional vectors of the standard cylindrical ablation cell with an aluminum piece (dashed lines) shielding the jet from the gas inlet leading to a sheet of even gas flow velocity running over the samples (A, no samples). This is observed in the models regardless of the presence of samples (B, two samples).

2.4 Ablation cell for large samples

CFD modelling of the standard cell improved understanding of the gas flows and effects of the cell geometry on aerosol transport. The next step was to design an ablation cell for large samples with optimized gas flows for fast washout. Dimensions of the maximum samples size which can be loaded into the ablation cell was given by the dimensions of the largest piece of stalagmite KRUM-3 (see chapter 7). The outer dimensions of the cell were not as stringent. Restrictions of the weight of the entire ablation cell including the samples were limited by the power of the z-motor of the stage when moving upwards, lifting the weight of both ablation cell and sample. Finally from the prototype to the final version of the cell, optimization was mainly focused towards decreasing the overall weight, while increasing the mountable sample dimensions and incorporating improvements regarding gas flows uncovered mainly through CFX modelling.

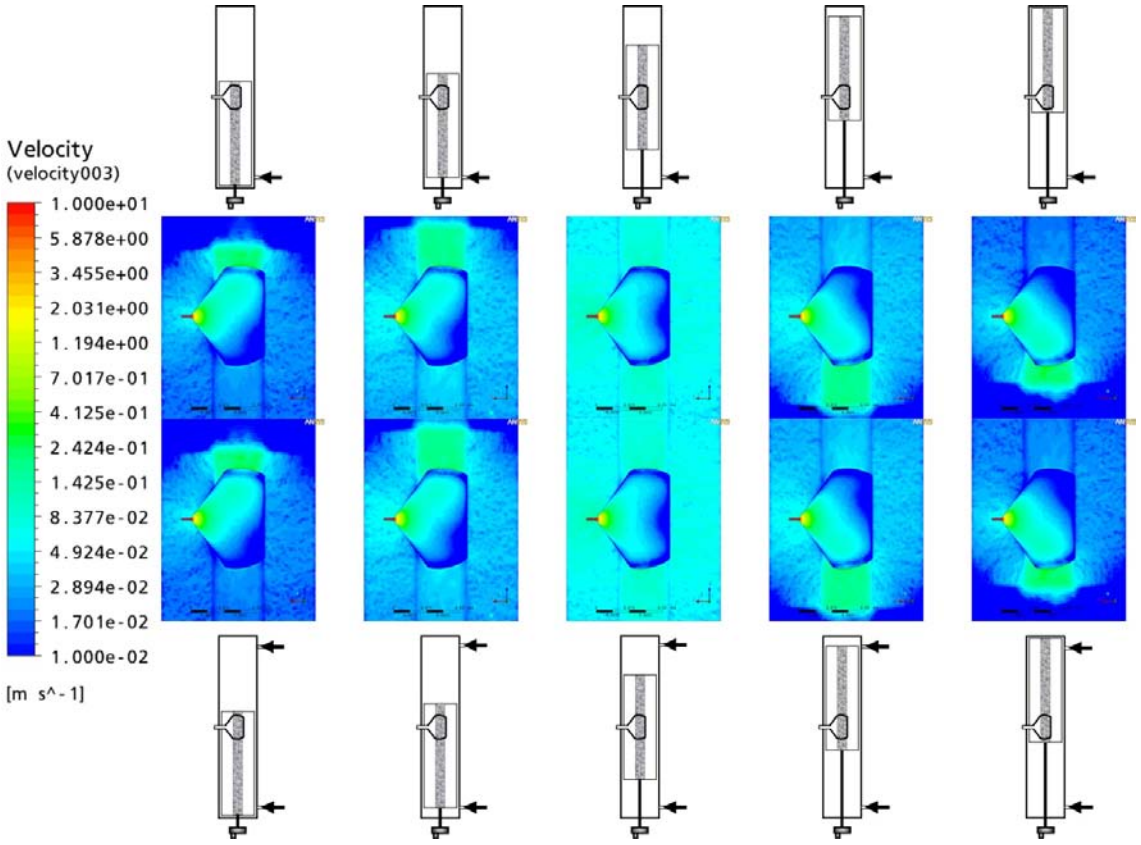

Figure 6: CFX modeling showing the velocity of the carrier gas (He) directly above the sample and at the height of the gas outlet (inset of the effective volume in each frame) for various positions of the sample sled inside the ablation cell. Comparing the effect of one (top row) versus two gas inlets (bottom row) revealed no difference of the gas velocity distribution. However using two gas inlets reduced the purging of ambient gases significantly. The purging is required after changing of the samples and sealing of the cell for the following analysis.

The modeling with one gas inlet versus two inlets did not show changes of the gas flow conditions in the effective volume (Figure 6). However, the experimentally determined time to flush the sample holder area after replacing or changing samples indicated that a single gas inlet increases the time to stabilize the instrument for the next analysis most significantly. Therefore, a second gas inlet was placed at the opposite side of the sample holder. This reduced the flushing time prior to the analysis by almost an order of magnitude. Unfortunately, such effects could not be observed using our approach of modeling, since all models were performed using He only and rinsing time was not implemented.

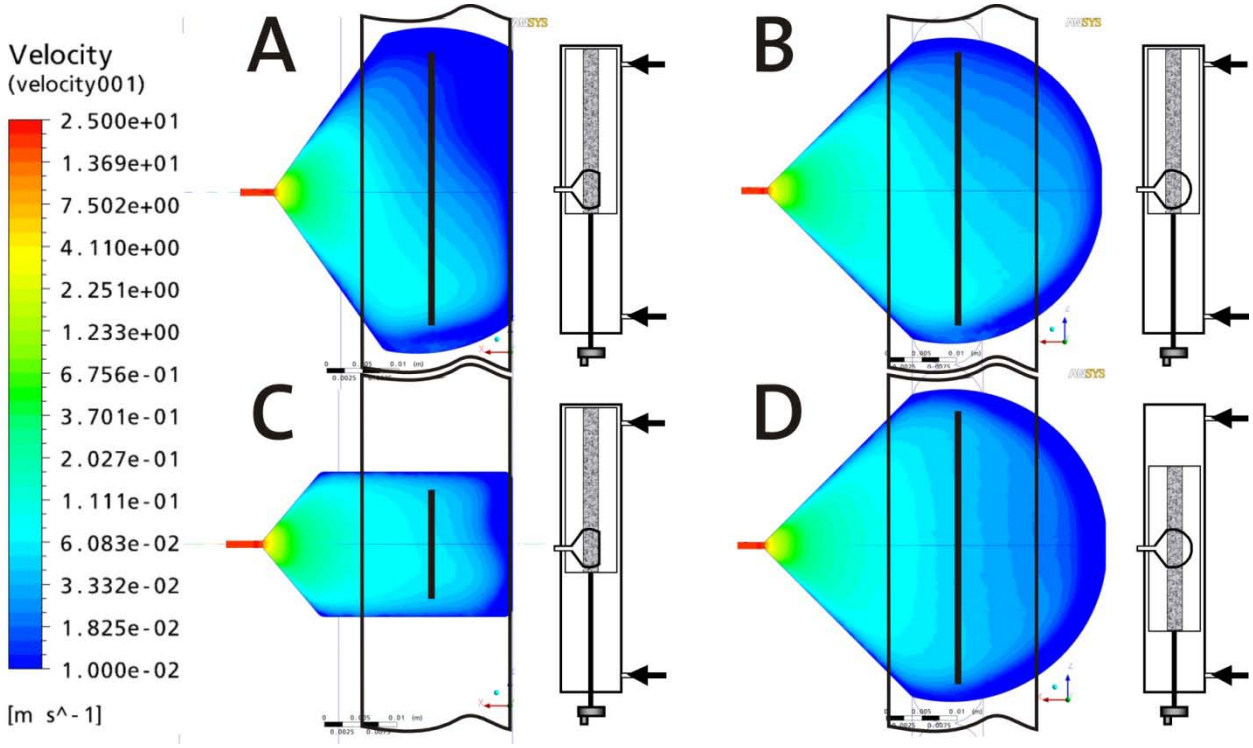

Figure 7: Carrier gas flow velocities at the height of the gas outlet are shown for three different geometries of the effective volume. Location of a typical line scan is indicated and illustrates superior gas velocity distribution of B and C in contrast to A. This was also achieved with configuration C. But this configuration is inferior due to the smaller area available for ablation, i.e. shorter line scans. D shows symmetric gas velocities for the center position of the sample sled.

By increasing the effective volume (Figure 7), the gas flow vectors were in fact optimized. This is contrasting the theory of creating the smallest possible effective volume for obtaining the fastest washout. In fact, this slight increase of the effective volume provides the necessary space for the gas flow vectors to align towards the outlet. Thus the low gas flow edge is further away from the sample surface and not changing the optimized gas flow conditions above the sample surface. The size of the effective volume is not the only measure leading to a fast washout of the aerosol, the effects of suppression of vortices and direction of the flow vectors pointing towards the outlet are more pronounced than the mere volume. A larger volume is also favorable, as it is

difficult to mount several samples and external standards into small volume ablation cells.

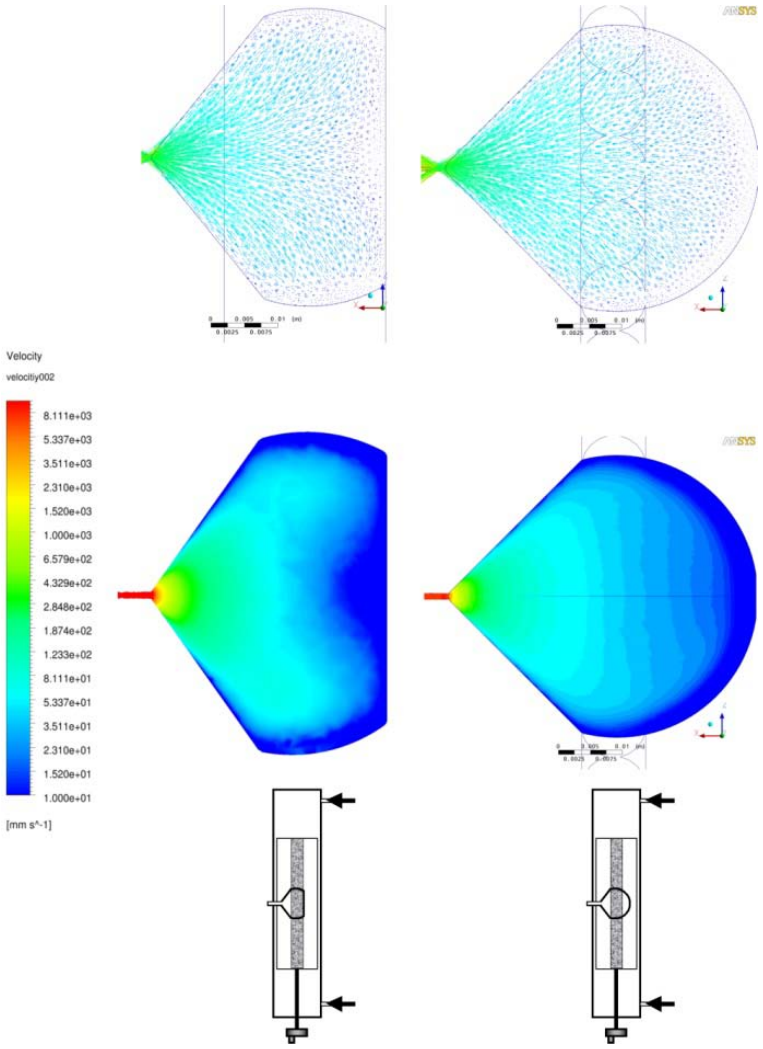

Figure 8: Gas flow vectors (top row) are pointing to the outlet resulting in a favorable configuration for rapid aerosol washout. The larger effective volume (right hand side) distributes gas flow velocity as well as direction of the vectors more homogeneously over the area available for line scanning.

All vectors are pointing towards the outlet which is the most favorable direction for rapid washout of the aerosol (Figure 8). Only a small ring of low gas velocity vectors are pointing upwards instead to the outlet around the effective volume. Due to this observation, line scans were generally not performed at the edge of the accessible volume and a distance of 5 mm from the edge was maintained.

2.5 Low dispersion high capacity laser ablation cell design

A technical drawing of the low dispersion high capacity laser ablation cell (LDHCLAC) is given in appendix A and a detailed description, covering the handling and replacing of spare parts is given in the ablation cell handbook (appendix B). Recesses in the Plexiglas body as well as in the metallic parts were cut out where stability was not impaired (Figure 9), in order to decrease the overall weight of the ablation cell. This had significant implications on the reduction of the physical stress on the microscope stage.

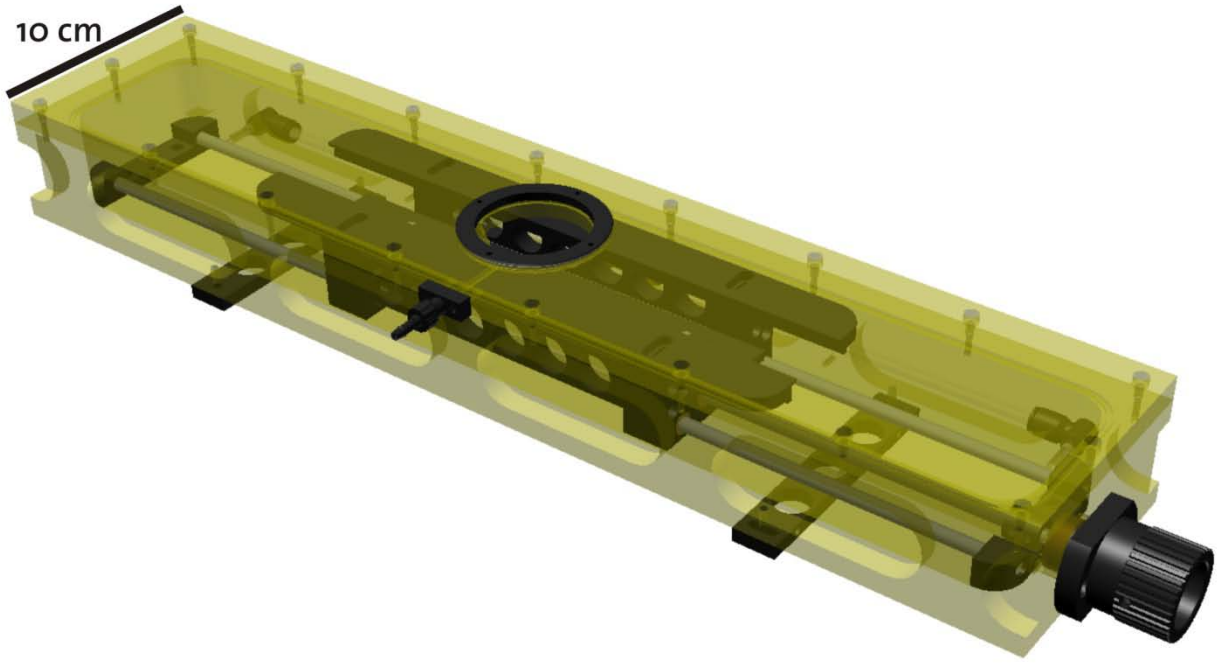

Figure 9: Perspective view of the low dispersion high capacity laser ablation cell.

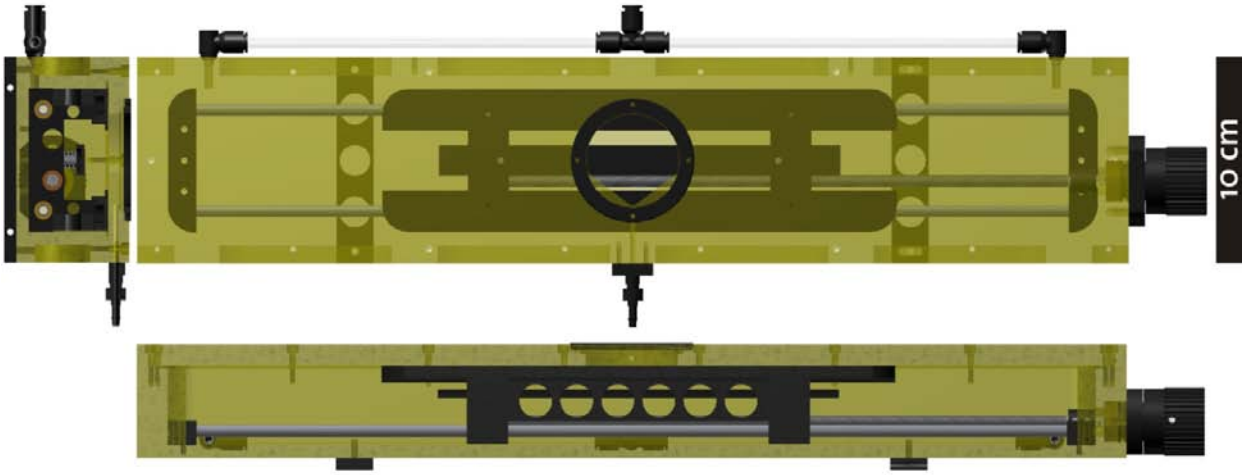

Figure 10: Top view of the low dispersion high capacity laser ablation cell, and sectional views through the ablation window center and through the long axis.

The top view and two sectional views shown in Figure 10, provide an overview of the ablation cell geometry. The sled is mounted on two rails and a spindle for positioning. A clearance regulator connects the sled to the spindle suppressing slip and thereby increasing precision of the movement. The spindle is rotated with a handle from the outside of the cell, allowing to move the sled without opening the cell. Gas tightness of the cell is assured by a custom made rotary shaft sealing, as it was found that O-rings on the shaft are insufficient seals in terms of tightness. Gas inlets are connected to the cell using legris (Parker Hannafin Europe Sàrl, Etoy, Switzerland) gas tube connectors. However, an in-house developed quick tube connector was used at the carrier gas outlet. Experimentally it was found, that a legris connector at the carrier gas outlet provides insufficient leak tightness due to the rigid transport tube material and the necessity to move the cell for line scanning.

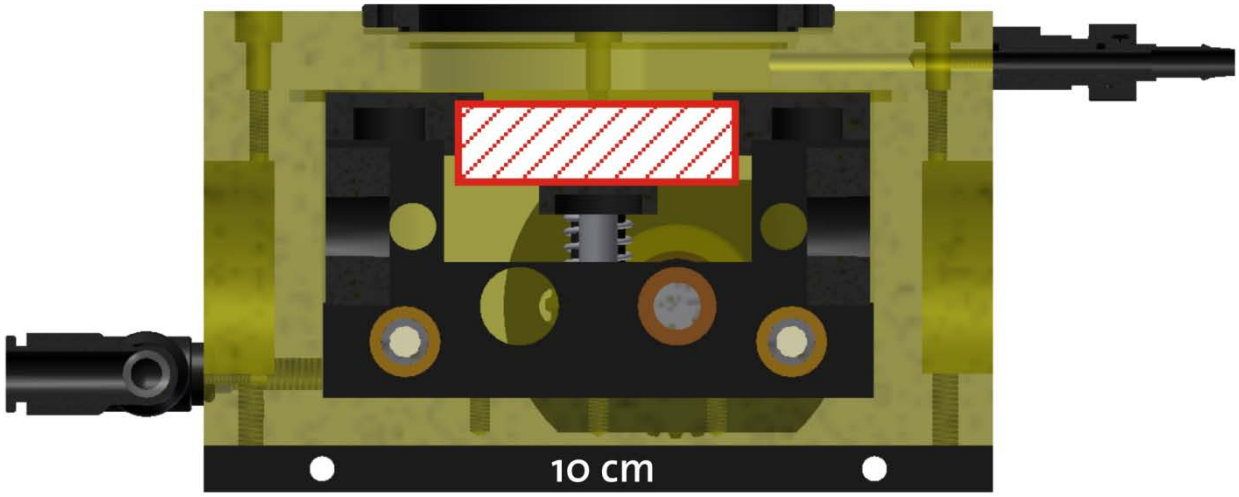

Figure 11: Detail of the sectional view through the carrier gas outlet with a sample (red frame) mounted on the sled. Maximum dimensions for a sample are 230x34x16 mm (LxWxD).

The sectional view through the carrier gas outlet, ablation window and sample sled (Figure 11) illustrates the way samples are mounted. Springs push the sample from below to the correct position on the sample holder, leaving 1 mm of space between sample surface and ablation cell cover. It is recommended that such a flat surface configuration is used for all samples. Only this sample geometry provides the same conditions as used for the modeling. In order to keep gas flows over the surface stable and similar to the models, smaller samples need to be mounted on a sample holder with holes into which they can be placed (e.g. 30 rice grains [22]). Maximum dimensions for a sample or sample holder are 230x34x16 mm (LxWxD). However, by applying small modification to the sample sled configuration provides access to samples with larger dimensions.

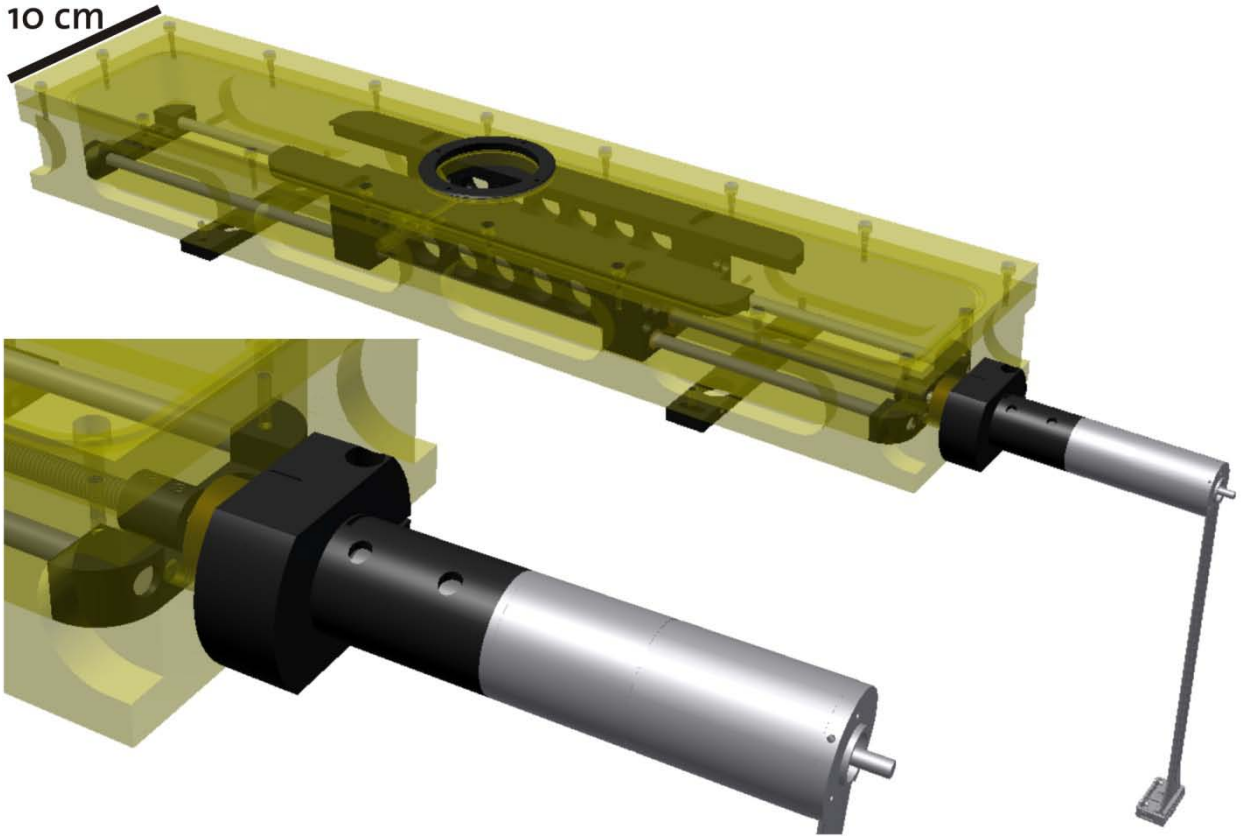

Figure 12: The motor (silver) and motor mount (black) attached to the LDHCL ablation cell for computer controlled movement of the sample sled. The end switches and the controller assembly are not shown.

The final version of the LDHC ablation cell (Figure 12) is equipped with a DC motor (brushless, 12 W, with encoder), planetary gear set 19:1, two hall sensor end-switches (placed outside of the cell with magnets attached to the sled) and an EPOS2 P 24/5 programmable positioning controller (all parts by Maxon Motor AG, Sachseln, Switzerland). A photograph of this system is shown in Figure 13. The motor controls are integrated into the *GeoLasPro* (GeoLasPro248, V. 1.3.7.0, Seatec GmbH, Coherent, Germany) program as a virtual 4^{th} axis of the xyz-stage of the microscope (Figure 14).

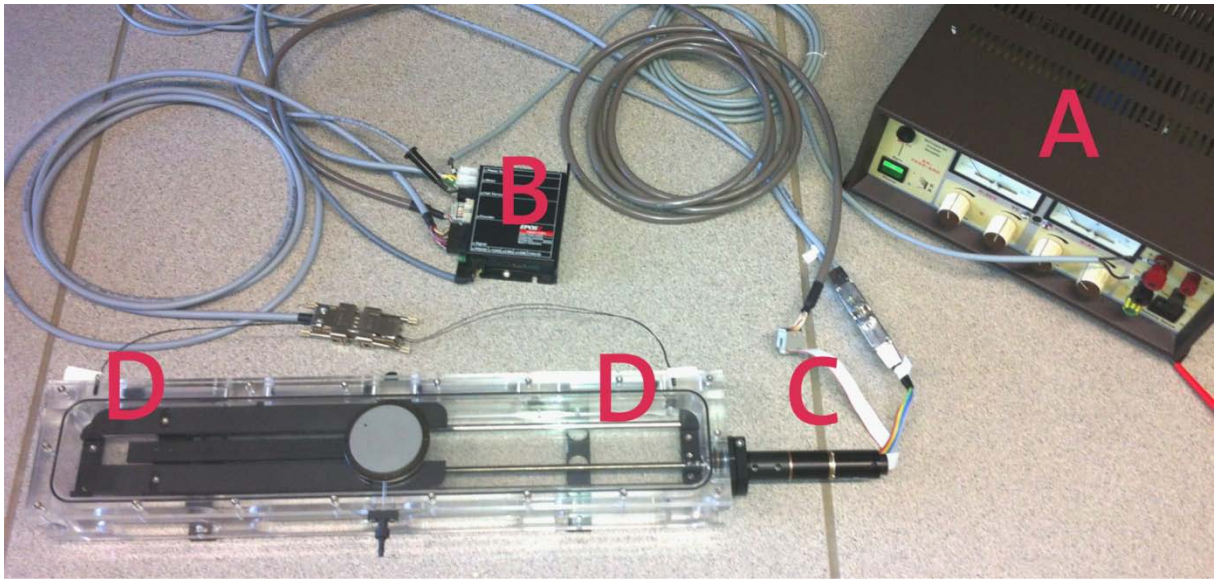

Figure 13: Photograph of the assembled motorized version of the LDHCL ablation cell consisting of the power source (A), controller (B), motor (C), hall sensors (D), and the cables connecting to the GeoLasPro computer.

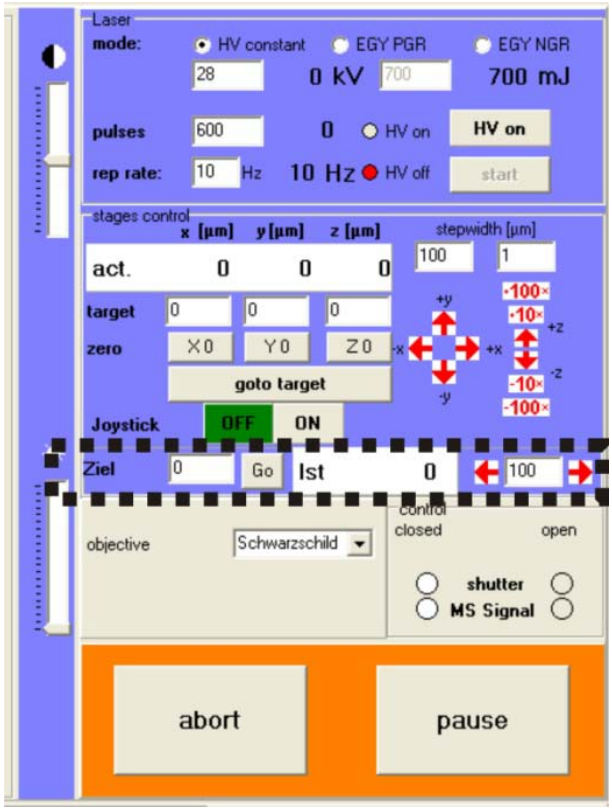

Figure 14: Screenshot of stage control part of the *GeoLas PRO* controller software. The black dashed frame marks the controls created specifically for the ablation cell motor.

2.6 Summary

The CFD modeling provided valuable insight into gas flow dynamics within an ablation cell. Based on these calculations an optimized ablation cell geometry for fast aerosol washout was transferred into a new ablation cell model. The achieved reduction in washout times (complete flushing of the cell interior) was specifically required for profiling and mapping of large, heterogeneous samples. In order to suppress mixing of aerosol generated from distinct laser pulses it was necessary to design an effective-volume geometry (i.e. the volume in which aerosol is generated and transported out of the ablation cell) preventing the formation of vortices. Almost all gas flow vectors homogeneously point towards the carrier gas outlet (having a funnel outline channeling the aerosol), even with sample contours present. The built and experimentally tested ablation cell can be applied for a wide variety of samples and provides significant improvements in fast aerosol washout. Another option of ablation straight inside the transport tube will certainly lead to a much faster aerosol washout (with only in-torch ablation yielding smaller dispersion [64]). However, handling and mounting of samples is difficult and imaging of samples is impossible. Therefore, the current version of the LDHCLA cell represents the optimum ablation cell when compared to other commercially available ablation cells.

Since the optimization was performed parallel to application (see following chapters), some samples were analyzed using earlier ablation cell versions. Therefore, not all aerosol washout times were as good as shown in the description of the final version of the ablation cell.

Furthermore the CFD modeling was also used to modify the standard cylindrical ablation cell to obtain a geometry with gas flow conditions favorable for fast aerosol washout. Therefore, the PTFE seal component was removed and replaced by a newly designed gas channeling system (using a 3D printer). This minor modification creates a homogeneous gas sheet flowing over the samples and the first results indicate a very significant reduction of the aerosol washout time (Dietiker et al. [in prep.]).

3 Experimental tests and qualitative analysis on an electrophoresis gel

This chapter was published in International Journal of Mass Spectrometry, 2011 [105].

High spatial resolution trace element analysis by LA-ICP-MS using a novel ablation cell for multiple or large samples

M. B. Fricker, D. Kutscher, B. Aeschlimann, J. Frommer, R. Dietiker, J. Bettmer, D. Günther, *International Journal of Mass Spectrometry* **2011**, *307*, 39–45.

3.1 Introduction

Laser ablation-inductively coupled plasma-mass spectrometry (LA-ICP-MS) is a widespread technique for analysis of major, minor and trace elements in solid samples with high dynamic range and low limits of detection [61]. Quantitative analysis of elements and isotopes are required in a wide variety of applications (bulk analysis, micro analysis, fingerprinting [20], depth profiling [19], line scans [22–26], isotope ratio analysis [21], and mapping [27,30,31] in many research fields [18] (earth sciences, forensics, gemology, material sciences, life sciences and in industry). In recent years, the detection of metal-containing proteins after separation on polyacrylamide gels has become a frequent application for LA-ICP-MS [130]. Especially electrophoresis in two dimensions provides high separation efficiency for a given sample. However, sensitive and spatially resolved detection is a prerequisite for the successful interpretation [131] of these gels.

The performance of LA-ICP-MS is crucially dependent on the characteristics of the ablation cell. Various investigations on ablation cell design have been carried out on the volume of the cell and transport tube material [21,81], transport efficiency in dependence on geometry [15,36,108], as well as on the applicability of cooled cells for hosting tissues [74], open-contact cell for large, flat samples [93] or double cell configurations with fast washout [78]. However, so far the different designs have not led to the development of an ablation cell, which can host large samples enclosed in an airtight Argon or Helium atmosphere. Since fast washout requires a small volume, a number of small cell volumes or double cells have been reported in the literature. Fast washout and transport of the laser generated aerosol to the ICP have been extensively studied for different ablation cell designs and approaches such as a laminar flow cell [86], cell in a cell [15,36,78,80], using the Venturi effect [84], rotating nozzle [82], cyclonic gas flow [83], and removing the cell by in-torch ablation [132]. Numeric modeling of gas flows [107,110] and particle trajectories [108] in the ablation cell are becoming a valuable source of information for designing and optimizing of new ablation cells for specialized purposes. Some of these small volume cells would be ideal to be placed on large sample holders. However, as indicated by Lindner et al. [133], this requires the design of a specific interface.

The requirement of large ablation cells evolved from a number of applications, where the samples cannot be cut into pieces for analysis, such as historic artifacts, precious objects, corals or stalagmites. For the tightly grown stalagmites, a cutting process would lead to significant loss of information recorded in the sample. For bulk analysis, a short washout of the aerosol is not critical. However, it is essential for analysis with high spatial resolution for scanning and mapping of solid sample surfaces. While in scanning mode, laser ablation runs along a heterogeneous sample (such as sediments [129], corals [23], stalagmites [27,70], biological tissue [30,134], etc.) the composition of the aerosols changes over time and therefore needs to be recorded as a transient signal without mixing of information [19,71,135].

Based on the literature and the variety of samples analyzed in our laboratory, we focused on the development of a routinely applicable ablation cell design for high resolution analyses of large, heterogeneous samples. The parameters of interest included signal intensities (transport efficiency) and stability in dependence of the position of ablation. These studies were carried out using prolonged ablation of profiles across two standard materials. The empirical investigations were furthermore validated by gas flow velocity simulations using computational fluid dynamics (CFD). Finally, we applied the ablation cell to perform imaging of the distribution of a pHMB-derivatised protein after electrophoretic separation using the intensity profile of mercury. As natural ovalbumin contains only S and P (but no metals) for detection with Q-ICP-MS, the artificial introduction of Hg was necessary to improve detection capabilities.

3.2 Experimental

3.2.1 Instrumentation

All analyses were carried out using an ArF excimer laser at 193 nm (GeoLasC, Lambda Physik, Göttingen, Germany), the ablation cell was mounted on a computer-controlled xyz-stage of an Olympus BX51 microscope. The prototype ablation cell was built in-house to host samples with max. dimensions of 230x34x16 mm (LxWxD). The total volume of the cell is around 1 L, whereas the volume, into which the laser aerosol expansion takes place, is only around 13 cm^3. The entire corpus was made from polymethylmethacrylate (PMMA) to provide a small weight (2.2 kg) of the ablation cell, see Figure 15.

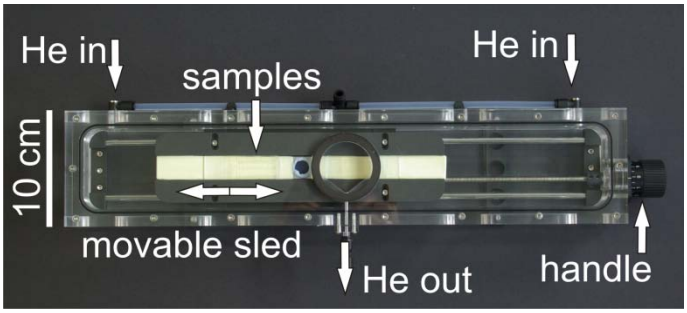

Figure 15: Top view of the ablation cell. During analysis the entire cell is moved by a computer-controlled xyz-stage for LA scanning through the round window in the center. The sample is fixed on a sled within the cell, allowing manual repositioning between analyses without opening of the cell. With the 50 mm diameter cell window, it is possible to scan about 40 mm on the sample before moving the sled manually with the handle. The dimensions of the chamber housing the sled are 450x70x40 mm LxWxD. On this photograph, two halves of a polyacrylamide gel (not stained) and one NIST SRM 610 are mounted on the sled, one ready for ablation in front of the He outlet.

The ablation cell was coupled to a quadrupole ICP-MS (ELAN DRC+, Perkin Elmer, Massachusetts, USA, or Agilent 7500cs, Agilent Technologies, Palo Alto, USA). The ICP-MS was tuned daily for high signal intensity and $ThO^+/Th^+ < 1.5$ %, and operating conditions of the laser and the ICP-MS are summarized in Table 3. A standard cylindrical ablation cell (volume of 63 cm^3, for samples up to 50 mm diameter) used in our labs [109] was used to compare washouts.

Table 3: Operating conditions of both the excimer laser and the quadrupole ICP-MS and list of isotopes (*m/Z*) that were monitored for analyses of NIST 610, JK-2D and the electrophoresis gels.

	NIST 610 cleaning	NIST 610 acquisition	JK-2D	Gel
Laser ablation				
scan length [mm]	5.5	5.5	28.6	35.7
energy density [J cm^{-2}]	6.5	6.5	26	14
crater size [µm]	127	63	90	160
repetition rate [Hz]	1	10	10	20
scanning speed [µm s^{-1}]	47	20	90	50
ICP-MS				
Instrument	**ELAN DRC+**		**ELAN DRC+**	**Agilent**
RF power [W]	1400		1380	1600
carrier gas, He [L min^{-1}]	1.0		1.0	1.0
nebulizer gas, Ar [L min^{-1}]	0.95		0.86	0.75
aux. gas, Ar [L min^{-1}]	0.84		0.75	
plasma gas, Ar [L min^{-1}]	17.0		17.5	15.0
dwell time [ms]	10		10	50
sweep time [ms]	650		208	312

NIST 610
$^{7}Li^{+}$, $^{11}B^{+}$, $^{13}C^{+}$, $^{23}Na^{+}$, $^{24}Mg^{+}$, $^{25}Mg^{+}$, $^{26}Mg^{+}$, $^{27}Al^{+}$, $^{29}Si^{+}$, $^{31}P^{+}$, $^{34}S^{+}$, $^{35}Cl^{+}$, $^{39}K^{+}$, $^{42}Ca^{+}$, $^{43}Ca^{+}$, $^{46}Ca^{+}$, $^{49}Ti^{+}$, $^{53}Cr^{+}$, $^{55}Mn^{+}$, $^{57}Fe^{+}$, $^{59}Co^{+}$, $^{60}Ni^{+}$, $^{65}Cu^{+}$, $^{66}Zn^{+}$, $^{71}Ga^{+}$, $^{79}Br^{+}$, $^{85}Rb^{+}$, $^{88}Sr^{+}$, $^{89}Y^{+}$, $^{133}Cs^{+}$, $^{137}Ba^{+}$, $^{139}La^{+}$, $^{140}Ce^{+}$, $^{141}Pr^{+}$, $^{146}Nd^{+}$, $^{147}Sm^{+}$, $^{153}Eu^{+}$, $^{157}Gd^{+}$, $^{159}Tb^{+}$, $^{163}Dy^{+}$, $^{165}Ho^{+}$, $^{166}Er^{+}$, $^{169}Tm^{+}$, $^{173}Yb^{+}$, $^{175}Lu^{+}$, $^{178}Hf^{+}$, $^{181}Ta^{+}$, $^{208}Pb^{+}$, $^{232}Th^{+}$, $^{238}U^{+}$

JK-2D
$^{13}C^{+}$, $^{23}Na^{+}$, $^{27}Al^{+}$, $^{29}Si^{+}$, $^{31}P^{+}$, $^{32}S^{+}$, $^{34}S^{+}$, $^{53}Cr^{+}$, $^{55}Mn^{+}$, $^{57}Fe^{+}$, $^{59}Co^{+}$, $^{60}Ni^{+}$, $^{63}Cu^{+}$, $^{95}Mo^{+}$, $^{118}Sn^{+}$, $^{208}Pb^{+}$

Gel
$^{13}C^{+}$, $^{29}Si^{+}$, $^{34}S^{+}$, $^{199}Hg^{+}$, $^{200}Hg^{+}$, $^{202}Hg^{+}$

3.2.2 Modeling

To validate the assumptions about the gas flow patterns within the ablation cell, the gas flow dynamics were modeled with Ansys CFX 11.0 [106] using an optimized fine numerical grid of about 1.8 million elements. The fluid was set to Helium at standard temperature and pressure (STP). The boundary conditions, i.e. inflow and outflow were based on experimental data and set to a mass flow of 2.9767x10^{-3} g s^{-1} at 25 °C (1 L min^{-1}).

3.2.3 Characterization

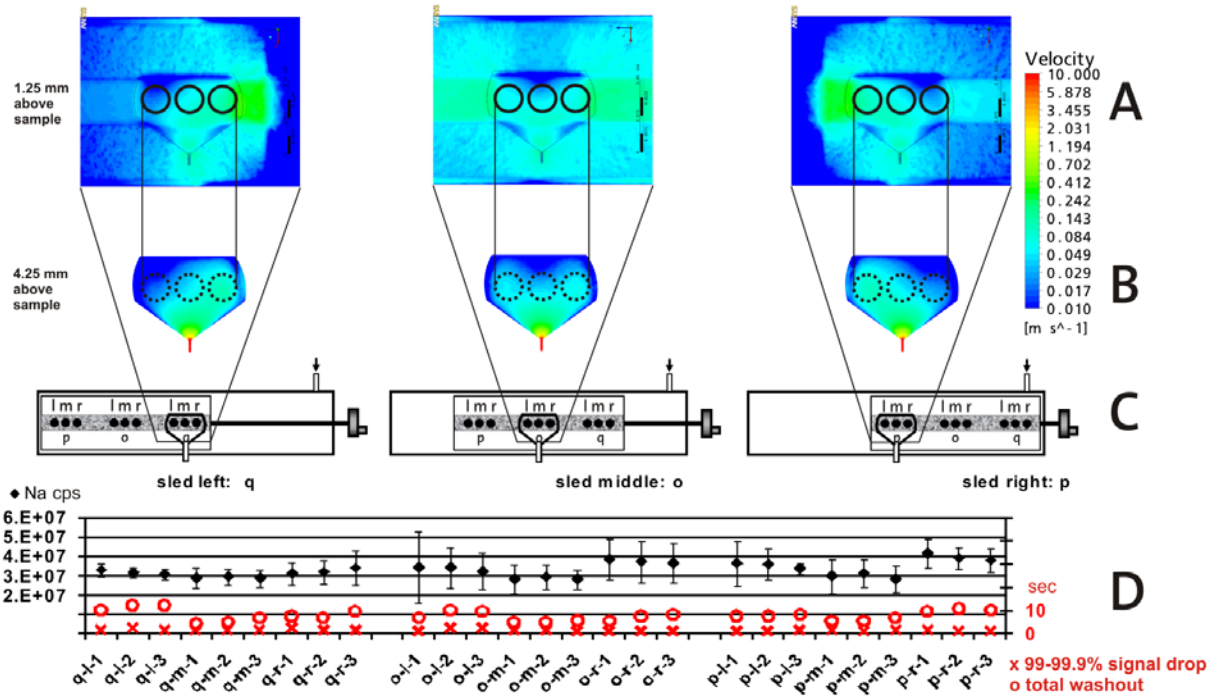

Figure 16: Gas flow models showing gas velocities (m s-1) at the ablation area, 1.25 mm above the surface of the sample (A) and insets (B) displaying gas velocity at the level of the outlet, 4.25 mm. Sketches (C) of the cell indicate the position of the sled and the samples (NIST 610) respectively. Signal intensity [cps] of Na (diamonds) is given in plot (D), three repetitions for each sample at each position (1-3). Aerosol washout time is shown in the same plot (D) for the complete washout (circles), i.e. drop of the signal to background level and for the fast washout (crosses), i.e. drop of the signal of 2-3 order of magnitudes (99-99.9% signal drop).

The design allows fitting large samples without further cutting. For testing the performance of the cell, NIST 610 SRM was placed in a PMMA slab (Figure 16) mimicking the contour of a cuboid sample. Based on this, it was assured that gas flow conditions on the sample surface were close to those used for modeling. The ablation experiments were carried out on three NIST 610 glasses, which were placed into the sample holder underneath the ablation cell window, as illustrated in Figure 17. Line scans were performed three times along the axis in the center of each sample.

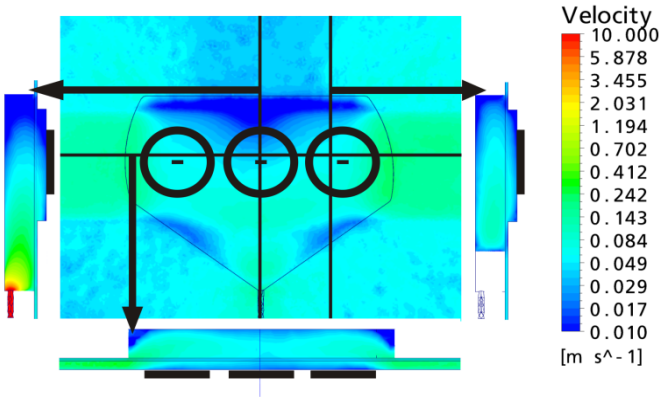

Figure 17: Gas flow velocities (m s-1) modeled using ANSYS. The black circles indicate the location of the three NIST SRM 610. A horizontal and two vertical cross-sections are shown on the sides. The cross-section through the center of the gas outlet (vertical on the left) shows the slightly larger low gas flow area (dark blue) compared to the cross-section on the side (vertical on the right).

They were repeated for 3 positions of the sled, at the end of the cell away from the He inlet (position q), in the center (position o) and at the He inlet (position p), respectively. All observations for signal intensity, stability and washout are based on multielement measurements. The signal of $^{23}Na^{+}$ was selected as a representative for cell evaluation, since Na is monoisotopic with a high concentration in NIST 610. This element provides high signal intensity and is thus very suitable for the determination of the washout time. The steel sample JK-2D was placed in the center of the sled and embedded in the same way as the three NIST 610 samples. Line scans of 28.6 mm length (scan 1 and 2 were shorter, due to geometry) were performed 12 times with a distance of 2.5 mm between the scans, see Figure 18. Each line was scanned twice: the first time for cleaning of the sample surface and the second time for the data acquisition. The steel sample analysis was carried out using two gas inlets enabling more symmetric gas flows and reducing purging time after closing of the cell when samples were mounted. Furthermore, for the measurements on the steel sample and the gel, the volume at the ablation area was increased to a near circular shape (Figure 18B) in order to suppress the low flow zones as observed in the simulations (Figure 17).

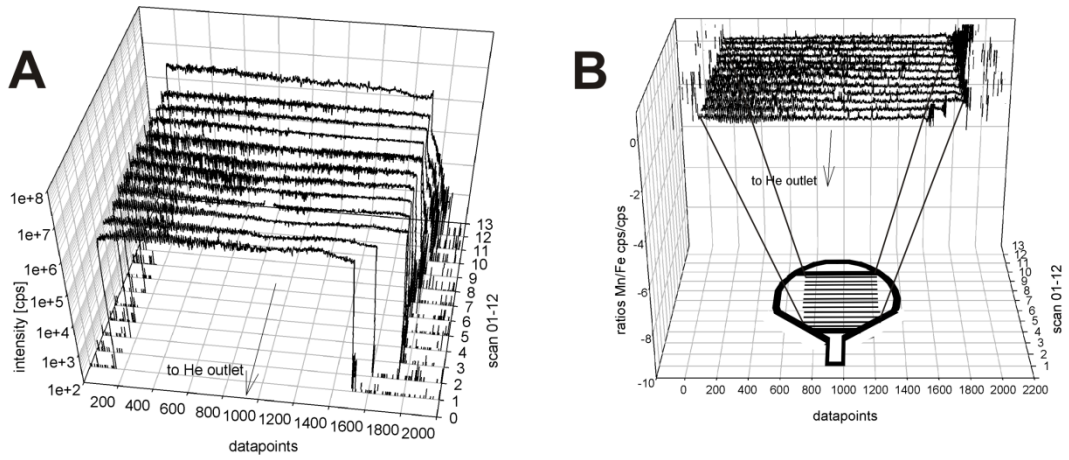

Figure 18: A: Signal intensity map on JK-2D shown for 57Fe+, scan 01 closest to the edge at the outlet, scan 12 closest to the far edge, both with unstable (wavy) signals. The left half of all line scans is noisier than the right half and washout is longer for the scans further away from the outlet. Missing data (middle of the line scan) in scan 04 was omitted due to a hole in the sample surface. The two line scans 1 and 2 are shorter due to the geometry of the ablation cell. B: The intensity ratios of 55Mn+/57Fe+ are plotted for the same line scans as A. The ratios are noisier for the left side than for the right side. All ratios are stable except for scan 12, where ratios slightly increase to the right.

3.2.4 Application

Derivatisation of ovalbumin with p-(hydroxymercuri)benzoic acid (pHMB) was carried out as described elsewhere [136]. Ovalbumin (Sigma Aldrich) was dissolved in 50 mmol L^{-1} NH_4HCO_3 (Sigma Aldrich) in ultrapure water (Millipore, Bedford, USA) to the desired concentration and then incubated with a 10-fold molar excess of pHMB (25 µmol L^{-1} in 0.05 mol L^{-1} NaOH) per cysteine residue. After two-fold ultrafiltration using a 10 kDa cut-off membrane (Millipore, Bedford, USA), the derivatised protein was diluted with 50 mmol L^{-1} NH_4HCO_3. After incubation in the sample buffer (62.5 mmol L^{-1} Tris, pH 6.8, 2% SDS, 25% Glycerol, 0.01% bromophenol blue), 1 µL of this solution was loaded on the gel. Gel electrophoresis was carried out using precast gels (PhastGel 12.5 % separation gel, dimensions 43x50x0.45 mm, GE Healthcare) on a PhastGel electrophoresis unit (GE Healthcare) for 30 minutes at 250 V. Following the procedure described by Raab et al. [26], the gels were shaken in glycerol for 2 minutes, to exchange remaining water before drying at 70 °C for 2 h. The exchange of water to glycerol was necessary to avoid deformation or breaking of the gel during drying. For laser ablation, the gels were divided in two pieces along the middle of the chromatographic axis, fixed onto a glass slide with double sided tape and mounted into the ablation cell together with a NIST SRM 610 for tuning of the ICP-MS. For comparison, one gel was stained using Coomassie Blue.

3.3 Results and Discussion

3.3.1 Modeling

Modeling of the gas flow velocities in the cell suggested non-symmetric gas velocities in the ablation area, when ablating at different positions of samples and sample holder. Symmetric gas flows - which are favorable for analysis - were observed only in the center position of the sled. All measurements on NIST 610 were performed using a single gas inlet in one corner of the cell (Figure 16C). Surprisingly, simulations with a single or a second He gas inlet, respectively, revealed only minor differences in the simulated gas flow pattern. However, a second gas inlet in the other corner drastically decreased purging time of ambient air after opening of the cell for sample replacement. The simulations of the sled positions left (q) and right (p) are nearly symmetric. However, intensity of the signals is more stable and RSDs of the signals are smaller for the left (q) position when compared to the right (p) position (Figure 16D). This may be due to low transient changes in the gas flow pattern. Such are not considered in a steady state CFD, and could be different between the two sides with only one gas inlet. The residence time of the aerosol inside the transport tube (90 cm) was calculated to be 680 ms and the gas velocity in the slow flow regime was approximately 1 cm s^{-1}. Depending on the position of the ablation, the distance travelled by the aerosol from the ablation spot to the transport tube can be up to 4 cm. On average, this yields a response time of 1-2 s from starting the ablation to detection of the signals.

3.3.2 Washout

The washout of the ablation cell and the transport of the laser generated aerosol to the ICP are crucial parameters for main and trace element analyses with high spatial resolution, as mentioned above. Hence, it should be as short as possible to avoid mixing of the aerosols from different spots and therefore maintain information from the sampling position. This is optimally achieved with a laminar gas flow between sample surface and ablation window with gas flow vectors pointing towards the gas outlet at all positions [17].

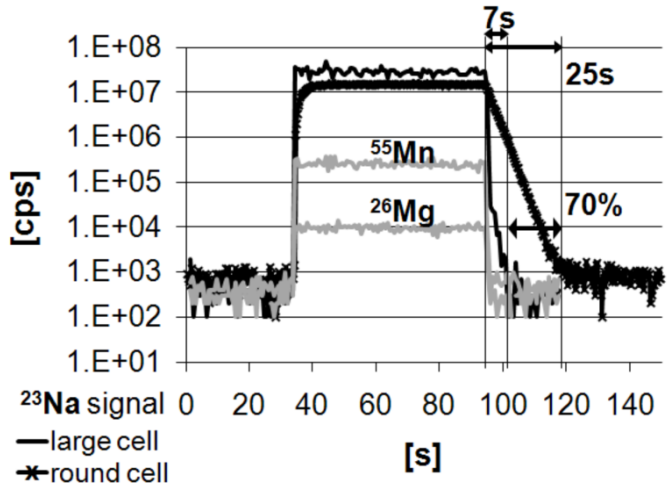

Figure 19: The comparison of the aerosol washout after 60 s of LA illustrates the different behavior of the two cells for rise and decay of the signal. The washout is 70% faster in the large cell compared to the standard (cylindrical) cell [109]. Two other signals (Mn and Mg) with lower intensities are plotted as examples for fast washout of trace elements in the large cell.

The total volume of the cell seems to be of minor importance as long as the gas flows under the ablation window (ablation site) are favorable for fast washout, as indicated by the modeling. It appears that the washout process of the aerosol involves two processes, here referred to as fast washout and slow washout (Figure 19). The fast washout is a sharp decrease in signal intensity, by 2-3 orders of magnitude (to signal intensities as low as 0.1-1%) within 1.3-2.6 s after the last laser pulse. The slow washout requires significantly more time (up to 10.4 s) and accounts for the time required for the signal to reach the background intensities (Figure 16D). Arrowsmith and Hughes [36] have explained such long washout with aerosol that escaped the ablation plume entrainment device (the inner cell in their study). As a result, a small quantity of aerosol is dispersed into the outer cell volume and requires more time (more than 14 min in their experiment) to be washed out completely. There is no inner cell in our setup; hence, the slow washout might be due to particles that are thrust away from the outlet upon ablation. These particles end up in a slow gas flow regime, resulting in a longer washout. Dispersion of the aerosol in the transport tube [17,72,81,133] also contributes to this effect, at least to some extent. However, the major contribution to signal dispersion and washout is related to processes within the cell. We determined for our setup a complete washout (signal intensity down to background level), which includes the fast and the short washout time in the order of 4.6-12.4 s. The two extreme positions q-l and p-r (Figure 16D) feature the longest washout time, as for these configurations ablation takes place in low gas flow areas as indicated by the simulations. The difference in washout between these two cell configurations can be explained by two parameters: A) The high gas flow velocities are pointing towards the gas outlet in the new cell configuration and B) the total volume of the cell for aerosol expansion is 2.5 times smaller than for the standard configuration as discussed in Koch et al. [17].

The washout of the new cell was compared to the washout of the standard cylindrical ablation cell [109] with a washout time of approximately 25 s (Figure 19). The washout of the new cell was determined to be 87% faster for the first 3 orders of magnitude of signal reduction in comparison to the standard cell.

3.3.3 Intensities and RSDs

The overall variability in signal intensities (signal height) measured within the cell was 11.5 % RSD and showed no indication for reduced transport efficiency in comparison to the standard cell. The signal intensities were 11.8 % lower when placing the sample directly in the center in front of the gas outlet (q-m, o-m, p-m). The position of the sled showed no influence. However, the intensities were 1.6 % and 10.2 % higher for the two other samples at positions l and r (Figure 16D), respectively. This may be explained by the lower gas flow velocities (between 2 and 3 times lower) in the center. Therefore, the aerosol generated there is transported slower than that generated in a fast flow area. Optimum cell designs need to offer a more uniform flow pattern and thus, aerosol transport at any position within the ablation cell. Constant gas flows in the entire ablation area and all flow vectors pointing towards the outlet would be ideal. They could prevent the creation of vortices that are prone to trap the aerosol, which leads consequently to an increase in washout time in certain regions. However, as shown by the results (Figure 16), the asymmetric low gas flow has almost no influence on signal intensity (samples l and r), whereas the complete washout is most significantly influenced (Figure 16D).

The experiments indicate a dependence of the signal on the sled position. When the sled is on the far side from the He inlet, signal intensity is more similar and stability of the signal (RSD) is higher. In that position signal RSDs are lower than 20 % in 8 out of 9 experiments. The RSDs become larger for those analyses in areas with faster gas flow, e.g. the center position of the sled (symmetric gas flow) leads to signals with higher RSD values (between 20 and 30 % and for one particular measurement higher than 50 %) as indicated by the o-l analyses (see Figure 16). During three successive measurements with this set-up, the signal for the first measurement (o-l-1) showed a high RSD due to a periodic 'wavy' variation [78,137] described as spectral skew. For the second run within the same ablation scan (o-l-2) the spectral skew was smaller and vanished for the third run (o-l-3) when the signal showed mainly random variation. This may be due to changes in the expansion properties of the ablation plume, since each of the three scans ablates deeper into the sample, thus the plumes of the three scans spread into different gas flow regimes for each of the scans. Other possible factors can be vibrations of the sample from the xyz-stage, or varying flow pattern in the course of analysis resulting in subtle pressure waves reaching the ICP. The influence of pressure oscillations on the ICP-MS signal have been reported by Hirata [138].

3.3.4 Imaging

Based on the experiments and optimization process, a second gas inlet was added to the final configuration of the cell. Twelve line scans were performed across the surface for monitoring signal stability and washout in dependence on the sampling position. The following analyses were carried out using two He gas inlets with equal gas flow rate of 0.5 L min^{-1} each, a total of 1.0 L min^{-1} He. This change led to a signal stability in the order of 13-28 % RSDs for the left side and 6-18 % RSDs for the right side, if the line scan would be split in the middle (Figure 18). The dimensions of the steel CRM JK-2D are close to the area accessible by the laser through the ablation cell window without moving the sample sled. Scan 01 is close to the sample holder, where irregular gas flows cause some fluctuations in the signal intensity. Furthermore, the signal intensity for Scan 12 is twofold higher than that of Scan 11 and decreases along the line scan, because it is as close as 0.5 mm to the other sample holder (Figure 18A). This indicates that measurements should not be performed close to the sample holders. As shown in Figure 18B, the ratios of $^{55}Mn^{+}/^{57}Fe^{+}$ are stable along the line scans, except for Scan 12, where this ratio increases. In conformity to the intensities, also the ratios of $^{55}Mn^{+}/^{57}Fe^{+}$ are noisier for the left side (average over 12 line scans: 0.50 ± 0.04, RSD: 8.2 %) compared to the right side (average over 12 line scans: 0.46 ± 0.01, RSD: 2.4 %). A slight difference in the two gas flows might be a source of oscillation, which causes a resonance within the cell. This effect was reproducible when the direction of the scan was inverted which indicated that the ablation process is not responsible for these oscillations. It is possible that a standing wave is created either by the shockwave of the ablation or by unequal division of the carrier gas upstream of the cell by the T-fitting. The reason for this phenomenon is not yet fully understood. The washouts for the scans that are further away from the outlet are considerably longer (Figure 18A) than for those scans close to the outlet. As indicated by the modeling, a slow gas flow regime at that position may slow down aerosol in a dynamic trap, resulting in slower washout.

Among the elements that were monitored (Table 3) during the analyses of JK-2D, it was found, that Al and Pb are distributed heterogeneously (Figure 20C) within the sample, which is in accordance to the findings reported by Wiltsche and Günther [57].

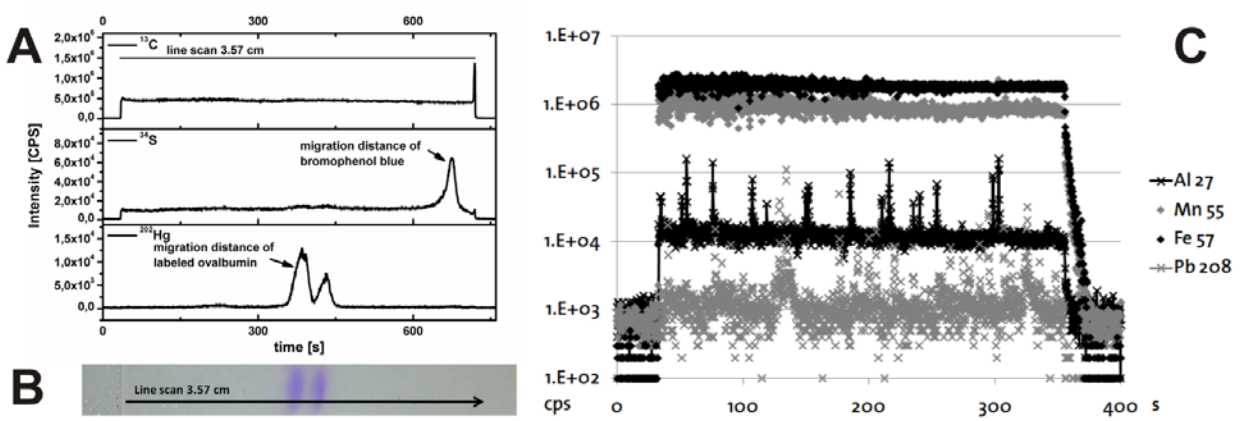

Figure 20: A: Signals of a line scan on the gel of 13C+, 34S+, and 202Hg+ containing Hg derivatized ovalbumin is shown, with the beginning of the separation gel set as starting point. The transient signal of 13C+ as a matrix element is constant during the line scan. The migration distance of bromophenol blue is indicated by the 34S+ signal (ca. 700 s). There are two clearly separated signals visible in the 202Hg+ trace, indicating two different species present in the derivatised ovalbumin (signals at 380 and 450s, respectively). The peak at the end of the 13C+ signal comes from short ablation of tape that was used to hold the gel in place. B: Picture of the Coomassie blue stained gel for comparison with 1 mm between the two protein bands. C: Plot of sgnals of scan 09 on JK-2D. Fe and Mn are homogeneously distributed in the steel standard (but noisier for the left side) while Al (84% RSD) and Pb (256% RSD) are inhomogeneously distributed.

3.3.5 Application of the ablation cell

For the ablation of gels, line scans over the entire separation gel length were performed (35.7 mm length). The beginning of the separation gel was defined optically, whereas the final migration distance of bromophenol blue as a marker could be traced by the $^{34}S^{+}$ intensity. Figure 20A shows the distribution of mercury within the gel. Comparison of Rf values between the stained gel and LA is in good agreement. Although the samples contained ovalbumin only, two separated signals were observed. As both signals are also observed in the underivatized protein (see Coomassie stained gel, Figure 20B), it can be concluded, that there is more than one species present in ovalbumin (for example due to phosphorylation or glycosilation), which is consistent with previous studies [136,139]. Two forms of ovalbumin were separated with a chromatographic resolution of R=1.1 (FWHM). As shown in the previous experiments, scanning from left to right in the cell gives a slightly higher RSD (4-5 %) for matrix elements, in this case $^{13}C^{+}$. The washout for $^{13}C^{+}$ was accomplished within 8 s from $1.4x10^{6}$ cps to $1.8x10^{4}$ cps background. This is longer than for particle transport, which suggests that washout of formed gaseous species of carbon [140] follows different laws than that of particle aerosol.

3.4 Conclusion

A large ablation cell capable of holding large objects was designed, built and tested successfully with three different sample types (glass, metal, organic matrix). It is shown that this ablation cell is able to provide high spatial resolution data of main and trace elements as well as hosting of large samples. A fast washout is achieved by restricting the effective volume for the expansion of the laser-generated aerosol at the ablation site with a geometry favouring laminar gas flows.

The source of the spectral skew and noisier half of the signal remains to be investigated. With this large ablation cell, it was possible to mount two electrophoresis gels simultaneously for the acquisition of Hg profiles in a gel. This allowed the detection of the separated protein and the determination of retention factors. The achieved resolution was limited by the resolution of the gel (and the large diameter of the bands), but such a large cell was necessary for hosting these large samples. Using this cell for imaging of the steel standard, we are able to detect small inhomogeneities (Al and Pb hotspots) that are present in the sample.

The major advantages of this cell design are the fast washout and the possibility to place either a number of samples or a large one into the sample holder. This allows fast switching from standards to the sample of interest and reduces the current necessity of cutting samples (drilling cores, sediments, corals, tree rings, etc.). Therefore, this type of ablation cell allows the analysis of a batch of samples without opening of the cell between analyses [141], which is promising for further automation of the technique. The motorization of the inner sledge to move the sample along one single ablation position is currently in progress and will contribute to improve the stability of the signal intensity.

4 LA-ICP-MS data reduction program STALQUANT for bulk analysis, profiling, and mapping

The work presented in this chapter resulted from collaboration with Thomas Philippe, Laboratory of Inorganic Chemistry, ETH Zurich, who wrote the Python code and Daniel Tabersky, Laboratory of Inorganic Chemistry, ETH Zurich, who helped to check formulas and design user interface.

4.1 Aim

After the development of the large LA cell (LDHCLAC [105], chapter 2.5) within this thesis, it became feasible to analyze large samples. Performing a large number of line scans across the surface yields the trace element profile of a sample (chapters 6, 7). Parallel line scans can be used for mapping (chapter 8) of element distribution of the sample surface. Nonetheless, assembling these short line scans to obtain a profile is tedious, time consuming and prone to calculation errors (e.g. when copying data from one application to another and amongst operators). Thus, the necessity of a software package to increase efficacy of such type of analyses emerged, with the main capability to rapidly quantify every data point of a spatially-resolved analysis with internal standardization as well as normalization to 100 wt% of the respective element-oxide. Currently available LA-ICP-MS data reduction packages such as Glitter [142,143], Iolite [143,144], IMAGENA [145], etc., do not meet all of these requirements within one program. Therefore, STALQUANT was specifically developed for rapid quantification of the raw data acquired within the large LA cell, i.e. profiling and imaging. However, it

swiftly handles also other applications, such as bulk analysis of solid samples and analysis with all other types of ablation cells.

Major attributes for this software are an intuitive user interface and easy data handling as well as increased efficiency in data reduction and thereby reducing user errors. With the effortlessly operated graphical user interface, handling of STALQUANT follows a straightforward procedure:

a) import raw data

b) set parameters

c) save project

d) calculate

e) export results

STALQUANT works with transient signals obtained from homogenous as well as heterogeneous samples to quantify the bulk concentration or 'data point per data point' (BORE) and assembles the results to yield a profile or map across a heterogeneous sample. The output text files provide the user with the option to use any program for further calculations, plotting and presenting the results. Consequently the program does not attempt to produce result plots or maps.

On the other hand, STALQUANT was not designed for quantification of fluid inclusion nor dating applications, for such data analysis, the user is referred to SILLS [143] and AMS [143] for fluid inclusion analysis, and UPb.age [146], LAMTRACE [143], GLITTER [143], ComPbCorr [143], LamDate [143] respectively for dating, most of which are summarized in [143].

4.2 Program

STALQUANT was written using the Python [147] programming language, an open source project running in several operating systems (Linux/Unix, Mac OS X, MS Windows), using appropriate Python interpreters.

The quantification protocol of STALQUANT is entirely based on calculations reported by Longerich et al. 1996 [66] and contains many useful features of LAMTRACE [148], such as linear interpolation between external standards to correct for instrumental drift, etc. However the following crucial features are not limited using STALQUANT:

a) number of data files in a series

b) number of series processed simultaneously

c) number of isotopes monitored by the MS

d) number of data points per file

e) different IS possible for the data files within a series

External standard acquisition in pairs at the beginning and at the end of a series are mandatory for quantification using STALQUANT. However, the program considers additional external standard acquisition at any position within a series as long as they are acquired in pairs. Moreover, it allows assigning quality control measurements (i.e. analysis of a well known reference material as a sample for validation) within a series. These are calculated as samples during bulk quantification but are ignored for all BORE calculations, as they are used for validation purposes only.

The program comprises four tabs, to be followed from left to right in a comprehensive manner. Furthermore, these tabs comprise frames to be followed from left to right.

In the first tab *parameters* detailed information such as performance and acquisition parameters of the laser and the ICP-MS are entered (Figure 21). The laser energy density is calculated in real-time as soon as crater size and energy values are entered. Values for scanning speed and sweep time are needed to convert time-domain signals to distance-domain concentrations. All information given here will be saved together when saving the project and exporting the output for quality and data management consideration.

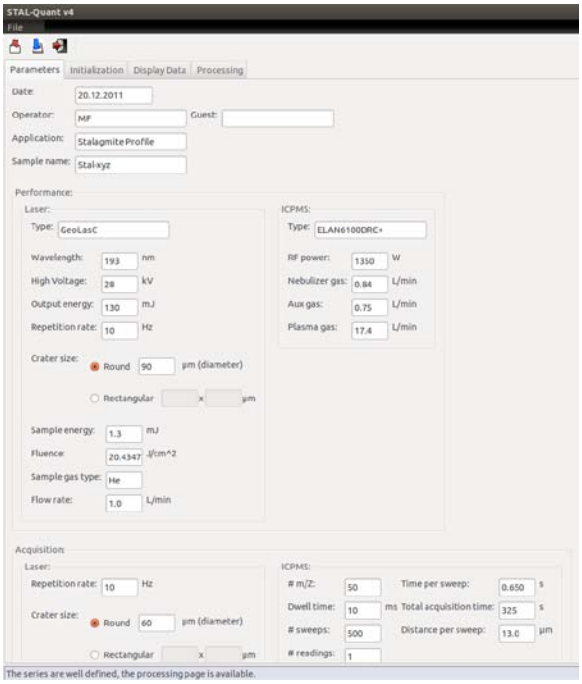

Figure 21: The Parameters tab comprises areas to enter information about the instrumental settings of both laser ablation and ICP-MS.

Transient signals as raw data (currently: PE ELAN6x00, Agilent7500, Spectro MS) are imported in the *initialize* tab (Figure 22A). External and internal standards are selected (Figure 22BCD) before proceeding with the next tab.

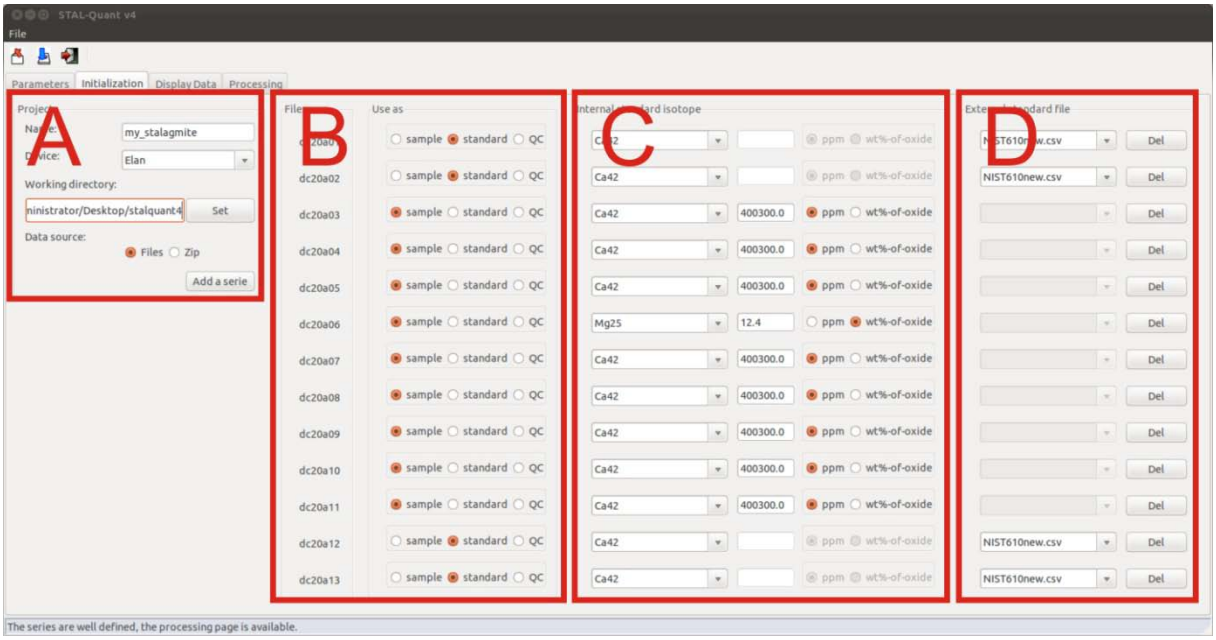

Figure 22: The initialization tab comprises areas to enter information about the project (A), a list of the imported data files including a label as sample, external standard or quality control (B), selection of the internal standard and concentration (C), and the selection of the type of external standard used (D).

The *display data* tab is used for selecting the intervals of background acquisition and laser ablation. This is accomplished by three different ways: clicking onto the plot (Figure 23B), clicking into the raw data table (Figure 23D) or entering time values in Figure 23E. When all intervals were selected, the project must be saved, because after this step (in the *processing* tab) no further parameters will be included in the saved project file. The project file contains all imported raw data files (unaltered) and all the information and selections given up to this stage.

Figure 23: The display tab comprises a list of the imported data files (A), the plot area of the selected data file (B), the list of the isotopes to be plotted (C) including a function to generate and plot isotope ratios from the raw data, a table of the raw data (D) of the selected data file, and the selection of the interval variable to be changed (E). Ablation intervals can be chosen by clicking either in B or D, as well as entering time values manually in E.

In the last tab *processing* options for the calculations (such as the choice of the estimation of limits of detection (details below) and which elements/isotopes are to be included in the 100 % wt normalization [68,149]) are selected, before proceeding with the calculations (Figure 24C). When the calculations for a series are finished, the desired output files are to be selected (Figure 24D), the output units (wt % of oxide or ppm) for each isotope chosen and then the files are exported. The exported file contains all of the selected results. Archiving such information with the results is crucial for data management, as it allows reconstruction of what values were used during each individual calculation, because such values can be changed in the program code, their reproduction is inevitable for proper quality management.

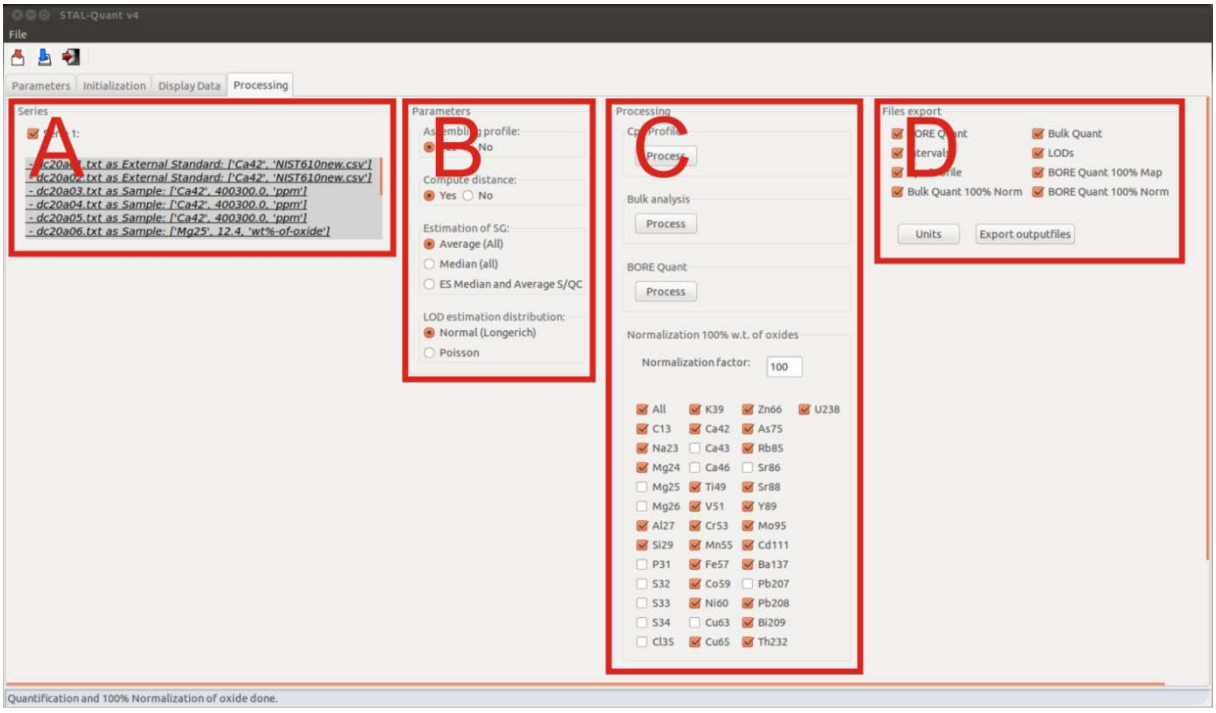

Figure 24: The processing tab comprises an area for selecting the series to be processed (A), selection of mathematical parameters (B) vital for the calculations, several buttons (C) that trigger the respective calculations, and a selection of what types of results are to be exported (D).

4.3 Calculations

All calculations throughout the program are performed using cps and µg g^{-1} units, i.e. ppm, except for the normalization to 100 wt% of element-oxides, for which the concentrations are converted to the respective oxides.

Quantification is based on formulas reported by Longerich et al. [66], i.e. identical to the formulas used within LAMTRACE [143]. Absolute element concentrations are obtained using internal and external standardization, summarized below. To correct for instrumental drift (assumed linear on the data file acquisition time scale), the external standard signal intensities are linearly interpolated between the two external standard data file pairs, i.e. a series. The BG-subtracted and abundance-normalized intensity (I_X^{ES}) of all data files in a series are plotted on an integer timeline to run a linear regression through the four ES values of each analyte x. The time-integer of the data file is inserted into the regression linear equation to compute the interpolated value of I_X^{ES} which is used in the quantification equation (Equation 1).

Equation 1

$$C_X^{SMP} = C_{IS}^{SMP} \cdot \frac{I_X^{SMP}}{I_{IS}^{SMP}} \cdot \frac{I_{IS}^{ES}}{I_X^{ES}} \cdot \frac{C_X^{ES}}{C_{IS}^{ES}}$$

- C_X^{SMP} Final result, concentration of analyte x in sample
- C_{IS}^{SMP} Concentration of internal standard in sample (obtained from independent measurements)
- I_X^{SMP} Signal of analyte x in sample (BG-subtracted, abundance-normalized)
- I_{IS}^{SMP} Signal of internal standard in sample (BG-subtracted, abundance-normalized)
- I_{IS}^{ES} Signal of internal standard in external standard (BG-subtracted, abundance-normalized, linearly interpolated)
- I_X^{ES} Signal of analyte x in external standard (BG-subtracted, abundance-normalized, linearly interpolated)
- C_X^{ES} Concentration of analyte x in external standard (certificate of ES)
- C_{IS}^{ES} Concentration of internal standard in external standard (certificate of ES)

For bulk quantification the background-subtracted and abundance-normalized average signals are inserted in Equation 1, whereas for BORE quantification each data point of the SG interval (background-subtracted, abundance-normalized) is quantified individually to obtain a distribution profile. In case of the presence of spikes are hampering result's quality, it is also possible to use median instead of average signals (Figure 24B). The median is more robust against outliers than the mean.

Ongoing discussions on limits of detection (LOD) estimation considering normal distribution (ND) or Poisson distribution (PD) have lead to the incorporation of several formulas into STALQUANT and let the operator decide upon which one to use. The LOD in LA-ICP-MS is a function of the standard deviation of the background (blank) measurement and the instrument sensitivity. As it is common in LA-ICP-MS to have close to or zero backgrounds for the heavy isotopes, it is important to employ the proper statistics to estimate the standard deviation of the background. For zero or close to zero counts the standard deviation of the background follows counting statistics, i.e. Poisson distribution. In Figure 25 the four cases for LOD estimation are listed. The user defines whether the LODs are to be estimated using Normal or Poisson distribution. STALQUANT then uses the corresponding formula for the BULK and the BORE calculations.

	BULK	BORE
ND **Normal distribution**	$\mathrm{LOD_x} = \frac{3\sigma_{\mathrm{BG,x}}}{\mathrm{S_x}}\sqrt{\frac{1}{m}+\frac{1}{n}}$	$\mathrm{LOD_x} = \frac{3\sigma_{\mathrm{BG,x}}}{\mathrm{S_x}}$
PD **Poisson distribution**	$\mathrm{LOD_x} = \frac{3.29\cdot\sqrt{\mu_{counts,BG,x}}\cdot\frac{1}{\sqrt{n}}+2.71}{\mathrm{S_x}\cdot\mathrm{DT_x}}$	$\mathrm{LOD_x} = \frac{3.29\cdot\sqrt{\mu_{counts,BG,x}}+2.71}{\mathrm{S_x}\cdot\mathrm{DT_x}}$

$\sigma_{BG,x}$	BG standard deviation of analyte x
S_x	Average Sample Sensitivity of analyte x
n	# of data points of BG
m	# of data points of SG
$\mu_{counts,BG,x}$	Mean cps_{BG}*DT_x (after Poisson: $\sigma^2=\mu$)

Figure 25: The 4 cases of limits of detection estimation. The user decides whether the ND or PD formulas are used for the calculations.

4.4 Surface plots

As mentioned above, STALQUANT was not designed to generate plots other than what is necessary for selection of ablation intervals prior to the calculations. However, since it was developed to do imaging analyses, there is the option to create a map output file in which the line scan results are sorted by the elements. Surface plots can be created rapidly from the STALQUANT output file using a macro (appendix C) written in the image processing program *FIJI* [150], a distribution of *ImageJ* [151]. Adapting the macro to

the current sample (such as number of elements, number of line scans, etc.) is straightforward and quickly accomplished. It is particularly relevant to choose correct dimensions of the pixels in order to reproduce the sample features properly, as this macro does not apply any kind of data smoothing nor does it plot gradients from mathematical interpolation between two data points. Such interpolation may create artifacts in the surface plots that do not represent the measured element distribution in the sample [152]. Furthermore, it simulates more details than is feasible to achieve with the method. On the other hand, Paul et al. [153] suggested an algorithm to account for the fact, that generally multiple mass spectrometer data values for the same pixel are obtained, as laser spots usually overlap.

4.5 Summary

Use of STALQUANT (currently version 4) for quantification of LA-ICP-MS raw data extensively improves the handling of large amounts of data. It reduces operator time spent on calculating and recalculating large datasets from more recent LA applications (such as line scanning and imaging of large samples) through automation, which was not noteworthy when LA-ICP-MS was used for bulk analyses only. Concurrently the automation reduces operator errors which may occur frequently (copy/pasting data between worksheets) and are hard to uncover in manually calculated results. Recalculation of the raw data from a saved project is straightforward, employing any updated reference values etc. On the other hand, all constant values are saved with the results, allowing consulting them in the results file at any time for proper quality management. Using a macro (written in *FIJI*) rapidly generates element distribution images from the STALQUANT map results file.

5 Trace element concentrations in fluid inclusion of the gigantic gypsum crystals from the Naica cave in Mexico

Parts of the content of this chapter were published in P. S. Garofalo, M. B. Fricker, D. Günther, P. Forti, A.-M. Mercuri, M. Loreti, B. Capaccioni, Earth and Planetary Science Letters ***2010**, 289, 560–569.*[154]*, and in M. B. Fricker, P. S. Garofalo, D. Günther,* CHIMIA International Journal for Chemistry ***2011**, 65, 620* [155].

5.1 Introduction

The largest natural crystals ever discovered on Earth (up to 11 m in length) were found in the Chihuahua desert, of Mexico in 2002. These are gypsum crystals of the selenite[1] variety (Figure 26), which were found within a group of deep karst caves (so-called hypogenic caves) within the Ag-Pb-Zn underground mine of Naica. These caves were unveiled by miners of the *Peñoles* [156] mine company during their regular underground activity. Soon after discovery, the Italian non-profit organization *La Venta* [157] started documenting this natural wonder with its partners *Speleoresearch & films* [158] and *C/Producciones* [159], developing the *Proyecto Naica* [158] in 2006. Their role in this project has been to explore this exceptional karst environment, and make an appropriate multi-media documentation of the caves.

[1] Selenite is the transparent variety of gypsum ($CaSO_4 \cdot 2H_2O$). Its name derives from the greek word *Selene*, i.e. the lunar deity of the Greek mythology, and refers to the color of the moonlight (not the chemical element Selenium: the mineral Selenite is free of Se).

Figure 26: Impressions of the Cristales cave in Naica showing the mere size of the selenite crystals (up to 11 m) as compared to the size of the explorers, wearing a protective suit against heat and humidity (photographs courtesy of La Venta, Italy).

Until recently the Naica caves have not been accessible to the public for a number of reasons. First, they occur in a deep portion of the mine, where mining activities are not compatible with touristic attention. Second, the caves have been under water (i.e. below ground water level (Figure 28) for a very long time and were made accessible only due to constant water eduction from the mine activity. Third, although the present ground water level is well below the caves, the environmental conditions do not favour speleological activity. Today, cave temperatures exceed 45°C and relative humidity is above 90 % [160]. These are conditions under which regular speleological activity cannot last for more than 15-20 min (before further residence poses a serious threat to the life of the explorer), and make these caves a sort of 'modern frontier' of deep cave exploration. In order to make speleological mapping and sampling safe at Naica, *La Venta* developed an appropriate protective suit (Figure 26) and set up ad-hoc underground logistics and teamwork organization [160].

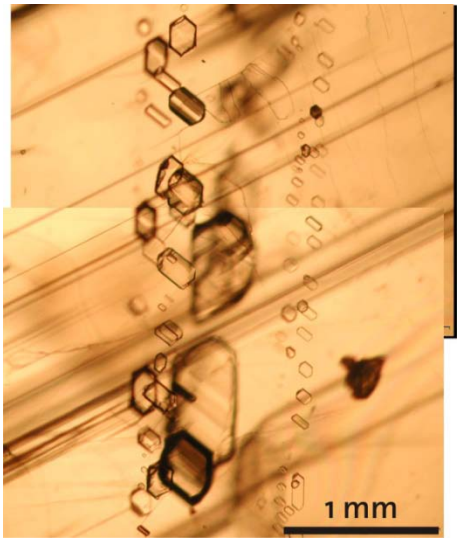

Figure 27: Photomicrographic image from an optical microscope displaying several Fluid Inclusion Assemblages (FIAs) within gypsum crystals.

The aim of the work was to determine bulk composition of the cave fluid entrapped within fluid inclusions (FIs) of the selenite crystals, a contribution to the Naica project. By definition, FIs are droplets of geological fluids found within tiny compartments in crystals (Figure 27). These inclusions are filled with liquids, gases, and sometimes also with solids and represent samples of the natural fluids from which minerals and rocks crystallized. In other words, FIs are micro-samples of fluids that were once in contact with the minerals and rocks at the time of their formation, and as such they convey fundamental information on the physical and chemical conditions under which minerals and rocks formed [161]. FIs can form in two ways [162]: a) at the time of crystal growth (primary FIs), in which case they represent the pristine fluid present during formation of the host mineral or b) after crystal growth, during the formation of fractures that cross-cut the host mineral (secondary FI) [163]. In the studied Naica samples, primary FIs are by far the most common inclusion type. Hence, groups of these primary FIs (Fluid Inclusion Assemblages, FIA) represent a statistically meaningful group of cave fluid samples, and have exactly the same age as the crystals. Because gypsum samples were collected in three distinct caves forming the Naica cave system (i.e. at *Cueva de los Cristales*, *Ojo de la Reina*, and *Cueva de las Espadas*, Figure 28), the studied groups of FIs allow the determination of gypsum precipitation in the entire cave system.

The types of FI analyses that are relevant to the characterization of natural (i.e. geological) fluids are both non-destructive and destructive. An important example of non-destructive FI analysis is microthermometry, which uses heating-freezing stages attached to a petrographic microscope to define the phase transitions occurring in the entrapped inclusion fluids [161,162]. Microthermometry allows the definition of some colligative properties of the trapped fluids (e.g. freezing point depression, vapour-liquid transitions, eutectic temperatures, etc.) that are of fundamental importance to reconstruct the P-T-X conditions of the trapped fluid. Raman spectroscopy [164] allows to de-

termine molecular species in fluids. Examples of destructive FI analyses are represented by bulk Gas Chromatography (e.g. [165]), Laser Induced Breakdown Spectroscopy (LIBS) [166], and LA-ICP-MS [167,168]. Recently an ablation cell with electronic cooling elements for LA-ICP-MS has been introduced [169]. It is mentioned here that LA-ICP-MS is also used for analysis of melt inclusions (inclusions which are solid at ambient pressure and temperature), e.g. it was compared to two other methods (electron microprobe, EMP and secondary ion mass spectrometry, SIMS) [170]. The dependence of the depth of the analyzed FI on element ratios has been studied by Guillong and Pettke [171], which is one of the two major difficulties of FI LA-ICP-MS. The other issue are limits of detection, which are not as good as LA-ICP-MS analysis of bulk solid samples due to low intensity of FI signals from the minute amount of sample stored in a single small FI.

In this study, LA-ICP-MS analyses were carried out on FIAs from the distinct cave samples listed above, i.e. from crystals in *Cueva de las Espadas* (CLE, located at -130 m below mine entrance), *Cueva de los Cristales* and *Ojo de la Reina* (CLC and OR, respectively, located at -290 m below mine entrance) depicted in (Figure 28). Additional analyses were carried out on gypsum samples, presently crystallizing from seeping of a contemporary fluid having ca. 53 °C, from a deep mine gallery forming a recent gypsum rosette (GR, see location called *thermal springs* in Figure 28 at -530 m below mine entrance). The comparison between the distinct FI compositions allowed deciphering the processes responsible for forming of such gigantic crystals.

5.2 Experimental and methods

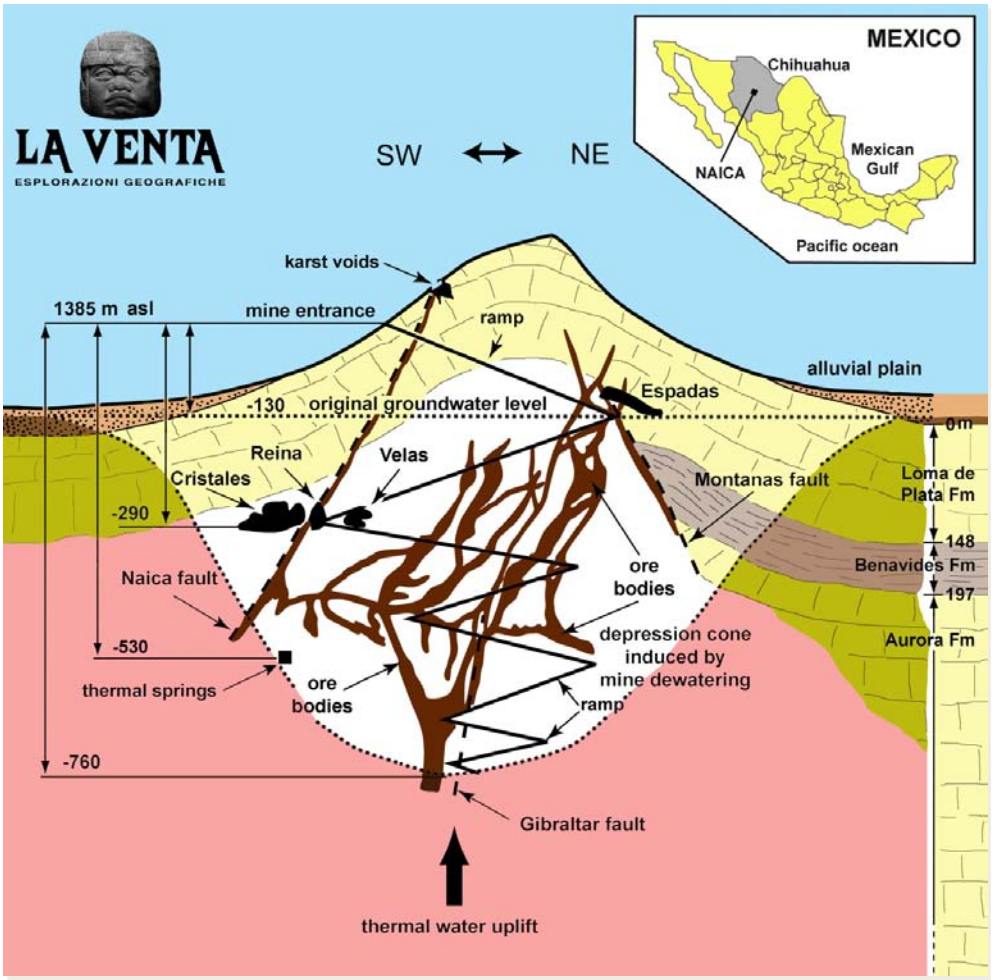

Figure 28: A cross-section of the mine and associated caves, the location of Naica, Mexico is indicated in the inset (top). Most of the ore bodies are below the original ground water level. However, they are made accessible due to constant pumping of the water. Illustration from [172].

From the four samples of the gypsum formation within the three caves, 11 FIAs were identified. In total 71 FIs were successfully analyzed by LA-ICP-MS using two UV 193 nm excimer lasers (GeoLasQ and GeoLasC, Lambda Physik, Göttingen, Germany) coupled to a quadrupole ICP-MS (ELAN6100DRC^{plus}, Perkin Elmer, Waltham, Massachusetts). Instrument conditions of the laser and the ICP-MS are listed in Table 4. Samples and external standard were mounted into an in-house cylindrical ablation cell [109](chapter 2.2, for gas flow modeling) with a volume of 50 cm^3 and LA was performed in single hole drilling mode. The MS was tuned daily for high sensitivity and low oxide formation.

Table 4: Instrumental settings of the laser system and the mass spectrometer.

LA Lambda Physik, GeoLasQ and GeoLasC		ICPMS Perkin Elmer, ELAN 6100 DRC^{plus}	
ArF excimer	193 nm	**rf power**	1380 W
fluence	9, 15 J/cm^2	**aerosol gas, He**	1.0 L/min
Repetition rate	10 Hz	**carrier gas**	0.8 L/min
Crater size	20, 30, 40, 60 µm	**aux. gas**	0.75 L/min
		plasma gas	17.5 L/min
		ThO^+/Th^+	<0.5%
		sweep time	0.637 s
Monitored isotopes:			
^{7}Li, ^{11}B, ^{23}Na, ^{24}Mg, ^{25}Mg, ^{26}Mg, ^{27}Al, ^{28}Si, ^{29}Si, ^{33}S, ^{34}S, ^{35}Cl, ^{37}Cl, ^{39}K, ^{42}Ca, ^{43}Ca, ^{47}Ti, ^{49}Ti, ^{51}V, ^{53}Cr, ^{55}Mn, ^{56}Fe, ^{57}Fe, ^{63}Cu, ^{65}Cu, ^{66}Zn, ^{68}Zn, ^{85}Rb, ^{87}Sr, ^{88}Sr, ^{89}Y, ^{90}Zr, ^{91}Zr, ^{93}Nb, ^{117}Sn, ^{118}Sn, ^{121}Sb, ^{123}Sb, ^{133}Cs, ^{137}Ba, ^{140}Ce, ^{175}Lu, ^{205}Tl, ^{206}Pb, ^{207}Pb, ^{208}Pb, ^{209}Bi, ^{232}Th, ^{238}U			

The measurement protocol reported by Longerich et al. 1996 [66] with external standard pairs analyzed at the beginning and at the end of a series was followed, using the SRM NIST 610 as external standard. During laser ablation of a FI, the laser first pulses drill through the host mineral (matrix), before the fluid inclusion is breached, then the laser continues to ablate deeper into the host material. In order to illustrate a typical FI ablation, a transient signal from one of the inclusions is shown in Figure 29.

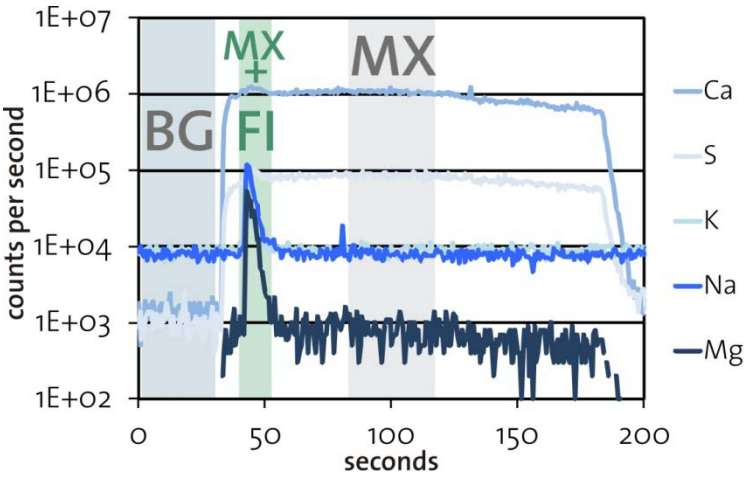

Figure 29: The breaching of a FI at just before 50 s is illustrated by the transient signal of a typical analysis. Shaded are the three phases of the signal: background (BG), fluid inclusion (FI) plus matrix (MX) and matrix alone which are necessary for successful quantification of the fluid composition [173]. Not the entire subsequent recording of the matrix signal is needed for the matrix correction. However, it demonstrates the stability of the signal from ablation of the gypsum.

Equation 2

$$I_{AN}^{FI} = I_{AN}^{total} - \frac{I_{Ca}^{total} \cdot I_{AN}^{MX}}{I_{Ca}^{MX}}$$

I_{AN}^{FI}	Signal contribution of the analyte AN in the FI only
I_{AN}^{total}	Sum of the analyte AN signal of both FI and MX (BG-subtracted)
I_{Ca}^{total}	Sum of the Ca signal of both FI and MX (BG-subtracted)
I_{AN}^{MX}	Signal of the analyte AN in MX (BG-subtracted)
I_{Ca}^{MX}	Signal of Ca in MX (BG-subtracted)

At the time, when the FI is breached, the transient signal comprises the FI contents plus variable contributions from the matrix (MX). Hence, before trace element concentration in the FI can be calculated, the contribution from the MX is subtracted using matrix correction Equation 2, reported by Heinrich et al. 2003 [174]. This matrix correction is valid under the assumption that the matrix element is not present in the solution of the FI. If this is not the case, the deconvolution of individual signal contributions is required [175]. For our gypsum samples, Ca was the only matrix element that could be used for matrix correction, as material purity was determined to be very high. Knowing only the FI fraction of the signal, quantification is possible using Equation 3 [66], provided that the concentration of an internal standard is known. An internal standard often used in FI analysis is Na, i.e. the most abundant cation of geological fluids [162]. The concentration of this metal can be estimated independently using the freezing point depression of the inclusion fluid determined via microthermometry prior to LA. Thus, before LA analysis, about 400 microthermometric measurements were performed to obtain the bulk salinity of the FIs using a Linkham THMSG 600 heating/freezing stage attached to an Olympus BX51 petrographic microscope. These salinity values are reported as mass % NaCl equivalents (more details in [154]). As these salinity values comprise contributions from all salts present in the FI, they are corrected for the presence of other analytes using the so-called salt correction [174] in order to calculate absolute element concentrations, Equation 4.

Equation 3

$$C_{AN}^{FI} = C_{Na}^{FI} \cdot \frac{I_{AN}^{FI}}{I_{Na}^{FI}} \cdot \left(\frac{I_{Na}^{NIST}}{I_{AN}^{NIST}} \cdot \frac{C_{AN}^{NIST}}{C_{Na}^{NIST}} \right)$$

C_{AN}^{FI}	Final result, concentration of analyte AN in the FI
C_{Na}^{FI}	Concentration of internal standard in the FI (obtained from independent measurements)
I_{AN}^{FI}	Signal of analyte AN in sample (BG-subtracted)
I_{Na}^{FI}	Signal of internal standard Na in the FI (BG-subtracted)
I_{Na}^{NIST}	Signal of internal standard Na in external standard (BG-subtracted)
I_{AN}^{NIST}	Signal of analyte AN in external standard (BG-subtracted)
C_{AN}^{NIST}	Concentration of analyte AN in external standard (certificate of ES)
C_{Na}^{NIST}	Concentration of internal standard Na in external standard (certificate of ES)

The terms in parentheses refer to values (signal intensities *I* and certified concentrations *C*) of the external standard SRM NIST 610, all intensities *I* are obtained from the measurements and the concentration of the internal standard was obtained prior to LA from microthermometric measurements.

Equation 4

$$NaCl_{eq}\,wt\% = C_{NaCl} + 0.5 \cdot \left[C_{MgCl_2} + C_{KCl} \right]$$

$NaCl_{eq}$	Corrected concentration of $NaCl_{eq}$ (i.e. concentration of NaCl only in FI)
C_{NaCl}	Concentration of $NaCl_{eq}$ determined by microthermometry
C_{MgCl_2}	Concentration of $MgCl_2$ in FI
C_{KCl}	Concentration of KCl in FI

The salt correction can be done only after knowing the main salt components present in the FI. The corrected concentration is then inserted in Equation 3.

5.3 Samples

Photographs of the five samples analyzed in this study are shown in Figure 30, which reports also some relevant details of the analyzed FIAs. The samples we have studied are:

1) A 11 cm-long, (swallowtail) twinned gypsum growing on the walls of *Cueva de las Espadas* (Figure 30A).
2) Fragment of a m-long, perfectly transparent selenite crystal from the floor of *Ojo de la Reina* (Figure 30B).
3) Fragment of a m-long, perfectly transparent selenite crystal from the floor of *Cueva de los Cristales* (Figure 30D).
4) Block of a euhedral, m-long crystal growing on the floor of *Cueva de las Espadas* (Figure 30E).
5) Aggregate of cm-long, euhedral crystals of gypsum growing at the roof of a mine gallery where thermal springs seep out. At the time of sampling, the crystals were covered by a thin film of aragonite ($CaCO_3$ (Figure 30C)).

Fluid inclusions at the core of crystals, 3 and 4 listed above, are large and regularly shaped (Figure 30F, H), while those at the rim of crystal 4 are flat, irregularly elongated, and host solid inclusions (Figure 30G). For the core of crystal 3 (Figure 30D), a corrected U/Th age of 34.5±0.8 ka has been determined [176].

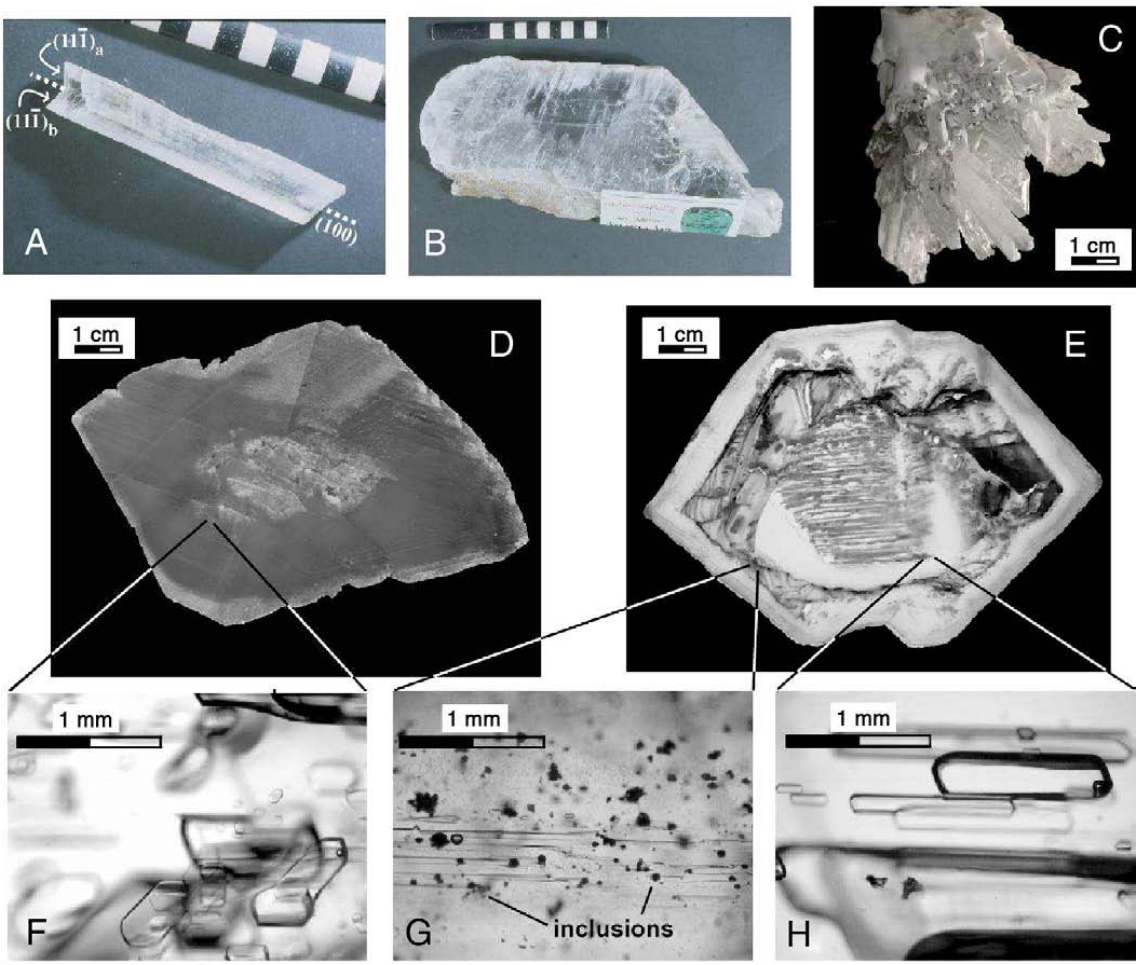

Figure 30: Photographs of the samples used in this study (A-E) and microscopic images of fluid inclusions (F-H). From the walls in *Cueva de los Espadas* (A), from the floor of *Ojo de la Reina* (B), from a gypsum rosette at Thermal Springs (C), from a fragment of a m-long crystal on the floor of *Cueva de los Cristales* (D), and from a m-long crystal growing on the floor of *Cueva de los Espadas* (E). Note the regular shaped FIs in the cores of both D and E, on the other hand the elongated FIs and solid inclusions in the rim of E. Illustration from [154].

5.4 Results and discussion

The calculated salinities from the microthermometric determinations are plotted in Figure 31A-C. The results reveal that bulk salinity of the cave fluid decreases systematically as a function of depth within the cave system. In the shallowest cave CLE, the highest salinity of 7.7 wt % $NaCl_{eq}$ was determined at the rim of the sample, while a value of 5.3 wt % $NaCl_{eq}$ was obtained at the core. In contrast, the samples from the deep caves CLC and OR (located at the same mine level) have a lower salinity of 3.1-4.2 wt % $NaCl_{eq}$. For the deepest sample, the gypsum rosette, a salinity of 0.7-1.6 wt % $NaCl_{eq}$ was obtained. A systematic decrease of concentration as a function of depth is shown by the fluid components Na, Mg, K, Sr, and Pb in the inclusion fluid from the

deep caves (Figure 31D, E). This feature represents a fundamental chemical signature of the regional underground flow system of Naica, and provides a unique geochemical marker of the local process that controlled crystal growth.

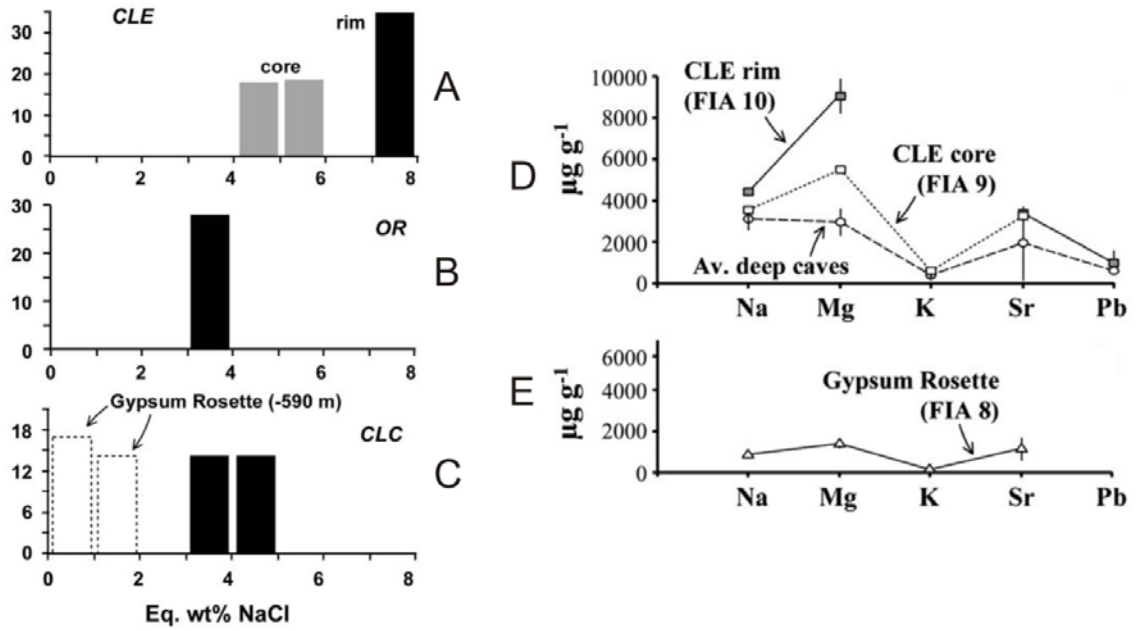

Figure 31: Histograms of the bulk salinities (A-C) of the samples illustrate the systematic decrease of bulk salinity with the depth in the cave system (CLE>CLC OR>GR). Concentrations of the most abundant elements (D, E) display the same trend of lower concentrations for samples from deeper caves. Illustration from [154].

The evidence for 9000 µg/g Mg and a Na/K ratio >>1 in the cave fluid (Figure 31D and Table 5), and the similarity between these values and those typically found in ground waters from arid environments subjected to evaporation [177], led Garofalo et al. [154] to consider the hypothesis that the climatic change occurring in the north of Mexico during crystal growth controlled the chemical composition of the cave fluid, and therefore crystal growth. An independent pollen record from lake sediments collected a few km north of Naica, lake Babicora [178], actually confirm this hypothesis, as it shows that in the Naica region cycles of warm/dry and fresh/wet climatic periods characterized the time between about 60 and 15 ka ago, with a later shift towards a definitely warmer period after that time. One of the crystals of CLE has been dated to have grown between 57 and 15 ka ago [179], hence its growth must have occurred during those cycles.

Table 5: Trace element concentrations in each FIA, number of FIs in a FIA given in second column, values from [154].

Sample	#FIs	**Na** µg/g	**Mg** µg/g	**K** µg/g	**Sr** µg/g	**Pb** µg/g
CLE	9	7500±800	1200±1300	1600±800	1800±1600	<LOD
CLE core	9	3600±1000	5500±1400	590±150	3000±3000	<LOD
CLE rim	14	4453 (n=2)	9100±800	<LOD	3000±5000	1000±600
OR	5	2200±200	3900±300	278 (n=1)	n.d.	553 (n=1)
OR	10	3100±600	2600±900	500±400	1700±2900	<LOD
OR	7	3500±500	2100±600	330±30	2300±1700	<LOD
CLC	7	3500±900	3000±800	320 (n=1)	1700±800	<LOD
Gypsum Ros.	9	820±90	1400±300	120±30	1100±600	<LOD

The discovery of an assemblage of 65 pollen grains within the crystal having 35 ka of age (Figure 30D) and studied for the characterization of the cave fluid [154], provide an independent evidence for crystal growth being controlled by climatic changes. Pollen species like *Quercus garryana*, *Juniperus*, *Taxus*, *Lithocarpus*, and others now hosted by the cave gypsum, must have been waterborne in the first place, transported to CLC by the regional underground flow system and entrapped within the crystal together with the FIs about 35 ka ago. That vegetational and floristic assemblage is characteristic of a mixed broadleaf wet forest, similar to the one currently present today in the south-western regions of the United States but not at Naica. Hence, relatively wet and cold climatic conditions must have been present at Naica during the crystallization of that the sample, in surprising agreement with the results provided from the data of Lake Babicora 35 ka ago [178].

Summarizing, our study shows that a climatic record is present within the gypsum crystals of Naica, therefore, other similar hypogenic cave systems worldwide may contain the similar records. Conclusions about this record emerged from studies of the composition of the cave fluid enclosed within the gypsum fluid inclusions and by the coeval pollen assemblage. The combination of these independent data sets may represent a useful tool for paleo-climatic studies of continental areas in the future.

From the experimental point of view, the results using our standard cylindrical ablation cell are satisfactory considering the unusual large FIs present in these samples. For the analysis of smaller FIs it would be necessary to increase the maximum intensity of the FI signal. This can be achieved by using an ablation cell with faster washout, i.e. smaller cell volume or optimized aerosol transport geometry. But a small cell volume severely limits the number of samples and external standards that can be placed inside of the cell simultaneously and is therefore dismissed. An ablation cell with optimized geometry for fast washout of the aerosol and room for many samples is a potential solution to this task. Such cell geometry is developed, tested and discussed in chapter 2.5, although the aim of the following study was not directly related to improving FI analysis, but rather analysis of heterogeneous samples with high spatial resolution, particularly ability to mount large or many samples simultaneously.

6 Element distribution profile in a lake sediment

The work presented in this chapter resulted from collaboration with Beat Aeschlimann, (Laboratory of Inorganic Chemistry, ETH Zurich, 8093 Zurich), who performed μ –XRF measurements.

6.1 Introduction

For the analysis of sediments X-Ray Fluorescence (XRF) spectrometry scanners have been and are commonly used [180,181] to determine major and minor elements. Gholap et al. [182] reported a comparison between LA and XRF for elemental imaging of biological tissue. They have concluded that both techniques are complementary in providing elemental images of tissue samples, although they provide qualitative results only. However, obtaining quantitative results with XRF is not straightforward due to matrix effects and the complex absorption of X-rays [183]. Furthermore, the detection limits are not low enough for trace element determinations (10-50 μg g^{-1} specification for Eagle III μ-XRF Spectrometer [184]). Using LA-ICP-MS allows quantitative analysis of major, minor and trace elements, moreover both methods work at μmeter resolution (spot size). This chapter aims at comparing LA analysis with its versatile potential to the well-established XRF analysis for such samples and evaluating the potential of LA-ICP-MS for such samples and studies. Reproducibility of each of the two methods was tested and element distribution profiles were superimposed to evaluate the cor-

relation between the two techniques. Finally interpretation of some of the element profiles obtained was attempted.

A prototype ablation cell with sled design for manual sample movement was used to perform a line scan on a lake sediment. The sample dimensions were 176x19x8 mm (Figure 32), hence too large to fit into the standard ablation cell (radius 25 mm) without further cutting. The sediment sample was collected from lake Zurich, Switzerland (~-130 m, greatest depth between Horgen and Meilen, surface 406 m asl) in 2004, prepared and provided by Prof. H. Thierstein (Geological Institute, ETH Zurich).

Figure 32: Photograph of the sediment ZHMP04 from lake Zurich. Chronology according to 2004 on the left and on the right 1944.

6.2 Experimental and methods

For stability and conservation reasons the sediment ZHMP04 was embedded in epoxy (Araldite BY 158, hardener HY 2996) and mounted together with SRM NIST 610 into the prototype ablation cell. The analyses were carried out using an ArF excimer laser at 193 nm (GeoLasC, Lambda Physik, Göttingen, Germany) coupled to a quadrupole ICP-MS (Agilent 7500cs, Palo Alto, USA) and by an EDXRF Eagle II (Röntgenanalytik Messtechnik GmbH, Taunusstein, Germany). Operating conditions are listed in Table 4. A total of 8 line scans (2400 µm length) were combined and resulted in one complete profile. Three complete profiles within the same track were obtained using LA (black line in Figure 32) and one complete profile was measured using µ–XRF (below the black line Figure 32). An external calibration [66] using SRM NIST 610 (two measurements before and two after the 8 line scans on the sediment) and an internal standard procedure using $^{42}Ca^{+}$ were applied for quantification of the signal intensities. The raw data were calculated using LAMTRACE [148] and the concentrations were normalized to 100 wt % sum of the oxides [68,149]. This resulted in 3 complete profiles. The limits of detection (listed in Table 7) were calculated for each line scan using the equation in Figure 25 (chapter 4.3) and all values <LOD are not shown in the data graphs.

All µXRF data are shown as net intensities (i.e. background subtracted) since matrix matched calibration materials for such sediments are not available. The µXRF element mapping was performed on a 4.8 x 3.75 mm area (yielding 512 x 400 pixel) on the sediment. The age model used in our study was provided by Prof. H. Thierstein.

Table 6: Instrumental settings of the laser system and the mass spectrometer.

LA GeoLasC		ICPMS Agilent 7500cs		EDXRF Eagle II	
ArF excimer	193 nm	**RF power**	1500 W	**Tube**	Rh, 20 kV/ 1mA
scan length	2400 µm	**aerosol gas, He**	1.0 L/min	**beam diameter**	50 µm
fluence	15 J/cm²	**carrier gas**	0.4 L/min	**# spectra**	8310
crater size	94.5 µm	**plasma gas**	15.0 L/min	**dist. between points**	24 µm
rep. rate	10 Hz	**sweep time**	0.605 s	**time**	15 s/point
scan speed	50 µm/s	**dwell time**	10 ms	**modulation time**	6 s
Monitored isotopes:				**Monitored elements:**	
$^{7}Li^{+}$, $^{10}B^{+}$, $^{23}Na^{+}$, $^{25}Mg^{+}$, $^{27}Al^{+}$, $^{29}Si^{+}$, $^{39}K^{+}$, $^{42}Ca^{+}$, $^{49}Ti^{+}$, $^{53}Cr^{+}$, $^{55}Mn^{+}$, $^{57}Fe^{+}$, $^{59}Co^{+}$, $^{65}Cu^{+}$, $^{66}Zn^{+}$, $^{75}As^{+}$, $^{85}Rb^{+}$, $^{88}Sr^{+}$, $^{89}Y^{+}$, $^{90}Zr^{+}$, $^{93}Nb^{+}$, $^{109}Ag^{+}$, $^{111}Cd^{+}$, $^{118}Sn^{+}$, $^{121}Sb^{+}$, $^{133}Cs^{+}$, $^{137}Ba^{+}$, $^{139}La^{+}$, $^{140}Ce^{+}$, $^{141}Pr^{+}$, $^{146}Nd^{+}$, $^{147}Sm^{+}$, $^{153}Eu^{+}$, $^{157}Gd^{+}$, $^{159}Tb^{+}$, $^{163}Dy^{+}$, $^{165}Ho^{+}$, $^{166}Er^{+}$, $^{169}Tm^{+}$, $^{173}Yb^{+}$, $^{175}Lu^{+}$, $^{178}Hf^{+}$, $^{181}Ta^{+}$, $^{182}W^{+}$, $^{205}Tl^{+}$, $^{208}Pb^{+}$, $^{209}Bi^{+}$, $^{232}Th^{+}$, $^{238}U^{+}$, $^{248}ThO^{+}$				Al Kα, Si Kα, P Kα, S Kα, Cl Kα, Cd Lα, K Kα, Ca Kα, Ti Kα, Mn Kα, Fe Kα, Cu Kα, Zn Kα, Pb Lα, Sr Kα, Mo Kα	

Table 7: List of the limits of detection (LOD) of LA-ICP-MS expressed as 3xSD of BG/Sensitivity of sample.

Element	LOD [µg g^{-1}]	Element	LOD [µg g^{-1}]
Na	6	**As**	1
Mg	3	**Sr**	0.1
Al	2	**Cd**	1
Fe	15	**Ti**	3
Cu	1	**Cr**	1
Zn	1	**Mn**	1
Si	263	**Sn**	0.1
K	2	**Sb**	0.1
Ca	120	**Pb**	0.1

6.3 Results

The reproducibility of LA-ICP-MS for successive line scans within the same tracks was demonstrated by acquiring data for 3 runs (without a cleaning scan) and the results (shown in Figure 33) of the second and the third run show trends in good agreement (mathematical correlation is hampered by the noise of the signals, thus the correlation coefficient is not given). However, the first analysis of the surface of the sample is

slightly off which can be mainly explained by surface impurities or contaminations. Furthermore it is known that the ablation of a fresh surface leads to a larger particle size formation, which causes higher RSD of the transient signals an effect of incomplete vaporization in the plasma [7]. Particularly the differences in the elements such as Si demonstrate the necessity of a cleaning scan which removes surface impurities as well as loose material from the sample material. Moreover it proves higher reproducibility of consecutive line scans within the same track.

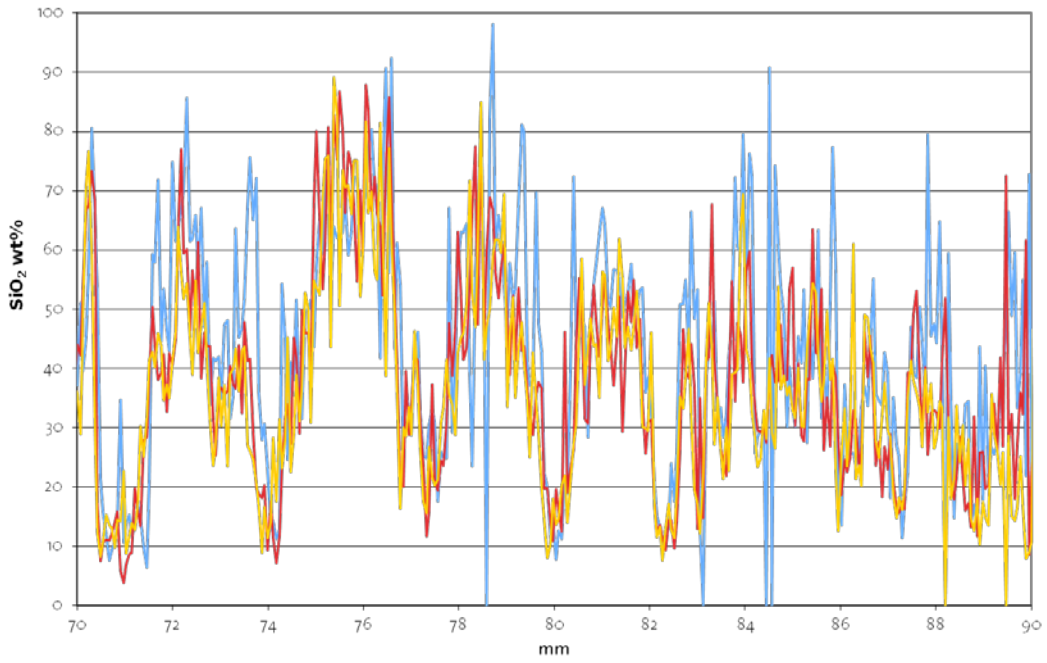

Figure 33: Section of the Si profile in the sediment for three consecutive analyses within the same track, no cleaning scan applied. The second (red) and third (orange) runs match closely, whereas the first (blue) is different.

The concentration profiles of Ca versus Si (Figure 34) demonstrate competitive sedimentation of detritus from silica forming (algae, diatoms) and $CaCO_3$ forming (invertebrates) organisms. The concentration profiles of Ca and Sr correlate due to the similar chemical properties of these two elements (both are alkaline earth metal, similar atomic radii, similar electro-negativity).

A selection of 21 elements above LOD (Mg, Al, Si, K, Ca, Ti, Cr, Mn, Fe, Cu, Zn, As, Sr, Zr, Cd, Sn, Sb, Ba, La, Tm, Pb) from the quantified LA results for second and third run are summarized in Figure 36, only the second and third run. The first run is discarded in the further discussion due to surface impuritiy, Figure 33. The trace elements (black and grey) are given in µg g^{-1} and major elements are given as wt% of their respective oxide.

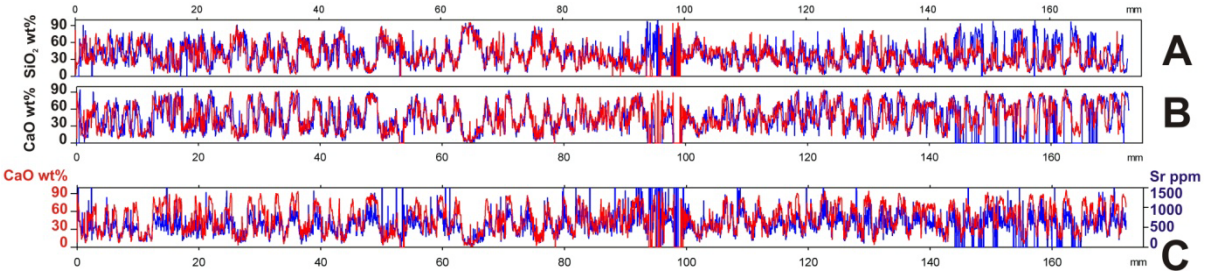

Figure 34: Concentrations of Si, Ca, Sr within laminated sediment determined by LA-ICP-MS at a spot size of 60 m and a repetition rate of 20 Hz. Anti-correlation of Ca and Si for two runs within the same track (a, b, red and blue), and correlation of Ca and Sr (c) were found.

A prominent feature is the bright, thick layer (in the photograph at 63 cm) corresponding to high Si and low Ca concentrations, a consequence of algal bloom (planktonic diatoms in freshwater) during the summer of 1982 (solid black frame), usually due to elevated temperatures [185,186] as well as nutrient availability. Average monthly air temperatures are plotted in Figure 35, which have been recorded at Fluntern (556 m asl), Zurich, Switzerland by MeteoSwiss [187]. However, these data show higher temperature (higher than 20°C) during summer of 1983, suggesting a possible counting error in the chronology of this sediment record, as counting is usually challenging. About the source of Si in the sediment, not the entire Si content in lake sediment is of biogenic origin. Up to 60 % biogenic Si were detected by Stoermer et al. [185] in Lake Baikal sediment, while the rest of Si content is usually attributed to detrital Si (rock fragments). Nevertheless, both LA-ICP-MS and XRF account for the bulk content of Si without specification of the Si origin. The results of the two methods (µXRF and LA) are correlated in Figure 37. Numerous spikes were observed in the trace element profiles of both runs. It was found that most of the discrepancies are caused by individual spikes within separate runs. Presence of spikes hampers the quality of statistical considerations, e.g. principle component analysis. Therefore, spike removal algorithms need to be carried out prior to statistical analysis of the determined concentrations.

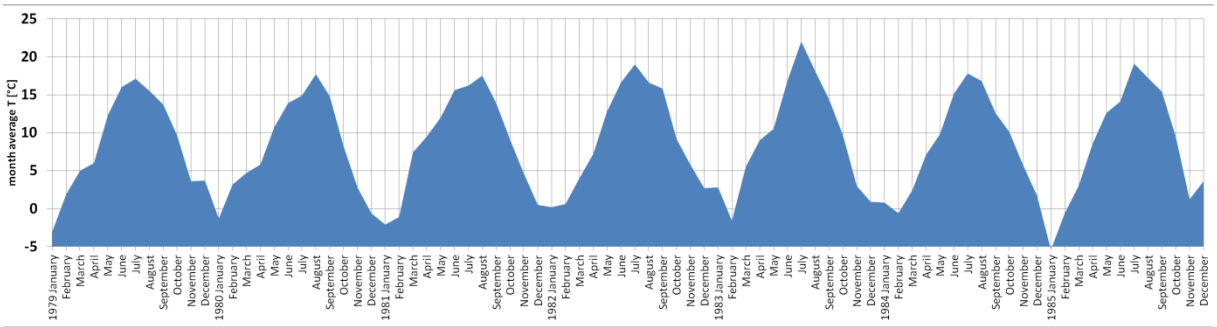

Figure 35: Air temperature (monthly average) at Fluntern (556 m asl), Zurich, Switzerland. Data from MeteoSwiss [187].

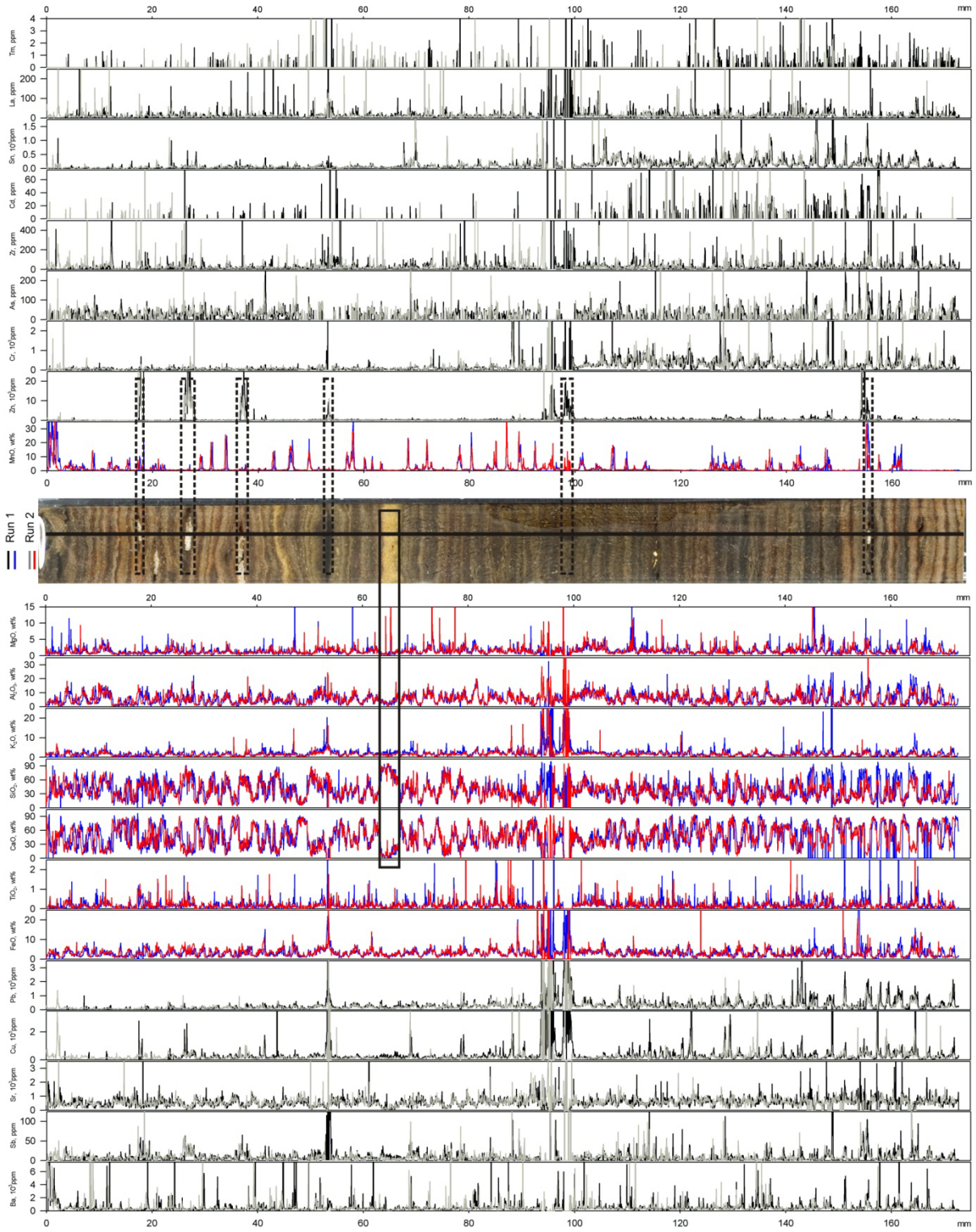

Figure 36: Concentration profiles of the sediment, obtained from LA-ICP-MS measurements. Holes in the epoxy resulted in artifacts in the Zn profile marked with dashed frames. First runs (black and blue) match second runs (grey and red) within the same track. One prominent event (black solid frame) is the hot summer of 1982, where temperatures caused algal bloom, represented as high Si concentration.

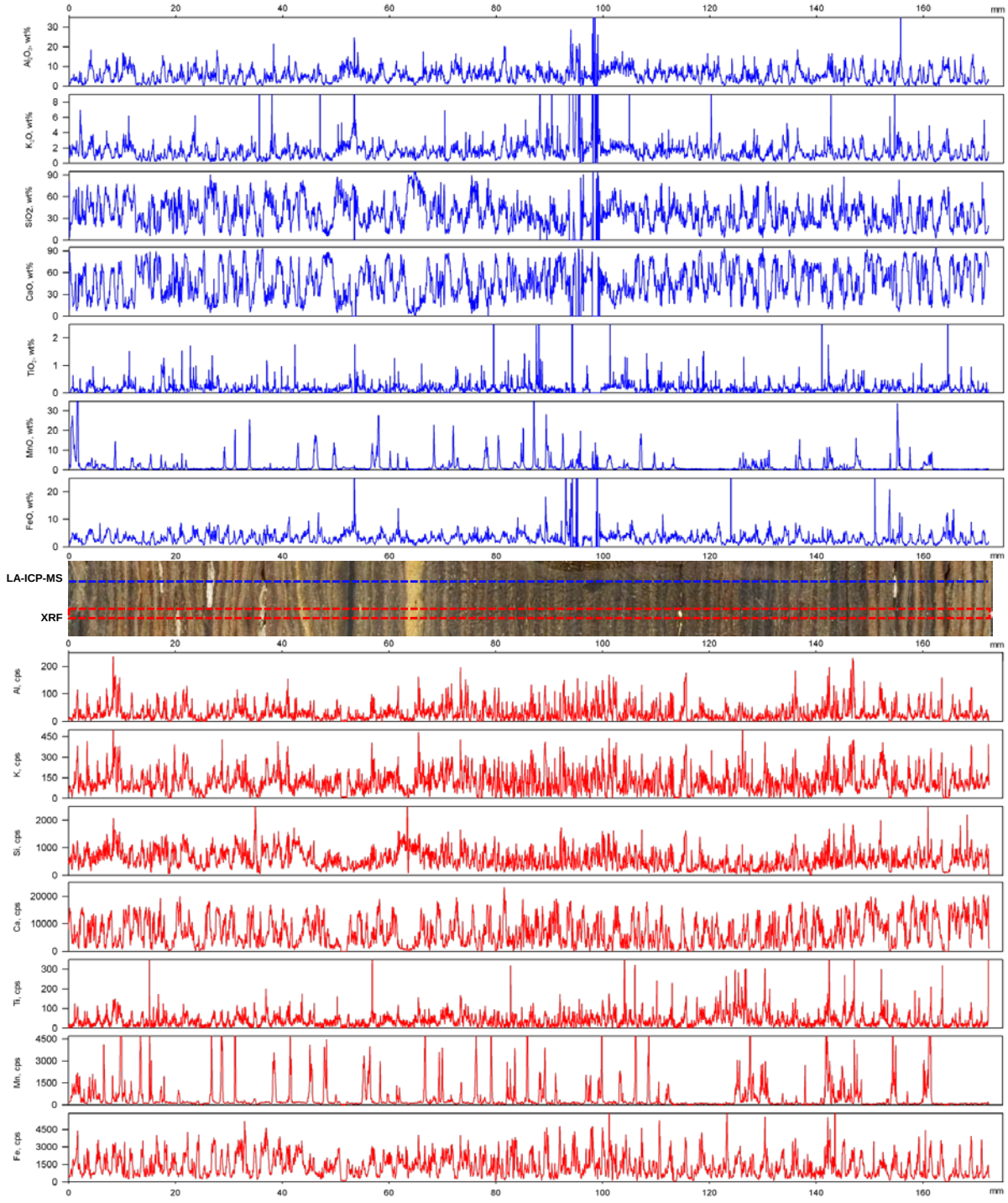

Figure 37: Concentration profiles from LA-ICP-MS are compared with intensity profiles (counts per second) fromμ – XRF analysis on parallel line scans.

The observed signals for Zn are artifacts from sample preparation (gaps and holes filled with white powder) and were marked with dashed frames. The same signals for Zn are observed in the XRF analyses (Figure 38), confirming that the signals are not caused by a polyatomic interference in the ICP-MS, but rather by a Zn containing impurity during the replacement of water with epoxy.

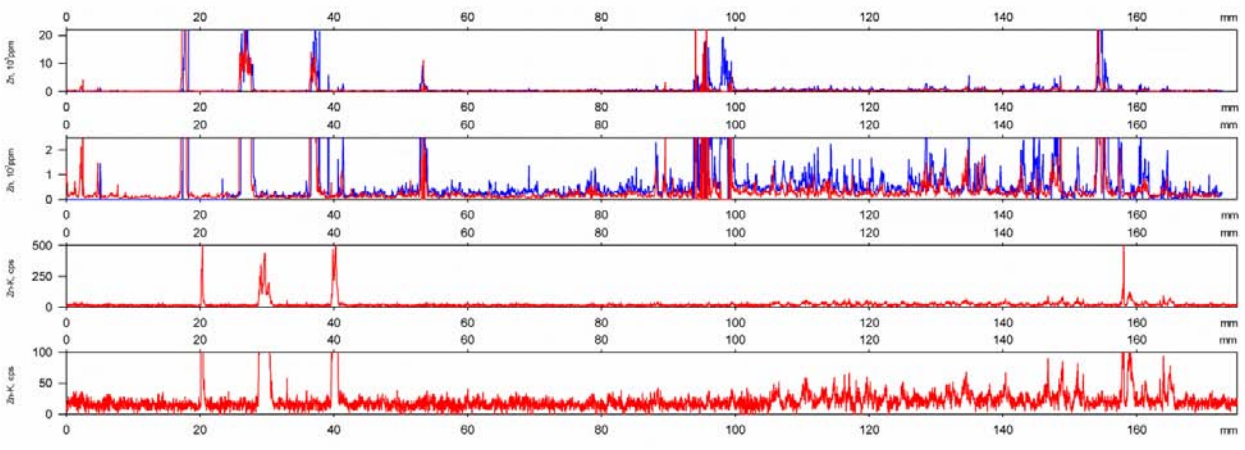

Figure 38: The concentration profiles of Zn acquired using LA-ICP-MS (upper two graphs) and XRF (lower two graphs). The scale of the lower plot of each pair is enlarged in order to make the small variations of Zn visible. The two acquisitions using XRF and LA-ICP-MS were carried out parallel but not exactly at the same position and still lead to similar results. Both techniques confirm the presence of Zn in the white powder filling the gaps and holes.

Reproducibility of two µXRF line scans is demonstrated in Figure 39 for Ca. The signals were acquired parallel with a distance of 5 mm between the lines. The data confirm overlap of most of the transient peaks. To show the mapping capabilities of µXRF , an area of 4.8 x 3.75 mm was analyzed (Figure 40). The element distribution was generated using a spot size of 50 µm. The figures show that a qualitative analysis can be carried out and these results confirm the results achieved by the two line scans. However, it needs to be stressed that these µXRF data are qualitative only. In contrast, LA-ICP-MS mapping can be carried out at similar spatial resolution and providing quantitative data for major, minor and trace elements (see chapter 8).

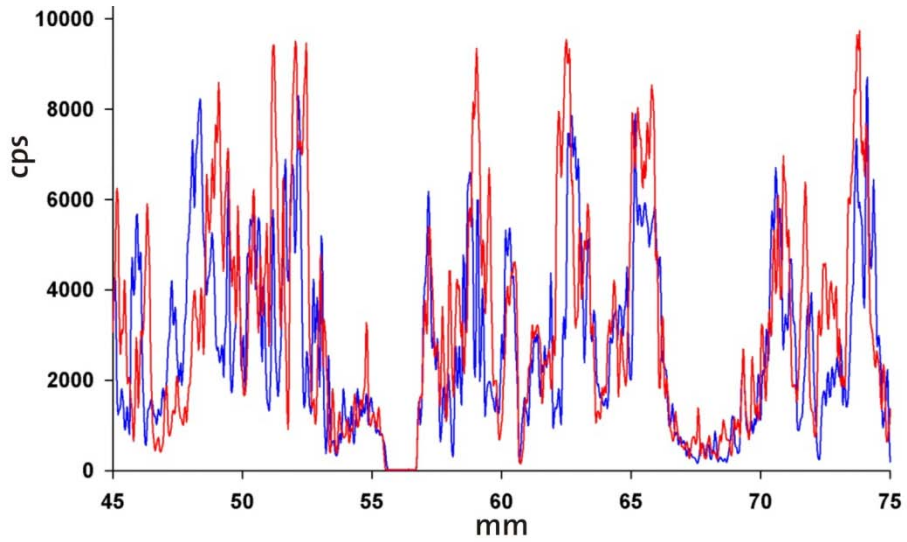

Figure 39: XRF intensities of Ca for two runs (blue, red) 5 mm apart on the sediment. The two signals overlap well considering they were not acquired in the same track.

A direct comparison of LA-ICP-MS and XRF element profiles is summarized in (Figure 41) for Mn and Ca. As it can be seen, both techniques provide very similar results. However, correlation coefficients cannot be given, since the XRF data are not quantitative. The narrow signals of high concentration of Mn correspond to a very narrow layer between the dark (winter) and bright (summer) layers of the sediment. This enrichment is an effect occurring either in spring or in fall over a short period in time. It is supposedly present in every year. However, it seems to be concentrated in hotspots spread across a layer (Figure 40). The spatial resolution used for these measurements allow to detect most of these Mn enriched layers. However, as shown some are missing due to the sample preparation and the heterogeneity of the layer structure of sediments.

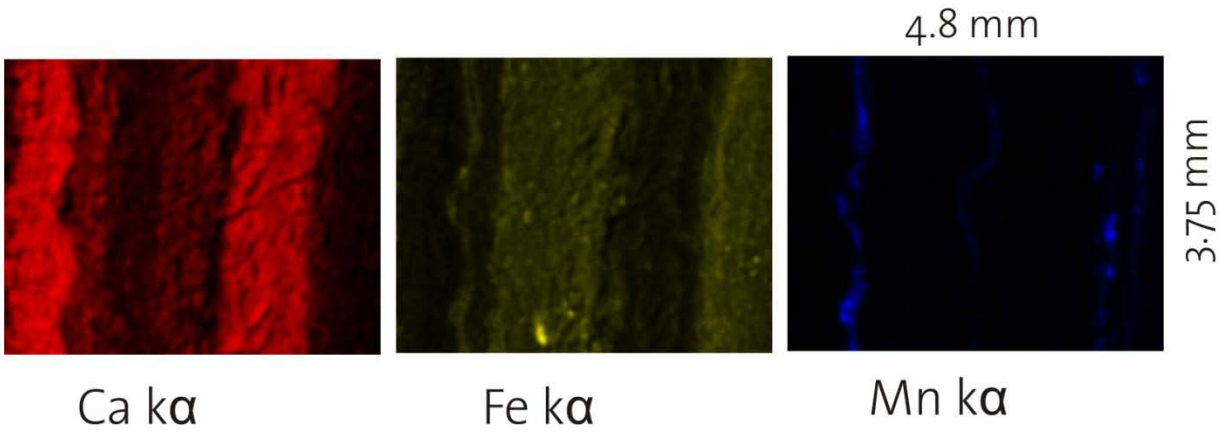

Figure 40: Mapping usingμXRF on a 4.8 x 3.75 mm area of the sediment. Several layers are observed and the element distribution correlates to the line scans.

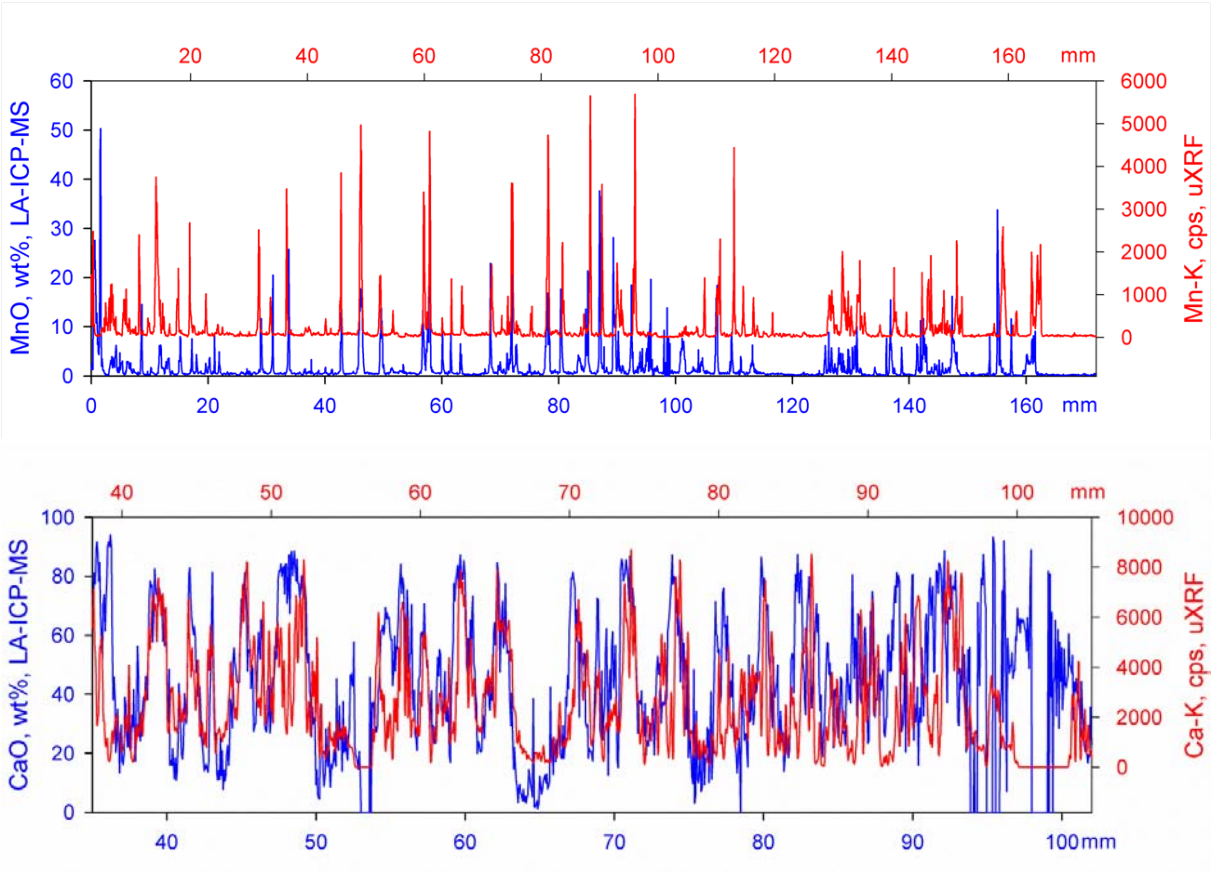

Figure 41: Comparison of quantitative LA and qualitative XRF results for the elements Mn and Ca evidences that the results of the two methods agree.

The age model of the sediment of interest is shown in Figure 42 and shows that the record dates back to 1944 (by layer counting) which can be seen in the yearly patterns in the Ca and Si concentration profiles. However, the growth rate of the sediment layers is not constant and depends on a number of environmental factors. Therefore, the age is not linear to the distance.

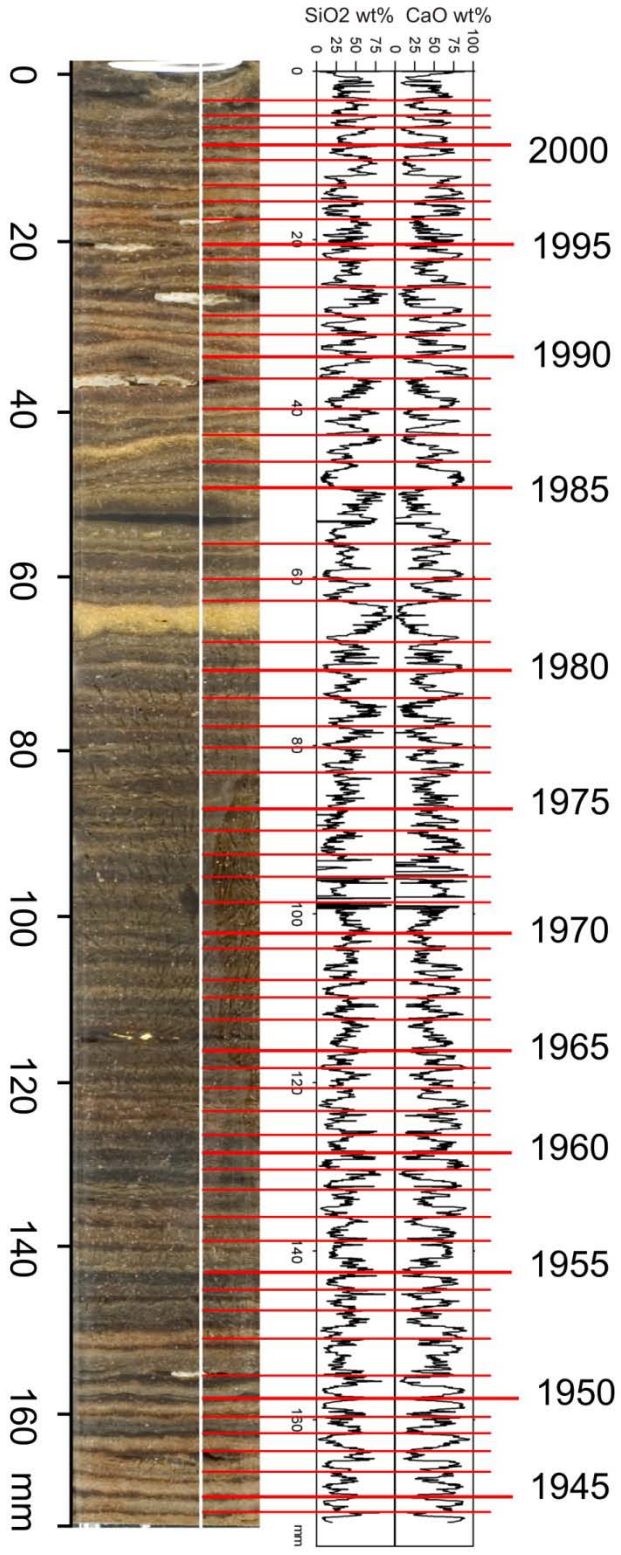

Figure 42: The Si and Ca concentrations plotted with a photograph of the sediment. Line scan of LA indicated by the white line and chronology provided by Prof. H. Thierstein.

The results measured by LA-ICP-MS revealed that many metal concentrations decreased in the more recent years, e.g. for Pb, Sn, Zn, Cr, Cd, Cu after around the 1970s,

Figure 43. A combination of many factors, most of them probably related to environmental consciousness, e.g. ban of Pb additives in petrol, regulations of toxic waste disposal, etc. The concentration profile of Sb, however, seems to be unchanged which may be related to its addition to friction brake pad composition used in motorized vehicles.

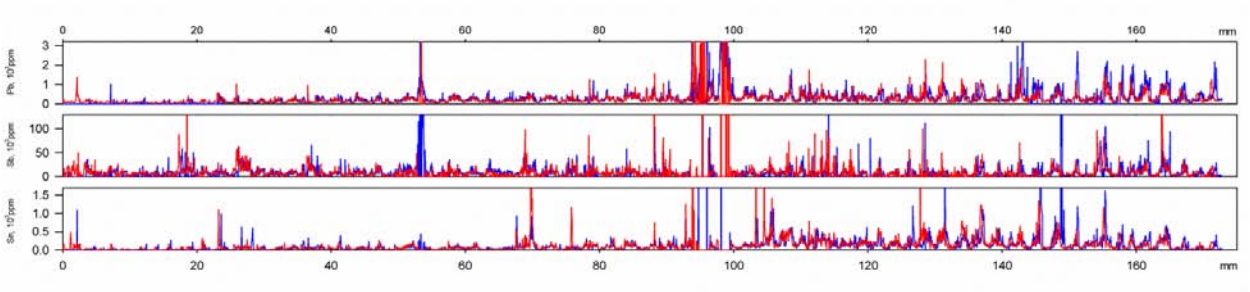

Figure 43: Profiles shown for Pb, Sb and Sn, it is observed that overall concentrations of these elements steadily decrease from 1944 to recent times.

Friedl [188] reported in 2001 that Ag concentrations can be used as a tracer for diatom production in marine sediments. Phytoplankton takes up Ag (similarly to Cd) which is deposited and immobilized as Ag_2S like CdS. A large population of these algae will lead to a higher concentration of Ag along with Si in the sediment. In the freshwater sediment sample of this study, such an incident from a large diatom population can be found in the wide yellow layer from the summer of 1982, although the Ag concentration for that area is below limits of detection. For other areas with higher Ag concentrations a correlation of Ag and Si was found (Figure 44). Unfortunately, the Cd concentrations determined in the sediments were mostly below limits of detection for the entire profile and is thus not shown.

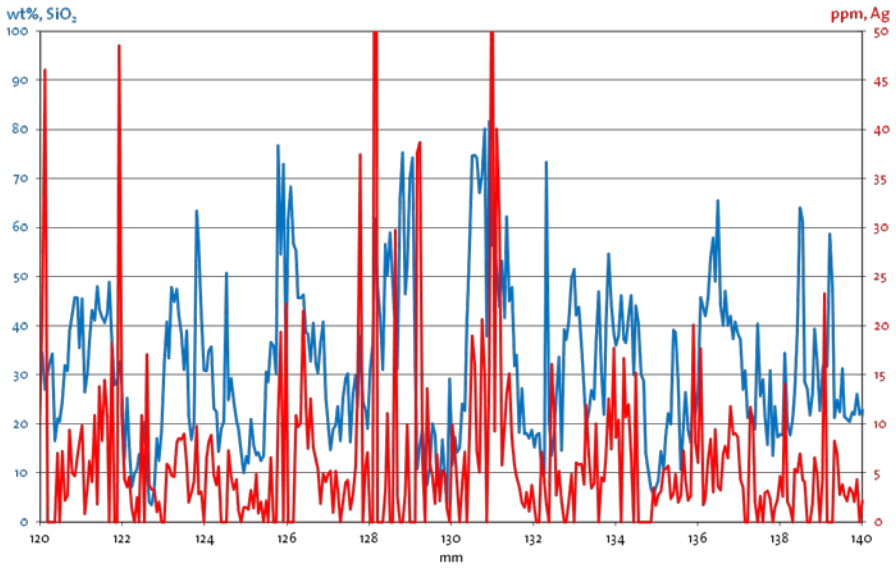

Figure 44: Close up of SiO2 wt% and Ag µg g-1 for the position between 120 and 140 mm of LA on the sediment sample. A similar pattern for the two elements was observed, although an Ag concentration is very low.

6.4 Summary

This study shows that µXRF and LA-ICP-MS analyses lead to comparable results when analyzing heterogeneous or layered samples. However, the detection capabilities of LA-ICP-MS are superior when compared to the so far well established µXRF technique and allow the determination of elements with a linear dynamic range of 9-10 orders of magnitude. In addition, LA-ICP-MS provides qualitative and quantitative data for major, minor and trace elements and could also be used to measure isotope ratios. The widespread use of µXRF is based on the fact that data can be acquired under normal atmosphere or in vacuum. In contrast, LA-ICP-MS requires a little more sample preparation and sample cutting. Some of these problems have been successfully addressed within this thesis and the newly designed ablation cell might contribute to the routine application of LA-ICP-MS to such environmental archives. The achievable spatial resolution is discussed in chapter 7.2.

In particular, interpretations of the element distributions based on their concentrations will provide new insights into environmental processes. In contrast to XRF, much more details become visible using LA-ICP-MS which may lead to the establishment of more and different indicator elements (proxies). A more detailed study will be shown in the following chapter.

7 Element distribution profile on a stalagmite

The work presented in this chapter resulted from collaboration with Dr. Sebastian F. M. Breitenbach (Climate Geology, ETH Zurich), who provided the sample and was involved during analysis and data evaluation.

7.1 Introduction

Speleothems are secondary $CaCO_3$ mineral deposits, typically found in caves. Stalagmites are particularly important archives of past climate [189] due to their ubiquous distribution on the continents, steady growth, durability over tens of thousands of years and their capability to incorporate various trace elements into aragonite or calcite. Such trace element variations in secondary cave carbonates record valuable information of past climate conditions. Together with accurate U-series dating and stable isotope variations[190], high resolution trace element profiles [27] or imaging [29,31], may become a powerful multi-proxy tool for paleo-climate reconstruction.

Our study site, Krem Umsynrang cave, is located on the Meghalaya plateau, NE India. The collected stalagmite KRUM-3 was found far from the entrance and ca. 40 m below surface (Figure 45).

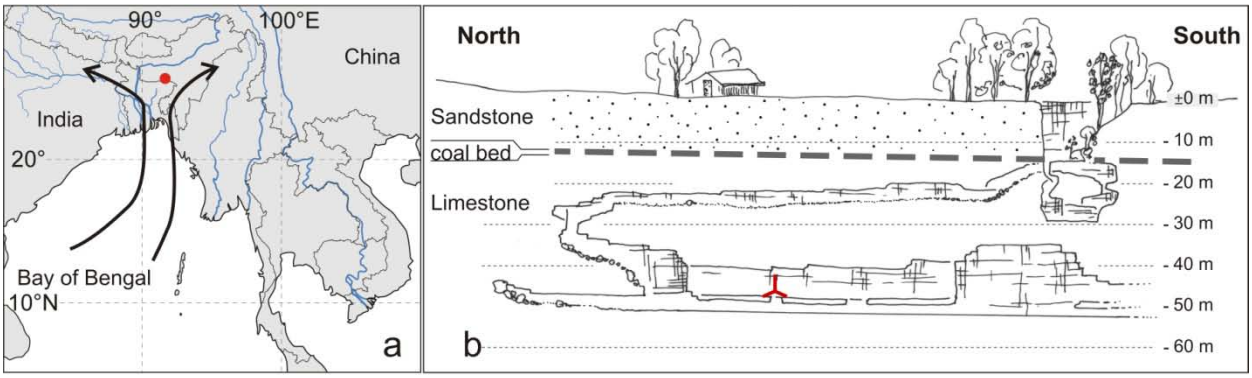

Figure 45: Map of the study area in India (a), location of the Krem Umsynrang cave marked by the red dot. The arrows indicate the route of the Bay of Bengal branch or the Indian Summer Monsoon. Profile of Krem Umsynrang cave (b), entrance 825 m a.s.l., red mark shows the location of the KRUM-3 stalagmite. Sketch (a) and (b) from [191] and original map of (b) with courtesy of H. D. Gebauer, 2007.

For transportation reasons it was broken into three segments, see Figure 46. It covers the entire Holocene[2] (~11000 years) in ~64 cm total length. Due to the Indian Summer Monsoon (ISM) and the Meghalaya plateau, this location is one of the wettest regions on Earth. Understanding past ISM variability may allow insights into the range of natural changes and predictions of rainfall changes which is vital information for South Asian economies.

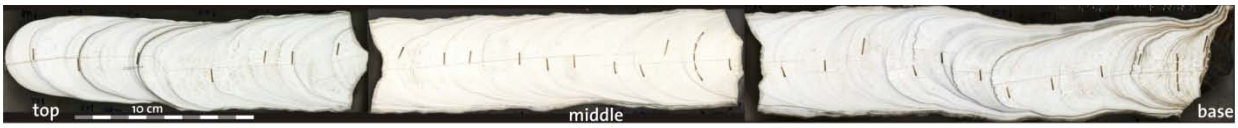

Figure 46: Cross-section of the three pieces of the stalagmite from NE India, covering 11000 years from base to top.

A method for quantitative analysis of large and heterogeneous samples with LA-ICPMS, which necessitates the new design of an ablation cell (Figure 47) was developed. This study is one of the first applications of the LDHCL-ablation cell [105], which was developed to host each of the three pieces of this stalagmite sequentially for profiling (chapter 2.5).

[2] Holocene (11.7 thousand years ago to present) is a geological epoch following the Pleistocene, which both form the Quaternary period (2.59 million years ago to present). It is the youngest interglacial. The beginning of the Mesolithic corresponds with the beginning of the Holocene.

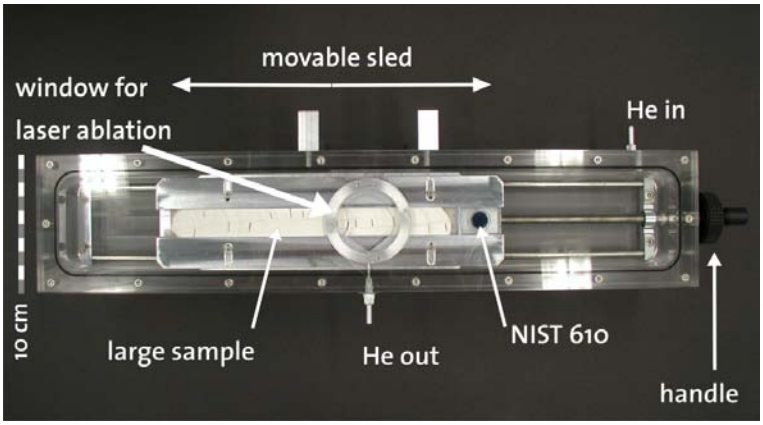

Figure 47: Photograph of the stalagmite sample KRUM3-top and an external standard mounted on the sample sled. The sled was moved sequentially to acquire the trace elements by LA-ICP-MS.

Although this analytical method is capable of providing quantitative data for main and trace element distribution, the interpretation of the results is challenging. Climate reconstruction relies on proxies (i.e. variation of concentration of various elements indicating physical characteristics such as temperature, humidity, etc.), which are still to be conceived by trace element analysis in the case of stalagmites. The incorporation of elements and the fractionation of isotope species during deposition from the fluid phase into the crystal lattice requires high spatial resolution analysis. In a study of a sediment core [181] from the Cariaco Basin, it was qualitatively found that the relative amount of Ti present in the dated varves[3] is a proxy for the amount of rainfall. This relation was used to infer that several intense multiyear droughts lead to the collapse of the Maya civilization. The geological setting of a stalagmite is entirely different to marine sediments, and thus an alternative set of proxies must first be established for paleo-climate reconstructions. Using the developed method demonstrates that quantitative results of main and trace element distribution with a high resolution are possible to obtain, and feasible for any solid sample that can be placed within the LDHCL-ablation cell.

7.2 Experimental and methods

The cell was developed and engineered in-house and designed to accommodate large samples with maximum dimensions of 230x34x16 mm (LxWxD) in an airtight plexiglas

[3] A varve comprises layers of sediment formed within one year, provided that several discriminable layers were formed by seasonal changes in the sedimentary system. Varves can be counted to establish a chronology, if the age of one or several of them is known or dated independently (e.g. ^{14}C dating).

body. Its design allows fitting the sample on a sled and a handle for repositioning of the sample manually without the need of opening the cell. Keeping the ablation cell closed eradicates the requirement of a fast opening mechanism and reduces idle time of the ICP-MS when flushing the ablation cell from ambient gases. To perform line scans through the 50 mm diameter ablation window, the cell (chapter 2.5) is mounted onto a computer-controlled xyz-stage. This, in combination with manual sliding (between line scans) permitted scanning of the entire sample. All analyses were carried out using an ArF excimer laser at 193 nm (GeoLasC, Lambda Physik, Göttingen, Germany) coupled to a quadrupole ICP-MS (ELAN DRC II, Perkin Elmer Inc., Woodbrigde, Canada). Instrument conditions of the laser and the ICP-MS are listed inTable 8. A total of 117 segments from top to bottom on the cross-sections of the three stalagmite segments were acquired on different days following a protocol of external calibration [66] using SRM NIST 610 and $^{42}Ca^{+}$ in $CaCO_3$ as internal standard. Cleaning scans with different settings were applied prior to each acquisition scan (Table 8). Quantification of carbonates using SRM NIST 610 was validated by analyzing the carbonate standard SRM MACS-1 and the obtained deviation from the reference values (USGS preliminary certificate and GeoReM published values [192]) are shown in Figure 48. Generally, an underestimation of 20% was observed for most elements, and K and Y deviated by -40%. The non-matrix-matched approach to quantify carbonates using NIST multi-element glass standards was successfully reported by Chen et al. [69], Roberts et al. [70], Sanborn and Telmer [71] and references therein. Furthermore, the particle size distribution of several samples (Background, NIST 610, NIST 612, MACS-3, MACS-1, KRUM-3, and Background again) were acquired using an ultra high sensitivity aerosol spectrometer (BAKRANA, Basel, Switzerland) using the same LA line scan conditions (crater size 32 µm, repetition rate 1 Hz, scanning speed 1 µm, 5 J/cm^2). The carrier gas flow was heavily diluted in order to avoid saturation of the detector. Results are shown in Figure 49 and represent averages of 10 replicates for each sample and 1 SD error bars. No particles were detected for the BG before and after the data acquisition. Particle size distribution for all samples (NIST 610, NIST 612, MACS-1 and KRUM-3, MACS-3) were equal.

Table 8: Instrumental settings of the laser system and the mass spectrometer.

LA Lambda Physik, GeoLasC		ICPMS Perkin Elmer, ELAN 6100 DRCII	
ArF excimer	193 nm	**rf power**	1400 W
scan length	5500 µm	**aerosol gas, He**	1.0 L/min
fluence	6.55 J/cm²	**carrier gas**	0.95 L/min
cleaning scan	**acquisition scan**	**aux. gas**	0.84 L/min
127 µm	63 µm	**plasma gas**	17.0 L/min
1 Hz	10 Hz	**ThO^+/Th^+**	<1.4 %
47 µm/s	20 µm/s	**sweep time**	0.650s
Monitored isotopes:			
$^{7}Li^+$, $^{11}B^+$, $^{13}C^+$, $^{23}Na^+$, $^{24}Mg^+$, $^{25}Mg^+$, $^{26}Mg^+$, $^{27}Al^+$, $^{29}Si^+$, $^{31}P^+$, $^{34}S^+$, $^{35}Cl^+$, $^{39}K^+$, $^{42}Ca^+$, $^{43}Ca^+$, $^{46}Ca^+$, $^{49}Ti^+$, $^{53}Cr^+$, $^{55}Mn^+$, $^{57}Fe^+$, $^{59}Co^+$, $^{60}Ni^+$, $^{65}Cu^+$, $^{66}Zn^+$, $^{71}Ga^+$, $^{79}Br^+$, $^{85}Rb^+$, $^{88}Sr^+$, $^{89}Y^+$, $^{133}Cs^+$, $^{137}Ba^+$, $^{139}La^+$, $^{140}Ce^+$, $^{141}Pr^+$, $^{146}Nd^+$, $^{147}Sm^+$, $^{153}Eu^+$, $^{157}Gd^+$, $^{159}Tb^+$, $^{163}Dy^+$, $^{165}Ho^+$, $^{166}Er^+$, $^{169}Tm^+$, $^{173}Yb^+$, $^{175}Lu^+$, $^{178}Hf^+$, $^{181}Ta^+$, $^{208}Pb^+$, $^{232}Th^+$, $^{238}U^+$			

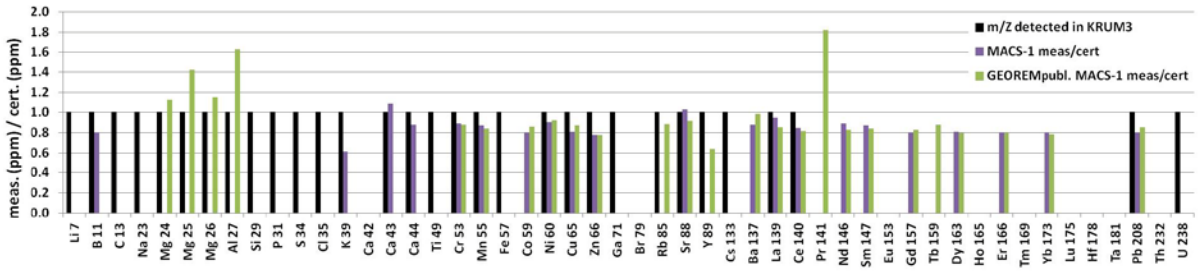

Figure 48: Deviation of the obtained concentrations for MACS-1 analyzed as sample. The quantification was based on 42Ca as internal standard and NIST 610 as external standard. Purple bars represent concentrations normalized to the USGS preliminary certificate, whereas green bars represent concentrations normalized to GeoReM published values [192]. Missing bars (purple or green) indicate at least one value was not available for the element. Black bars identify those elements which were detected in the natural stalagmite KRUM-3.

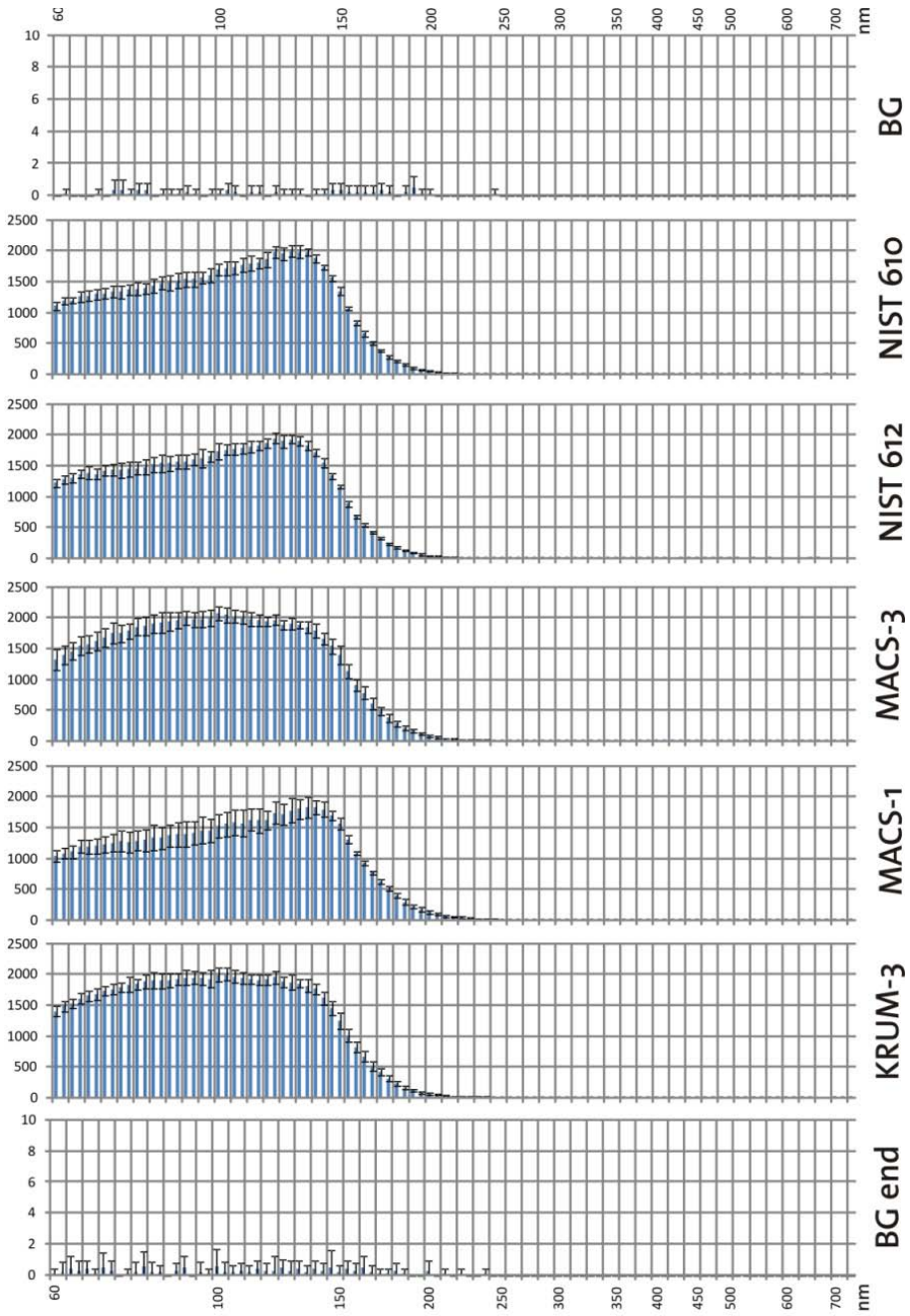

Figure 49: Particle size distribution of background, external standards and sample, acquired under the same LA conditions in the LDHCL ablation cell. Intensities are given in arbitrary units. The error bars show 1 SD of ten replicates for each sample.

An important feature of the ablation cell is the small dispersion (as discussed in chapter 3). In order to acquire high resolution data of a heterogeneous sample a short washout time was crucial. The raw data were background- and drift-corrected and quantified using SRM NIST 610 and matrix standardization (assuming 99.5 wt% of $CaCO_3$). Each sweep (one data point per element) was normalized to 100 wt% sum of the oxides of all measured elements (reported for bulk analysis in absence of internal standard values in [68,149]). Due to the heterogeneity of this natural sample the concentration of the internal standard was not determined by an independent method, but cal-

culated assuming pure $CaCO_3$. Hence the normalization to 100 wt % of the oxides accounted for changes of concentration of the internal standard. Limits of detection were calculated for each line scan using the equation shown in Figure 25, and values <LOD were rejected. Finally, all scans were assembled to gain one profile of each of the three parts of the stalagmite (Figure 50). A computer program capable of performing all of these calculations necessary for data analysis was developed after the completion of this technical method for stalagmite analysis and is presented in chapter 4. Prior to the laser ablation procedure the stalagmite was subjected to U-series dating (34 samples) and $\delta^{18}O$ stable isotope analyses (1439 samples), for both of which the sampling was performed by milling of drill holes. Further details of this sampling strategy are given in [191]. The laser ablation was off (shutter closed) while the line scan was progressing across such holes and thus no trace element data are available at such positions.

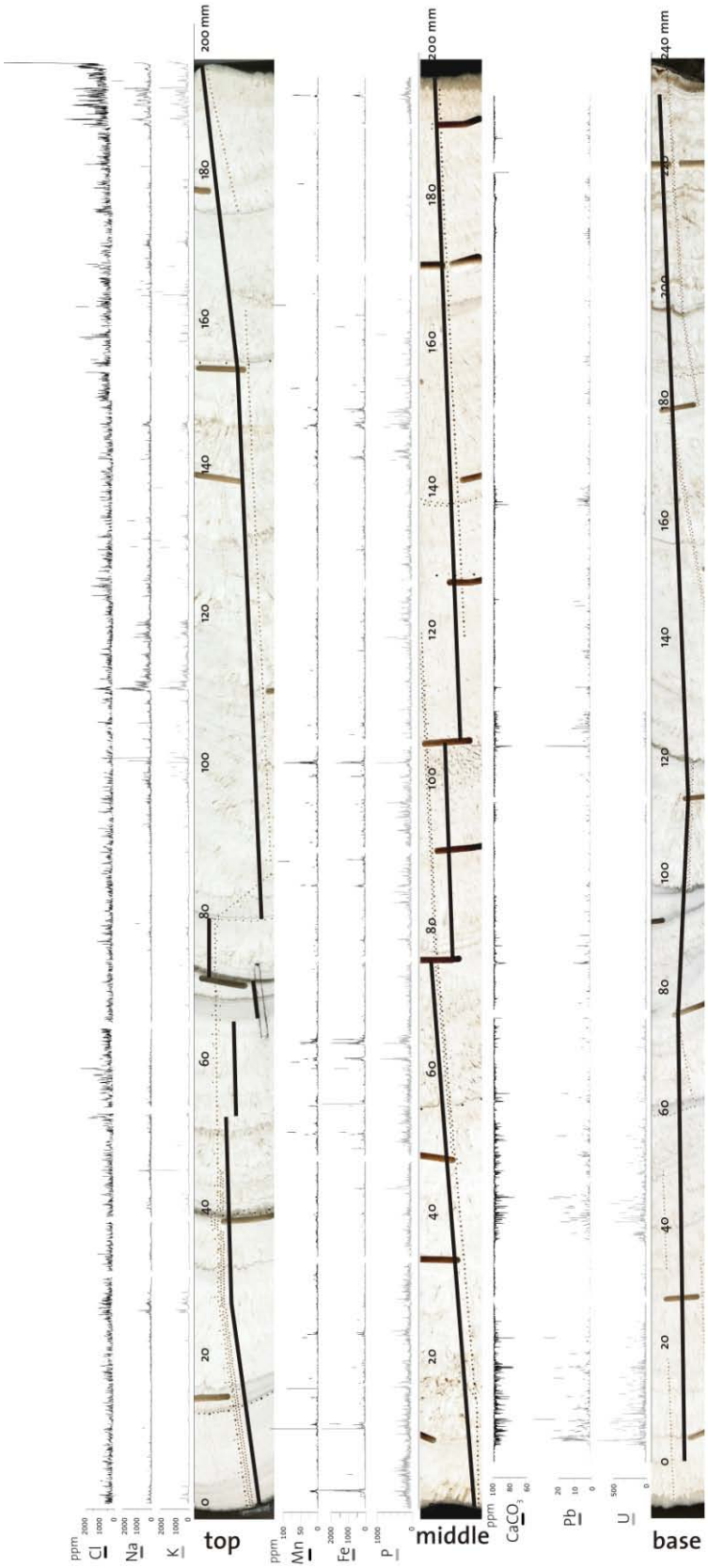

Figure 50: The results are shown for the top, middle and base segment of KRUM-3. A selection of 9 element profiles is displayed. Exemplary for all of the acquired elements, all concentrations are given in µg g-1 (ppm) except Ca (in wt % of the carbonate). The black line on the images indicates the position of the laser scans. The young side of each segment is on the bottom of the image.

The chosen instrumental settings (see Table 4) result in a 13 µm drive within one acquired sweep (i.e. one data point for each isotope monitored) which was equal to more than 6 ablation pulses with an offset of 2 µm between the pulses (Figure 51). It needs to be mentioned that these values do not render lateral resolution on the sample, as the crater size must be considered, yielding roughly 60% overlap of ablated area from the first to the last of six ablation pulses within one sweep (not considering dispersion of the aerosol in ablation cell and transport tubing). The laser ablation parameters were chosen such that a constant flow of laser-generated aerosol is transported to the Q-ICP-MS, where it is analyzed sequentially. Therefore, one single laser pulse does not correspond to one data point. Albeit a mix of several ablation pulses contribute to the recorded transient signal, it is possible to detect sample features smaller than the crater diameter (depending on the concentration of such a feature), as it has been shown by Senoner et al. [135]. However, the lateral resolution of line scans on a heterogeneous sample cannot be accurately described due to diverse unknowns, such as magnitude of micro-scale concentration differences in the sample at the micro-scale, aerosol dispersion, and the fact that data points are not correlated to specific ablation pulses on the sample. Estimations can be given considering the 13 µm drive between datapoints and the fact that the highest signal (^{23}Na) decreases over 3 orders of magnitude within less than 2.6 s (corresponding to 4 datapoints at a sweeptime of 0.650 s) which results in an estimated lateral resolution of 52 µm. All other monitored isotopes have lower intensity than ^{23}Na and are therefore washed out within less than 2.6 s resulting in <52 µm estimated lateral resolution. Jilbert et al [129] have estimated a lateral resolution of 30 µm using 0.8 s sweeptime and 25 µm scanning speed.

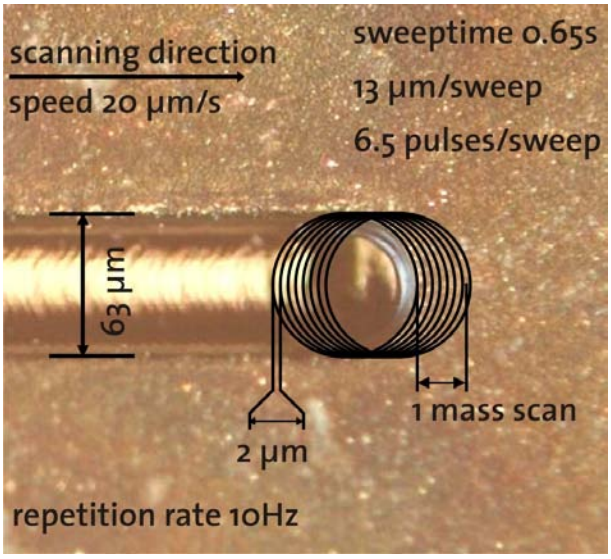

Figure 51: The relationship of instrumental settings is illustrated in this figure, shown as an example on lake sediment embedded in epoxy (chapter 6). More than 6 ablation pulses, with 2 µm offset, overlap to contribute to one data point of the transient signal recorded by the MS.

7.3 Results

The obtained $\delta^{18}O$ values of the stalagmite record range from present (2004) to approximately 11000 years back in time, to the beginning of the Holocene. Stalagmite growth started after the Younger Dryas[4], and this particular dry period is not contained in this record. However, the trend of $\delta^{18}O$ values of KRUM-3 and the GRIP ice core (Greenland ice core project [193]) match when the scale for the KRUM-3 increases downwards and the scale of GRIP increases upwards, as shown in Figure 52.

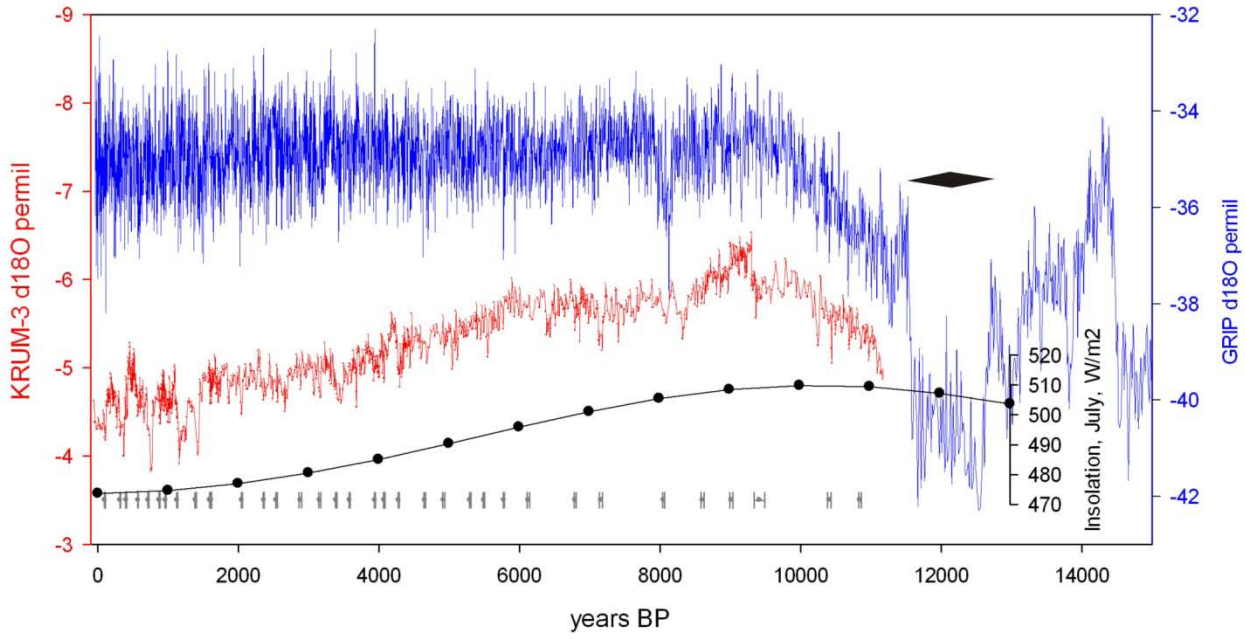

Figure 52: Comparison of the δ18O stable isotope record of KRUM-3 [191] (red) and the GRIP ice core [194] (blue). Results from U-series dating (grey) [191] are plotted at the bottom. The insolation curve data (black circles) from [195], is calculated for the coordinates of the KRUM-3 origin for the month July, based on orbital and precessional quantities of the earth and shows a similar trend as the δ18O results. The Younger Dryas is marked by the black diamond.

Highly negative $\delta^{18}O$ values indicate increased Rayleigh fractionation of moisture from the Indian Ocean, increased total rainfall and freshwater input into the northern Bay of Bengal during the summer season due to stronger summer monsoon, thus changing the moisture source composition and isotopic signal in the rainfall above the study site [196]. Over the course of the Holocene, the ISM rainfall follows changes in the mean northward extent of the ITCZ, itself tracking summer insolation in the northern hemi-

[4] The Younger Dryas was a short period of cold/dry climate (approximately between 12800 and 11500 years BP) interrupting the warming trend after the latest glacial period. This period appears prominently in temperature data of past climate obtained from ice cores and lake sediments, and as drying trend in Chinese stalagmite records.

sphere. The insolation model is computed based on orbital and precessional quantities described by Laskar et al. [197]. Moreover the results for the insolation curve in Figure 52 were calculated [195] using the coordinates of the KRUM-3 origin, and shows the amount of solar radiation received by the earth during July, since this month corresponds to the maximum of the ISM. Such findings of correlation of $\delta^{18}O$ values in stalagmite with ice core and insolation curve were also reported by Yuan et al. [198].

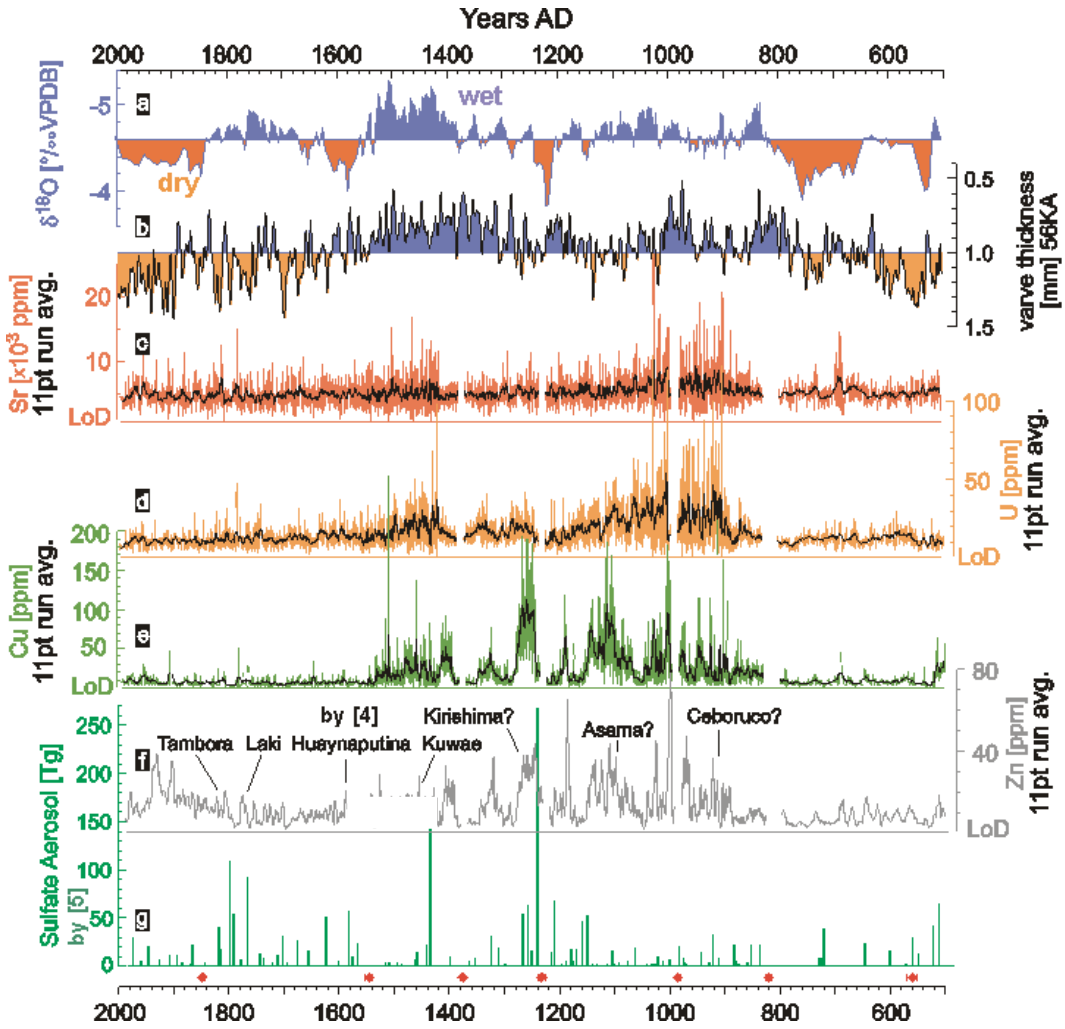

Figure 53: Concentrations of Sr, U, Cu and Zn are plotted for the top 73 mm of KRUM-3 as 11 pt running averages. The ages were obtained from a U-series age model. The varve thickness curve stem from sediment core 56KA of the northern Arabian Sea [199] which was later reinterpreted [200]. Data on past volcanic eruptions, possible events that might have caused the signal change, were obtained from [201]. The sulfate aerosol data are reconstructed from ice cores [202].

The $\delta^{18}O$ profile (Figure 53) coincides with other wet/dry data obtained from varve thickness of a sediment core from the northern Arabian Sea [199,200]. As mentioned above, the trace element profiles of the stalagmite reveal higher concentrations during the wet phase, reflected in the $\delta^{18}O$ data. The profiles of Cu and Zn are overlapping during the wet phase. Moreover, Cu and Zn peaks may correspond to volcanic erup-

tions [201] (aerosol spikes [202]), although further work is needed to prove this relationship. Acid rains after volcanic eruptions cause changes in soil acidity and Cu, Zn leaching by the percolating water, thus enhancing transport into the cave.

The complexity of the interpretation of such large datasets is illustrated in Figure 54. It is challenging to accurately correlate the signal to the photomicrograph for such small structures and signal variations. In a first attempt the trends of the trace element variability on the entire sample (Figure 50) was established.

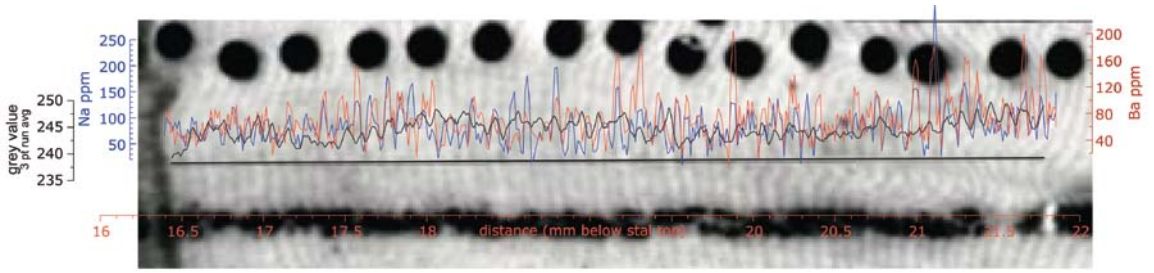

Figure 54: A close-up high resolution photograph of 6 mm of KRUM-3. The scan image was converted to black and white with contrast strongly enhanced in order to visualize individual layers of the stalagmite growth. The growth rate at this position corresponds approximately to 100 µm per year (the laser crater diameter used for this study in line scanning mode was 63 µm). As an example the profiles of Na and Ba were plotted with grey scale values obtained from the photograph.

7.4 Summary

Detailed long-term monitoring of the drip water chemistry inside the cave is necessary to compare with coeval carbonate deposition on the stalagmite in order to understand the influence of climate processes on trace elements profiles, i.e. obtaining independent evidence for robust proxies.

The morphology of the sample plays an important role in the interpretation of the results and the reproducibility of the obtained trace element profiles within the stalagmite and between coeval samples. As reported by Roberts et al. [70] and Treble et al. [27], the element data obtained from two neighboring stalagmites are probably not coherent, threatening the potential use of trace elements in stalagmites as robust climate archives. This is in contrast to marine sediments, where the elements reservoir is well-mixed by the ocean.

The final version of the LDHCL-ablation cell (chapter 2.5) developed in this study was motorized and allowed controlled and accurate line scan ablation. Furthermore movement in x-direction of the stage was replaced by moving the sample sled using the motor during laser ablation. This technical development kept the cell dispersion constant and provides significantly improved data. The LA position was not changed with respect to the window during a line scan. Together with the LA data reduction program STALQUANT (chapter 4), it was possible to acquire and calculate the data efficiently.

The entire KRUM-3 element profile comprises nearly 48000 data points per monitored isotope (for 640 mm of stalagmite). This demonstrates that the current set-up is capable to analyze large samples with high spatial resolution. However, it is important to note, that it is particularly challenging to derive an interpretation of such large datasets. Accordingly one of the prospective steps in the future will address at statistical processing, for example principle component analysis, as a means of further data reduction. Additionally, elemental imaging is a way to gain insight into reproducibility and significance of individual signal variations, i.e. whether a particular variation in the trace element profile is inherent from the sample or is caused by a grain or dust particle will become very important. Until now only little data using LA-ICP-MS are available. Therefore, many different systematic studies on stalagmites need to be carried out to improve the general understanding of the underlying growth processes. The set-up developed within this thesis is currently routinely applied to stalagmite analysis within the sinergia project STALCLIM (SNF project CSR122_646/1), which was the major aim of this PhD thesis.

8 Map of a pearl section

The work presented in this chapter resulted from collaboration with Francesca Peretti (GemResearch Swisslab, Lucerne), who provided the sample.

8.1 Introduction

Mapping capabilities of the LA-ICP-MS system using the LDHCL-ablation cell (chapter 2.5) were demonstrated on a cross-section of a drop-shaped salt water cultured pearl of a black-lipped pearl oyster (*Pinctada margaritifera cumingii*) from the Republic of Fiji. The pearl analyzed within this study (NF120, GRS-ref#535-0177, GemResearch Swisslab, Lucerne, Switzerland) originates from the Republic of Fiji, was untreated and of natural colour consisting of a metallic-anthracite luster and yellow-green coloured nacre in the cross-section. This species originates from French Polynesia, but is cultured in Salomon Islands, Fiji, Marshall Islands, Kiribati, Hawaii and Iran [203]. The residence time of the bead inside the pearl oyster was approximately 2 years, during which it was coated with several layers of nacre[5].

[5] Nacre is composed of aragonite ($CaCO_3$) platelets embedded in an organic matrix.

8.2 Experimental and methods

The pearl was cut through the center using a diamond cut-off wheel on an ACCUTOM circular saw (both by Struers), and one piece (~11 x 14 mm) was embedded in epoxy resin (EpoFix Kit, Struers, Switzerland, left for drying overnight at 40°C), for simple handling and unproblematic positioning of the line scans, as illustrated in Figure 55.

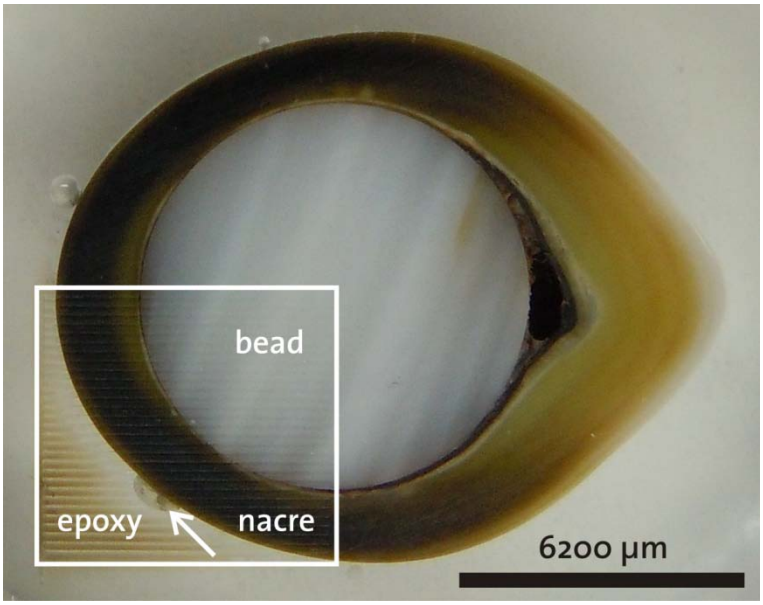

Figure 55: Photograph of the pearl (GRS-ref#535-0177) cross section. The white frame marks the area which was analyzed, individual line scans are visible. The arrow points to a bubble in the epoxy resin, where the laser ablation was interrupted during analysis, and hence no results are available for that area.

All analyses were carried out using an ArF excimer laser at 193 nm (GeoLasC, Lambda Physik, Göttingen, Germany) coupled to a quadrupole ICP-MS (ELAN DRC^{plus}, Perkin Elmer Inc., Woodbrigde, Canada). The sample was mounted in the LDHCL-ablation cell [105], which was optimized for profiling/mapping of heterogeneous samples (chapter 2.5), together with the SRM NIST 610. A total of 29 line scans of a length of 6200 µm with 200 µm spacing between them were acquired. All line scans mutually covered an area of 6.200 by 5.800 mm, i.e. one quadrant of the pearl cross-section. Laser ablation was performed across epoxy, nacre and bead (Figure 55), thereby simplifying the data acquisition as well as data reduction and plotting of the quantitative results. Cleaning scans with different settings were applied prior to each acquisition scan (Table 9). An external calibration [66] using SRM NIST 610 and $^{42}Ca^{+}$ internal standard procedure was applied for quantification. Acquisition file numbers (01, 02, 18, 19, 34, 35) were measured on the external standard in order to quantify data series with external standard pairs at the beginning and the end of a series. The concentration of the internal standard was assumed to be pure $CaCO_3$ (aragonite) whereby normalization of the re-

sults to 100 % wt of the oxides [68,149] accounted for deviation from the stoichiometric concentration. The raw data were quantified and arranged for plotting using the in-house developed computer program STALQUANT described in chapter chapter 4. All element distribution maps were generated using the map results output from STALQUANT. The map results file was processed as a batch using a macro (appendix D) written in the image processing program *FIJI* [150] which is a distribution of *ImageJ* [151].

Table 9: Instrumental settings of the laser system and the mass spectrometer.

	cleaning	acquisition
LA		
instrument	GeoLasC	
energy density [J cm^{-2}]	18.5	
scan length [µm]	6200	
Spacing between lines [µm]	200	
crater size Ø [µm]	120	60
repetition rate [Hz]	2	10
scanning speed [µm s^{-1}]	100	20
ICP-MS		
instrument	ELAN 6100 DRC^{plus}	
RF power [W]	1400	
carrier gas, He [L min^{-1}]	1.0	
nebulizer gas, Ar [L min^{-1}]	0.85	
aux. gas, Ar [L min^{-1}]	0.75	
plasma gas, Ar [L min^{-1}]	17.5	
dwell time [ms]	10	
sweep time [ms]	650	
# of isotopes	50	
Isotopes monitored:		
$^{7}Li^{+}$, $^{11}B^{+}$, $^{13}C^{+}$, $^{23}Na^{+}$, $^{25}Mg^{+}$, $^{27}Al^{+}$, $^{29}Si^{+}$, $^{31}P^{+}$, $^{34}S^{+}$, $^{35}Cl^{+}$, $^{39}K^{+}$, $^{42}Ca^{+}$, $^{44}Ca^{+}$, $^{49}Ti^{+}$, $^{51}V^{+}$, $^{53}Cr^{+}$, $^{55}Mn^{+}$, $^{57}Fe^{+}$, $^{59}Co^{+}$, $^{60}Ni^{+}$, $^{65}Cu^{+}$, $^{66}Zn^{+}$, $^{71}Ga^{+}$, $^{79}Br^{+}$, $^{85}Rb^{+}$, $^{88}Sr^{+}$, $^{89}Y^{+}$, $^{90}Zr^{+}$, $^{93}Nb^{+}$, $^{105}Pd^{+}$, $^{107}Ag^{+}$, $^{111}Cd^{+}$, $^{118}Sn^{+}$, $^{121}Sb^{+}$, $^{127}I^{+}$, $^{133}Cs^{+}$, $^{137}Ba^{+}$, $^{138}Ba^{+}$, $^{139}La^{+}$, $^{140}Ce^{+}$, $^{141}Pr^{+}$, $^{153}Eu^{+}$, $^{163}Dy^{+}$, $^{197}Au^{+}$, $^{202}Hg^{+}$, $^{205}Tl^{+}$, $^{208}Pb^{+}$, $^{209}Bi^{+}$, $^{232}Th^{+}$, $^{238}U^{+}$		

8.3 Results

A representative transient signal for pearl analysis is shown in Figure 56. Contributions of the three phases (epoxy, nacre and bead) of the sample can be distinguished. In order to fingerprint pearls, only the composition for nacre is of importance, formed of hexagonal aragonite ($CaCO_3$) platelets embedded in an organic matrix [203]. A natural pearl is composed of 91.50 % $CaCO_3$, 3.83 % organic matter, 3.97 % water, and an unknown rest of 0.01 % [204]. The organic matter is mostly composed of conchin which is cementing the aragonite platelets. The center of natural pearls consists of prismatic layers (calcite) and the outer layers of aragonite platelets, whereas high Sr content in the water favors formation of aragonite in the pearl center [203]. In the nacre of this sample B, C, Na, Mg, S, Cl, K, Ca, Mn, Fe, Sr and were above limits of detection, as listed in Table 10. The Mg concentration in nacre (aragonite) is low and Sr concentrations of 1400 µg g^{-1} are consistent with the typical values for mollusc shells (1000-2000 µg g^{-1}) [205,206]. However, Dauphin et al. [205] reported high Mg concentrations of more than 25000 µg g^{-1} in the prismatic layers (calcite) found in the center of a natural pearl. In the cultured pearl of this study less than 100 µg g^{-1} of Mg in the nacre were determined, indicating the absence of prismatic layers in the pearl center, where the center of this cultured pearl is not natural, i.e. the bead. The element concentrations in the pearl match those reported in shells, *Pinctada margaritifera*, French Polynesia [207], B 12 µg g^{-1}, Na 5500 µg g^{-1}, Ca 396000 µg g^{-1}, Fe 70 µg g^{-1}, Sr 900 µg g^{-1}, except Mg 2100 µg g^{-1}, Mn 2000 µg g^{-1}, Cu 1000 µg g^{-1}. The higher content of Mg, Mn and Cu in the shell from French Polynesia may be due to the differences of the subspecies, biominerals (shell vs pearl) and location of the origin.

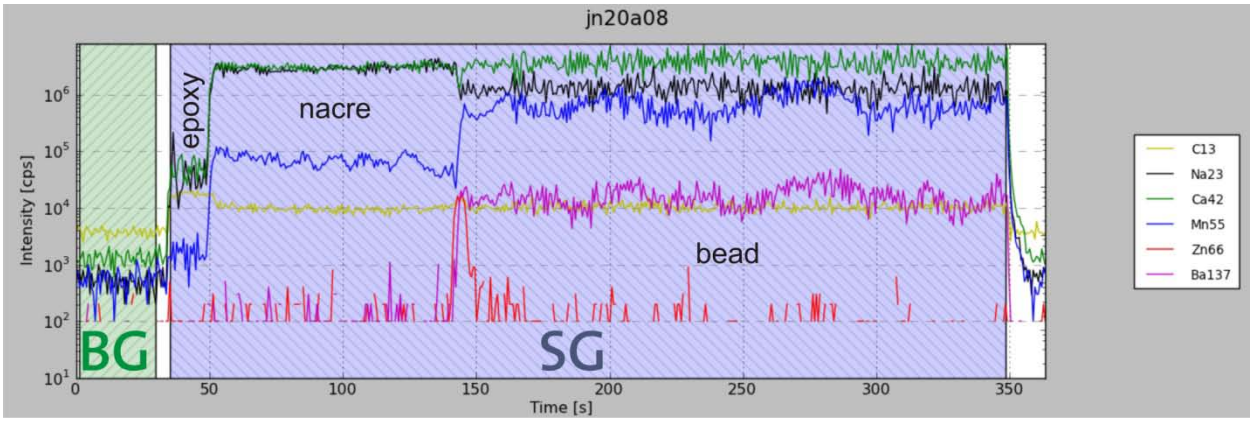

Figure 56: A representative transient signal for pearl analyses. The ablationrepresents line scan number 6 counting from the top in Figure 55 and Figure 57. The background (BG) and signal (SG) intervals are shaded green and purple, respectively. Epoxy, nacre and bead contribution are marked in accordance to Figure 55.

Table 10: Results from bulk analysis of nacre, average and 1 relative standard deviation (RSD) of n=29, limits of detection (LOD) are expressed as 3xSD of BG/Sensitivity of sample.

Element	Concentration [µg g^{-1}]	RSD %	*LOD [µg g^{-1}]*	Element	Concentration [µg g^{-1}]	RSD %	*LOD [µg g^{-1}]*
Li	<LOD		*1.1*	**Sr**	1425	4.2	*0.40*
B	17.1	7.9	*11*	**Y**	<LOD		*0.11*
C	2.65	10	*0.99*	**Zr**	<LOD		*0.25*
Na	5000	5.7	*1.6*	**Nb**	<LOD		*0.14*
Mg	79	13	*3.3*	**Pd**	<LOD		*0.55*
Al	<LOD		*2.5*	**Ag**	<LOD		*0.29*
Si	<LOD		*260*	**Cd**	<LOD		*1.6*
P	<LOD		*25*	**Sn**	<LOD		*0.30*
S	604	13	*260*	**Sb**	<LOD		*0.29*
Cl	330	17	*120*	**I**	N/A		*N/A*
K	49.3	16	*4.7*	**Cs**	<LOD		*0.06*
$^{42}Ca^{+}$	IS			**Ba (on $^{137}Ba^{+}$)**	<LOD		*0.75*
Ca (on $^{44}Ca^{+}$)	389400	1.9	*210*	**Ba (on $^{138}Ba^{+}$)**	0.32	22	*0.17*
Ti	<LOD		*3.4*	**La**	<LOD		*0.09*
V	<LOD		*0.28*	**Ce**	<LOD		*0.08*
Cr	<LOD		*4.0*	**Pr**	<LOD		*0.08*
Mn	75	16	*0.89*	**Eu**	<LOD		*0.17*
Fe	28.2	11	*15*	**Dy**	<LOD		*0.47*
Co	<LOD		*0.24*	**Au**	<LOD		*0.49*
Ni	<LOD		*1.1*	**Hg**	N/A		*N/A*
Cu	<LOD		*0.88*	**Tl**	<LOD		*0.17*
Zn	<LOD		*1.7*	**Pb**	<LOD		*0.18*
Ga	<LOD		*0.31*	**Bi**	<LOD		*0.13*
Br	<LOD		*98*	**Th**	<LOD		*0.10*
Rb	<LOD		*0.12*	**U**	<LOD		*0.07*

For simplification of handling the calculations and plotting, all three phases are reported, revealing noteworthy features in the bead. For example, the bright and dark features of the bead (see photograph Figure 57) can be observed as changes in intensity of the transient signal of Mn and Ba. Furthermore, the Mn signal shows intensity changes for the nacre phase, which add up the lines of distinct growth zones of the pearl shown in Figure 57b. The presence of Zn (and other elements: Mg, S, Cl, K, Sr, and traces of B, P, Fe, Cu, Br, see Figure 58) in the transition zone from nacre to bead were also detectable. The trace element pattern indicates a bonding of nacre and bead which is most likely an organic layer.

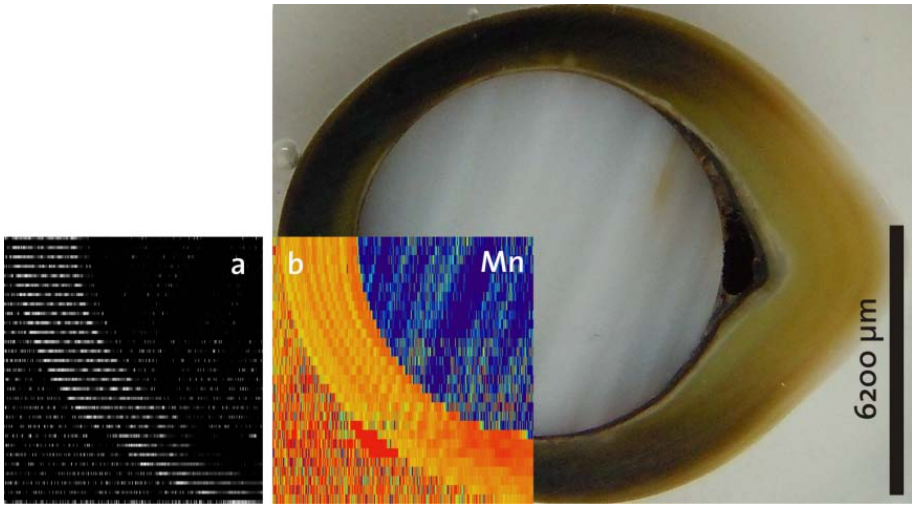

Figure 57: The measured distribution of Mn is represented in a black and white image (a) and overlaid using false colors (b) on a photograph of the pearl cross section. The bright and dark features of the white bead are clearly reproduced in the Mn distribution (a). Several layers of different Mn concentrations in the nacre are visualized by the nuances of orange. The values at the location of the bubble were set to zero prior to image generation, indicated by the small red area (see Figure 55).

In order to reproduce the image based on the measured data only, the distance between individual line scans was filled by black bars (Figure 57a). These sampling parameters (Table 9) were chosen such to demonstrate that features in element distribution at the µm scale can be visualized without LA scanning of the entire surface. However, decreasing the distance between line scans and thus increasing the number of line scans and measurement time results in more detailed elemental maps. To increase legibility, the black bars representing non-sampled area were omitted and the pixels elongated to fill in the gap (Figure 57b). No smoothing functions were applied, and thus each pixel represents one data point. Gradients from mathematical interpolation between data points may create artifacts in surface plots, as discussed in chapter 4, which do not necessarily represent features of the pearl. Nevertheless, automatic contrast enhancement was necessary to make sample features clearly visible on each element map. Moreover, this step introduced a non-linear color scale [145] increasing peculiarity of tiny features, but eliminating all quantitative information, hence only relative differences are highlighted. To present the maps in a quantitative way, another approach of enhancing the contrast needs to be established or the non-linearity of the color scale needs to be presented in each map.

The thin lines of different concentration of some elements in the nacre are very prominent in the upper half of the map (Figure 57b and Figure 58), where the line scans were performed perpendicularly to the lines in the sample. However, in the lower half the lines in the nacre appear blurred. This is an effect of the gaps between line scans which is strong when scanning parallel to the lines in the sample. This effect is so dominant, because the crater size of the ablation (60 µm) is on the same order of magnitude as the thickness of the line (approximately 70-100 µm) within the sample. Overall it is more straightforward to resolve small sample features when performing the line scans

perpendicularly to the features, rather than parallel. Placing more line scans in that area should reproduce the line pattern seen in the sample. Furthermore, this effect should be inverted when the line scan direction is turned by 90°.

In the Mn distribution seven dark and seven bright layers were observed but direct evidence to the two years age of the pearl cannot be assured, suggesting formation of four layers per year (formation of various layers per year in mollusks depend on season, temperature or stress [208]). Outridge et al. [209] and Lutz et al. [210] reported that mollusc shell growth consists of thin layers of alternating $CaCO_3$ and organic matrix, however it is not clear whether this correlates to the observed layers in the nacre of this sample. And, as the time period between the alternations is unknown the connection to the observed layers is difficult.

Element concentrations above limits of detection or heterogeneous distribution in the sample are shown in Figure 58 as element images. The air bubble in the epoxy, indicated in Figure 55, clearly stands out in the image for Cl, i.e. the blue area formed from four line scans within the red area representing the ablation on the epoxy. This area is equal in all of the images. Furthermore, five line scans suffered from short periods of spectral skew during ablation of the nacre, the effect of which relates to the disorder seen light blue in the Si image. This can be found in all other element images, where the element concenctration is above limits of detection. The exact cause for the spectral skew when using the LDHCL-ablation cell are unknown. However, some possibilities were discussed in chapter disschapter 3. Spectral skew was reported by several groups [78,137,211], using various ablation cells, thus it is not occuring exclusively in the LDHCL-ablation cell.

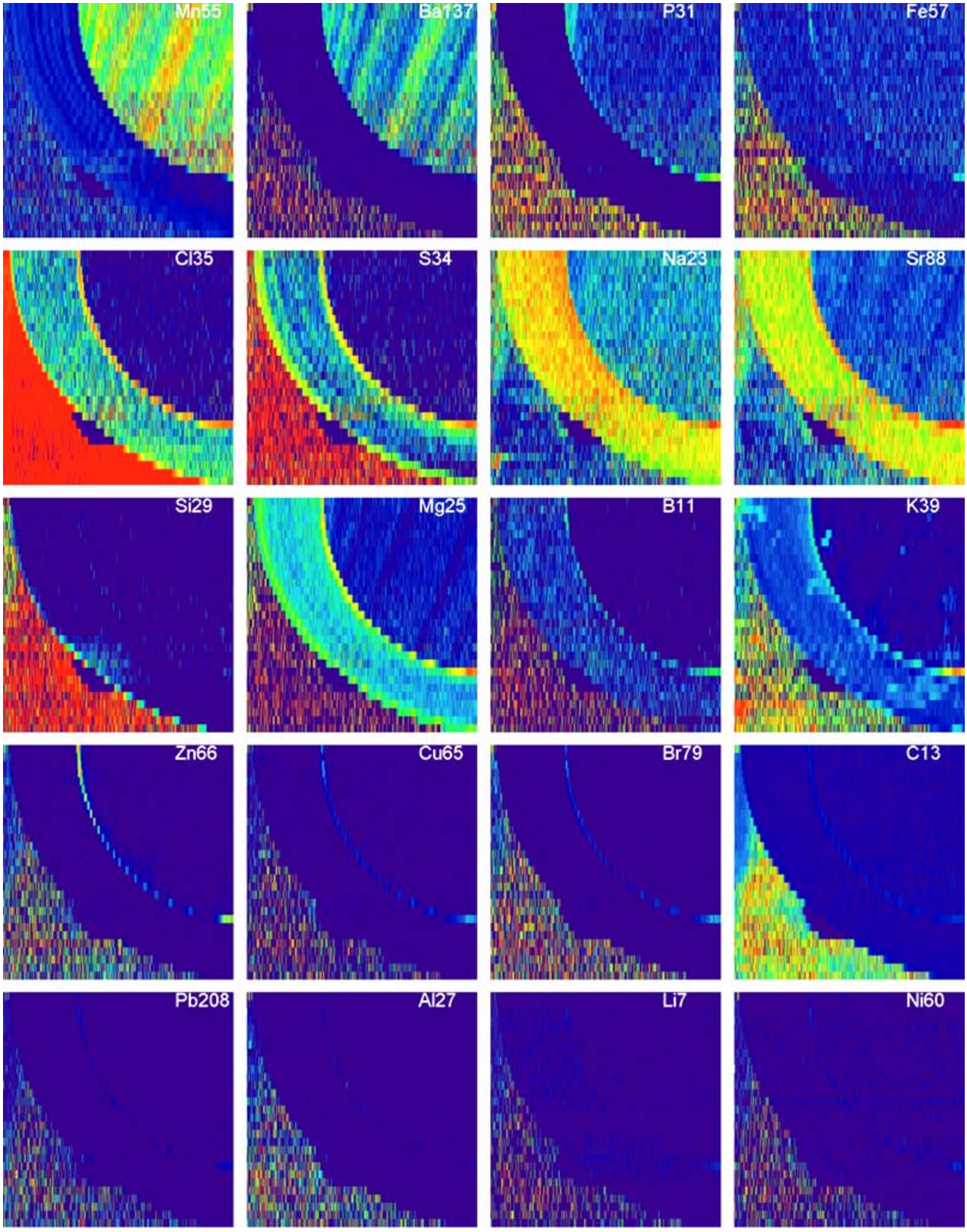

Figure 58: Images of selected elements, the number indicates on which *m/Z* the data was acquired. Note that for each element an individual color scale was applied during the automatic contrast enhancement while generating the plots. In order to make the important features in element distribution visible, a non-linear color scale was applied to the quantitative results. Hence, the colors do not represent quantitative data anymore, but rather images of relative distribution of the elements.

Further understanding of trace element distribution in pearls by LA-ICP-MS is currently investigated to gain more information about pearl characteristics such as age, quality, and provenance. Although the sample was destroyed within this study by cutting to access the cross-section, surface analysis or drilling into the pearls might provide similar information. Single hole drilling leaves a hole in the sample according to the size of the crater e.g. 60 µm. This hole for analysis can be placed at the position where it would later be drilled to put it on the strand of a necklace. The transient signal from single hole drilling produces similar transient signals as the radial line scans, thus the obtained results are expected to be equivalent. However, the depth that can be reached with LA is limited. The trace element composition of a pearl may contain information about its provenance. However, for fingerprinting of pearls large datasets (forming a reference library) need to be acquired to distinguish different locations or natural and synthetic pearls. The imaging as shown in this study indicated that the most valuable information is found for the elements Mg, K and Mn in the nacre and Mg, Cl, K, Cu, Zn, Br and Sr in the layer connecting bead and nacre.

9 Summary and outlook

9.1 Summary of the studies carried out within this PhD project

Trace element concentration determination in individual Fluid Inclusions found in the gigantic gypsum crystals from a cave system in Naica, Mexico was performed using the standard cylindrical ablation cell and quantitative LA-ICP-MS data contributed to the understanding of the growth process of these unique crystals.

Computational fluid dynamic modeling was performed on the standard cylindrical ablation cell to understand gas flow dynamics which are important for transport of laser generated aerosol. Several new geometries were tested and gas flow velocities modeled to find a configuration permitting fast washout of the aerosol, a requirement for profiling and mapping of heterogeneous samples. The gas flow velocity distribution models revealed the important factors that influence gas flows. It is necessary to prevent the formation of vortices which trap aerosol and increase mixing of particles from different laser pulses. It was also shown, that indirect gas flow over the sample surface

is inevitable for fast washout. As a consequence, it was demonstrated that the total volume of the ablation cell is insignificant, as long as gas flow conditions in the effective volume, where laser ablation takes place, are optimal. Considering these facts, a large ablation cell capable of hosting large or many samples was developed, manufactured and tested.

The Low Dispersion High Capacity Laser Ablation Cell (LDHCLAC) incorporates the ability to host large samples while maintaining fast aerosol washout (few seconds) in the effective volume. The geometry guides the gas flows in a way that allows accessing the entire sample area under the ablation window for LA sampling, making the narrow tube cell design unnecessary. Nonetheless, sample size is no longer restricted by the diameter (50 mm) of the ablation cell window due to the large size of LDHCLAC and a sample sled design. It is possible to manually move the sample and thus access the entire sample surface without the necessity to open the ablation cell. The maximum sample dimensions are up to 230x34x16 mm (LxWxD) which allows mounting of sediments, stalagmites, multiple small samples or valuable objects that cannot be cut or damaged in order to fit into the standard ablation cell. The capability of acquiring qualitative and quantitative results of major, minor and trace elements were evaluated for bulk analysis and the application range expanded by demonstrating profiling and mapping on natural samples. The ablation cell was successfully mounted onto the computer controlled xyz-stages of GeoLas C (ns laser system) and the fs laser system and allows reproducible analyses of larger samples. Performance and capabilities of the LDHCL ablation cell were demonstrated on specific applications summarized in Figure 59.

a) Quantitative LA-ICP-MS results (i.e. trace element profiles) were compared to qualitative element profiles obtained by μ-XRF analysis on a sediment core from Lake Zurich. The comparison demonstrated full correlation of the results from these two independent analytical methods. Laser ablation is advantageous over XRF due to the higher sensitivity and large dynamic range enabling analysis of main and trace elements simultaneously and the ability of obtaining quantitative results, which is rather complex in XRF analysis (chapter 6).

b) The analytical figures of merit of the LDHCL ablation cell were characterized by the analysis of several standard reference materials. Single hole drilling and line scanning were performed, aerosol washout for various locations within the effective volume and signal stability determined. Performing line scans on electrophoresis gels showed the distribution of Hg-labeled protein which was separated in the gel beforehand (chapter 3).

c) A 65 cm long stalagmite section was profiled in three pieces to obtain the trace element distribution from the present to 11000 years in the past. Such a profile contains valuable information on past climate that

was recorded during the time of the stalagmite growth and contributes to extending the understanding of paleo climate in order to predict future climate (chapter 7).

d) A cross section of a cultured pearl was imaged by performing 29 parallel line scans to obtain a surface plot of the trace element distribution in the mother of pearl (chapter 8).

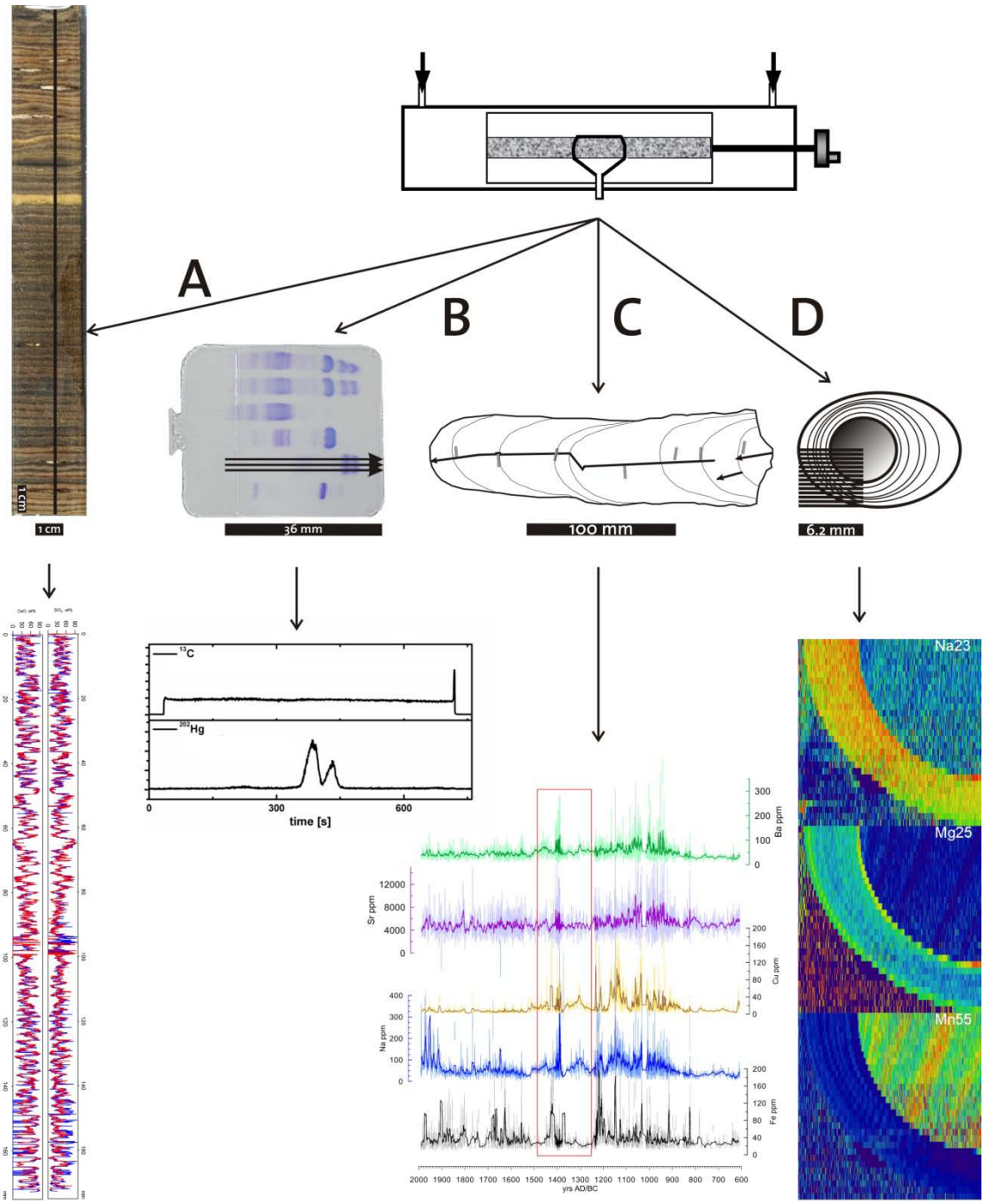

Figure 59: Qualitative (B, Hg labeled protein separated by electrophoresis), quantitative (trace element distribution on a sediment, A, and a stalagmite, C) profiling and elemental imaging (D, trace element distribution in a cultured pearl section) were successfully demonstrated using the LDHCL ablation cell developed in this thesis.

The LDHCL ablation cell has recently become commercially available and ten specimens are currently used by other laboratories worldwide. Nonetheless, further developments were continued and lead to motorization of the sample sled, making the manual movement of the sample sled unnecessary. A prototype of the current version is now motorized, allowing practically to perform a single line scan over the entire 230 mm of available sample surface by computer controlled movement of the sample sled.

Such profiling and imaging analyses produce tremendous amounts of raw data to be quantified, sorted and assembled. As doing so manually consumes a lot of time and is a source of user errors. Overcoming this obstacle lead to the development of STALQUANT, a program specifically devised for the task of quantifying LA-ICP-MS raw data produced by bulk analysis, profiles and images using LDHCL ablation cell or any other.

Several studies using the LDHCLA cell have already been published in peer-reviewed journals, e.g. iron determination in rice grains [22], analysis of platinum group metals in lead fire assay buttons [141], trace element determination in sediment [129], mercury determination in protein separated by electrophoresis gels [105,136], cisplatin-protein complexes separated by 2D gel electrophoresis [212].

9.2 Outlook

The ablation cell portfolio will be completed in the near future, ultimately permitting to analyze any kind of solid or liquid samples regardless of sample size imposed by the three ablation cell types and eventually location-independent analysis by mobile laser ablation with subsequent mass spectrometry in the laboratory.

a) Standard cylindrical ablation cell

   A modification of the cylindrical ablation cell with equal washout characteristics as the LDHCLA cell, is currently investigated by Dietiker et al. [in prep.], permitting profiling and imaging of small samples using the standard ablation cell enhancing gas flow characteristics for fast aerosol washout. This will extend the application range of this versatile ablation cell from bulk analysis to profiling and imaging of small samples.

b) LDHCL ablation cell

   Future versions of LDHCLAC have a motorized sample sled and controls incorporated into the laser software to broaden the accessible range of line scanning by rendering manual movement needless.

c) Ablation without ablation cell

   The introduction of a gas exchange device opened a vast range of possibilities for future LA-ICP-MS applications, specifically any sample size fitting under the microscope. The principle of exchanging atmospheric gases to either Ar or He (or any other gas) is crucial, as the presence of the former severely disturbs plasma conditions and creates a multitude of isobaric interferences. However, it was already shown, that the use of an aerosol entrainment device is indispensable for complete sampling of the laser generated aerosol. But independence from airtight ablation cells has proved very convenient in practical terms. Current investigations may lead to LA analysis in absence of an ablation cell using a gas exchange device (GED) for online exchange of ambient gases to Ar or He, as reported by Kovacs et al. [94] using an open tube and Tabersky et al. [95] using a plume entrainment device (Manta).

d) Mobile ablation

   The use of small, mobile laser ablation unit with glass-fiber optics and an aerosol pump allows collecting the laser generated aerosol on a filter for subsequent analysis in the laboratory. Such a system is very mobile and can be used anywhere, provided access to electrical power [213].

Further improvements of data quality can be achieved by implementing video recording during the LA of line scans in order to improve data quality, as for example unwanted sample features (pores, holes, gaps, dust) can be detected during and after analysis. Moreover, there are several matters that may be addressed in the near future to augment capacity of STALQUANT regarding various LA-ICP-MS applications.

a) Implement a spike filter with user defined parameters

b) Enable selection of several LA intervals per data file for more accurate selection of signals and allowing to mark 'LA off' intervals, e.g. when scanned over gaps on a damaged sample surface

c) Integration of laser logs (coordinates of the sample stage, laser on/off) with the ICP-MS raw data for automated location based assembling of the obtained concentrations onto an photograph of the analyzed sample surface, as reported by Paul et al. [153]

d) Include means of uncertainty assessment for bulk analysis as well as for each data point in BORE analysis

e) Include means of multivariate data analysis as a first step towards successful interpretation of the large amounts of results

10 Appendix

10.1Appendix A: technical drawing LDHCLAC

Technical drawing of the low dispersion high capacity laser ablation cell (LDHCLAC)

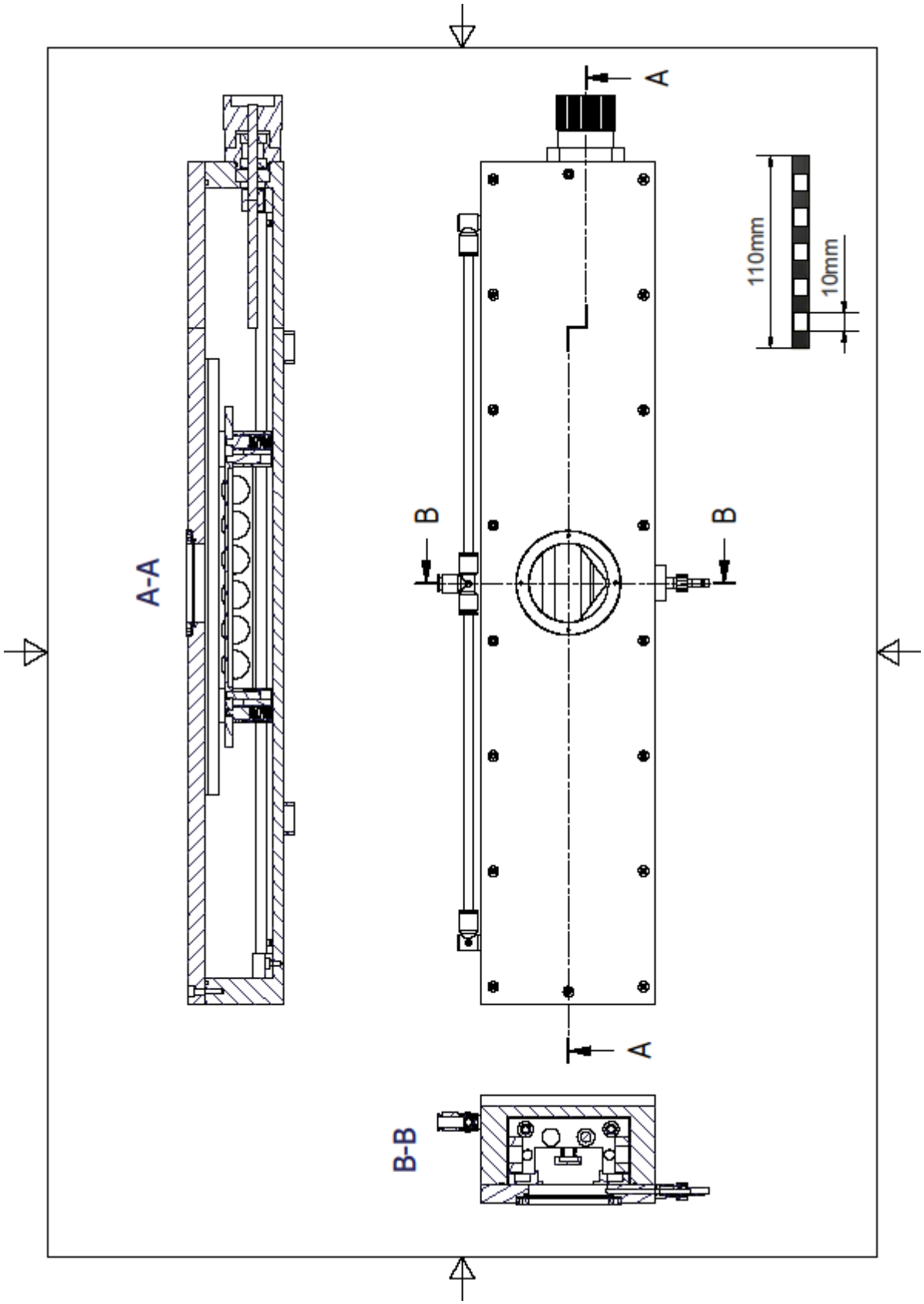

10.2 Appendix B: LDHCL ablation cell manual

User manual for
The LDHCL-ablation cell

Manual Version 1.0

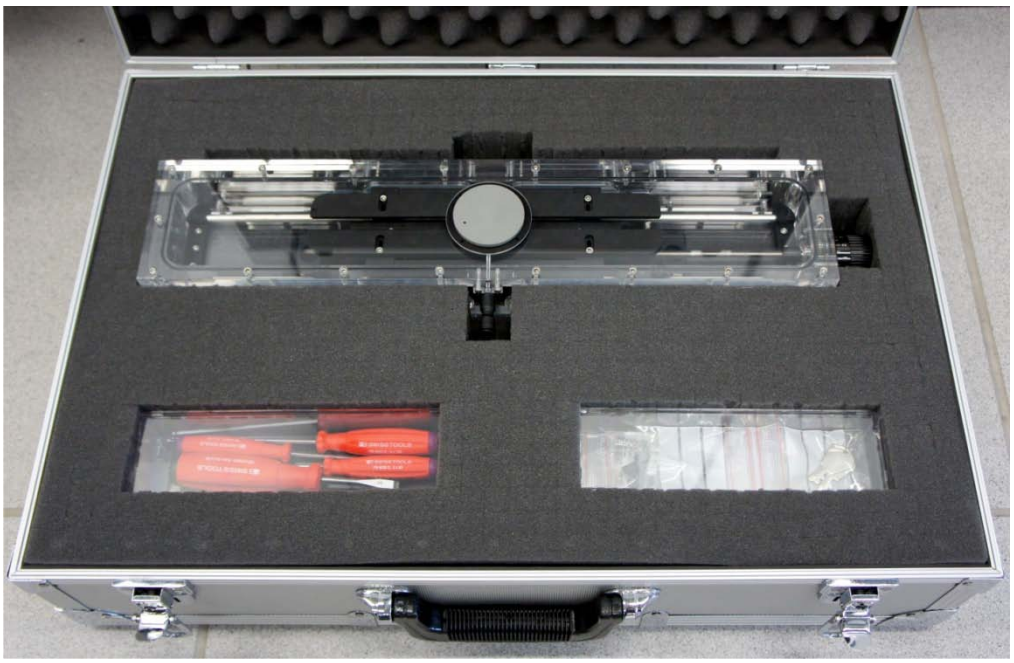

Trace Element and
Micro Analysis

ETH
Eidgenössische Technische Hochschule Zürich
Swiss Federal Institute of Technology Zurich

By Mattias B. Fricker

March 2011

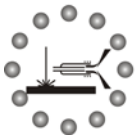

Trace Element and Micro Analysis

Prof. Dr. Detlef Günther

ETH Zurich
Department of Chemistry and Applied Biosciences
Laboratory of Inorganic Chemistry
HCI G 113
Wolfgang-Pauli-Str. 10
8093 Zurich
Switzerland
http://www.guenther.ethz.ch/

ETH

Eidgenössische Technische Hochschule Zürich
Swiss Federal Institute of Technology Zurich

Table of Contents

1. About this manual

This manual describes scope of supply, operation and maintenance of the low dispersion high capacity laser ablation cell (LDHCLAC).

The terms *cell* or *ablation cell* used in this manual refer to the low dispersion high capacity laser ablation cell.

This ablation cell is intended for use with an excimer (193 nm) laser ablation (LA) system, a computer controlled xyz-stage and any available detection system like Inductively Coupled Plasma-Mass Spectrometry (ICP-MS).

Registered trademarks used in this manual are exerted for identification purposes and remain property of their owner.

This ablation cell was developed at ETH Zurich as part of a doctoral thesis.

ETH Zurich and all persons involved in developing, building, characterizing, improving, and using this ablation cell and manual are gratefully thanked, especially Roland Mäder from ETH Zurich workshop.

2. Parts and tools

Following items are shipped with the ablation cell:

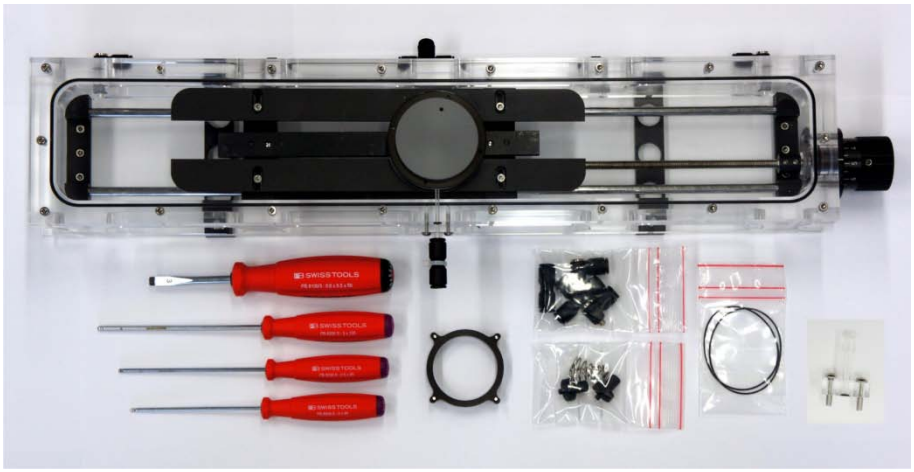

- Aluminum carrying case
- Cell body including sample sled and cover plate with UV-transparent window
- Window protector
- Tools
  - Allen key ® 2 mm
  - Allen key ® 2.5 mm
  - Allen key ® 3 mm
  - #3 screwdriver
  - Window exchange tool
- Spare parts
  - Legris ® gas tube connectors
    - 2-way connector, 6 mm
    - 3-way T-connector, 6 mm
    - Screw-on connector, 6 mm, 2 pieces
  - 2 O-ring seals for window
  - 2 springs for sample support
  - 2 long bolts for sample support, for use with thin samples
  - Extra carrier gas outlet with O-ring

3. Description and requirements

3.1. Overview

This ablation cell is intended for performing analyses with a laser ablation system coupled to an inductively coupled plasma mass spectrometer or any other suitable detection system. The UV-transparent window and the short distance between window and sample surface are designed for use with an excimer laser and Schwarzschild objective, but other laser ablation systems capable of handling the dimensions of this cell may be utilized as well. Due to the characteristic performance of this ablation cell it is possible to perform qualitative and quantitative analysis of main and trace element components at tens of µm range by single hole drilling, line scanning and sample mapping/imaging.

3.2. Materials and spare parts

The cell body is milled from a single Polymethylmethacrylate (PMMA) block and is supplied with a PMMA cover plate for enclosing the samples in an airtight system. The sled, sample support, sample holders and other parts are made of black anodized aluminum. The sled bars and sample support pins are made of stainless steel. Do not use grease in the system and do not use aggressive chemicals for cleaning. Custom manufactured spare parts can be ordered from the contact given in chapter 6, while commercial spare parts can be ordered from their producer directly.

- Gas adaptors, http://www.legris.com
- O-rings, http://www.johannsen-ag.ch
    - Ø 48 x 1 mm, window
    - Ø 329 x 2 mm, body
    - Ø 3 x 1 mm, gas outlet

3.3. Window

The window supplied with the ablation cell (diameter 2 inches, thickness 0.4 mm) is anti-reflection coated for 0° incident angle of a 193 nm laser source and allows operation with any 193 nm laser system, provided that the energy density at the window position is below the ablation threshold of quartz. This applies specifically to GeoLas laser ablation units. The window can be exchanged (chapter 5.3) if broken or damaged and represents the most fragile part of this ablation cell. Keep the window protector on the window at all times except during analysis.

3.4. Sample sled

The sample sled can take up samples of dimensions up to 230mm×34mm×16mm (L×W×D). One large or several small samples (and external standards) can be placed on the sample sled. For very small samples (e.g. rice grains) it is advised to manufacture a sample carrier with the abovementioned dimensions that has small bulges for placing the samples (e.g. rice). A flat surface of the sample is required for optimal gas flow conditions and rapid washout of the laser generated aerosol. A pair of springs presses the sample support from below against the sample holders to secure sample position at an ideal distance to the window. For thin samples (e.g. microscope glass slides) the sample support needs to be adjusted with long bolts as described in the maintenance chapter (chapter 5.2) otherwise the sample cannot be placed properly.

3.5. Gas tubes

The ablation cell must be connected to a carrier gas source, capable to deliver a constant gas flow rate. The gas outlet must be connected to the injector of the plasma torch of the ICP-MS. All gas connections require tubes with 4/6 mm (inner/outer diameter). As short as possible tubing and gas tight material is recommended.

3.6. Handle

The cell window allows performing LA on a length of 40 mm on the samples. The sled can be moved manually with the external handle to sequentially access the entire sample length.

3.7. Stage mount

Adjustable brackets with ball plungers on the bottom of the cell allow rigid mounting on a range of xyz-stages.

3.8. Legris adaptors

For the correct handling of Legris adaptors with the gas tubes, the user is referred to the Legris website: http://www.legris.com

4. Operation

For safety of the window, keep the window protector on at all times except for measurements.

4.1. Preparation of the cell for analysis

1. Remove cover plate
2. Mount samples (in sample carrier, not supplied) on sample support
3. Insert this package into the sample sled
4. Adjust sample holders
5. **Warning:** Irrespective of sample morphology, it is important to fill gaps around samples in a way that the contour resembles a block with dimensions 250mm×34mm×16mm (L×W×D). Only with such configuration the optimal gas flow conditions (according to specifications) are achieved. Placing several pieces of rock randomly on the sample support will result in uncharacterized gas flow conditions around the sample
6. Ensure that O-ring is not damaged and properly aligned in the groove
7. Place cover plate onto cell

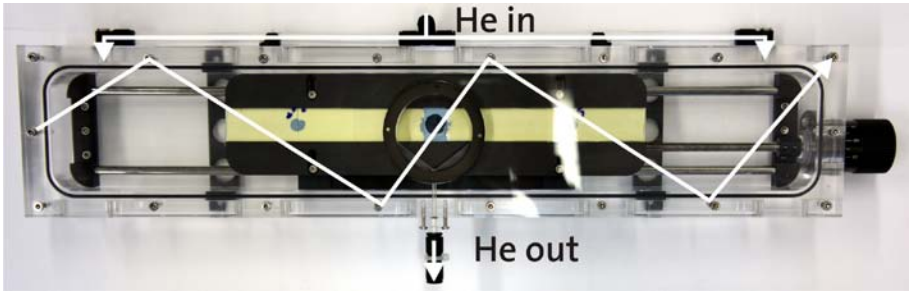

8. Tighten all screws in a random fashion (note: do not start on one end and go around tightening the screws, it will produce leaks)
9. Connect He (or Ar) gas inlet and turn on gas flow (1-2 L/min)
10. Let the cell flush for 5 minutes
11. Connect gas outlet to torch injector
12. Reduce gas flow to 0-0.1 L/min
13. Start plasma
14. Set gas flow slowly to 1.0 L/min

15. Leave for 1 hour (warm up of plasma and removing ambient gases from the cell)
16. The ablation cell is now ready for analysis

4.2. Analysis

Analyses are performed in the same way as with other ablation cells, with the only difference that between analyses the sample sled can be moved manually in order to sequentially place the entire sample under the cell window. Best results are obtained with the sample holders and sample furthest away from outlet while ablating close to the outlet, leaving 2 mm between ablation spot and sample holder.

4.3. Applications

Using this ablation cell allows a number of qualitative as well as quantitative analysis modes such as bulk analyses, line scanning, and imaging on one large or several small samples. In this way, the cell can be used for analysis of many samples without opening it between analyses and therefore reduces plasma interruption. Any solid sample or fluid inclusions with abovementioned maximum dimensions can be analyzed. An attempt to provide a complete list is not made and is delegated to the imagination of the user.

5. Maintenance

5.1. Adjusting the stage mount

Adjustable bars at the bottom of the cell allow fixing it onto the xyz-stage rigidly. This avoids accidental movement of the cell during analysis.

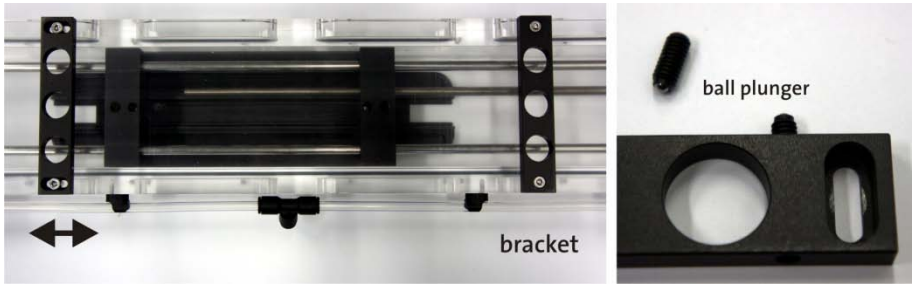

- **Required tools**

Allen key ® 3 mm
Allen key ® 2 mm

- **Procedure**

1. Remove cover plate
2. Turn cell upside down
3. One of the two stage brackets is equipped with slots for sliding to the desired position using a 3 mm Allen key ®
4. Inside of this bracket position of the two ball plungers can be adjusted using a 2 mm Allen key ®. Correct position of these locks the cell properly onto the xyz-stage

5.2. Adjusting sample support for thin samples

For analysis of thin samples the sample support has to be adjusted, or a spacer block (not supplied) can be placed between sample support and sample.

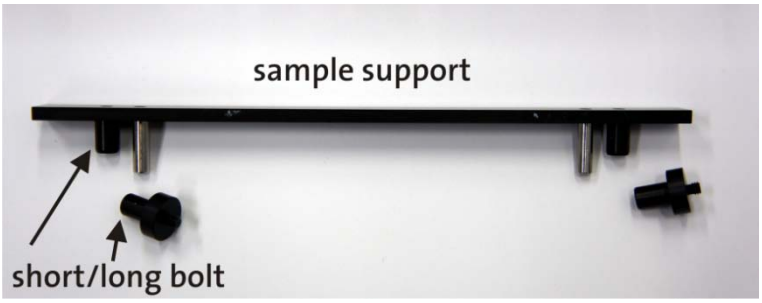

- **Required tools**

None

- **Procedure**

1. Remove cover plate of the cell
2. Remove sample support from sled
3. Remove the two short bolts
4. Place the two long bolt
5. Put sample support back onto the sled

5.3. Exchanging the window

In case of stained or damaged window, it can be cleaned or replaced.

- **Required tools**

Window exchange tool
Gloves

- **Procedure**

1. Remove cover plate of the cell
2. Wear gloves to avoid contamination on the window
3. Use the window exchange tool to unscrew the window lock
4. Remove damaged or stained window carefully
5. Ensure that both O-rings (one in the cover plate and one on the window lock) are undamaged and placed properly in the groove
6. Window can be cleaned gently with sparse organic solvent (e.g. Ethanol) and dust-free optical grade tissue
7. Put replacement window meticulously back in place
8. Put the window lock back onto the window and carefully tighten it with the window exchange tool

5.4. Disassembling for cleaning

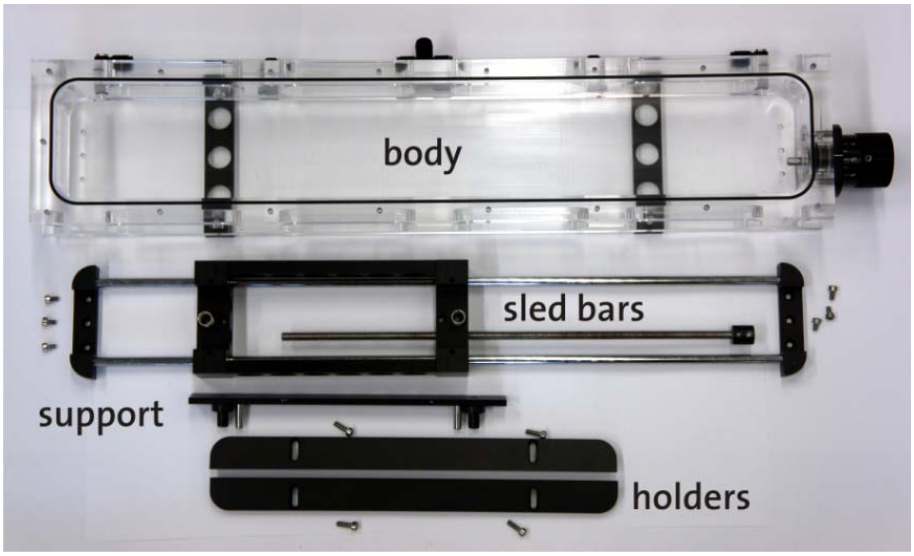

- **Required tools**

Allen key ® 2 mm
Allen key ® 2.5 mm

- **Procedure**

1. Remove cover plate from cell
2. Move sled to center position
3. Remove sample support and sample holders from sled
4. Unlock the axle joint using a 2 mm Allen key ®

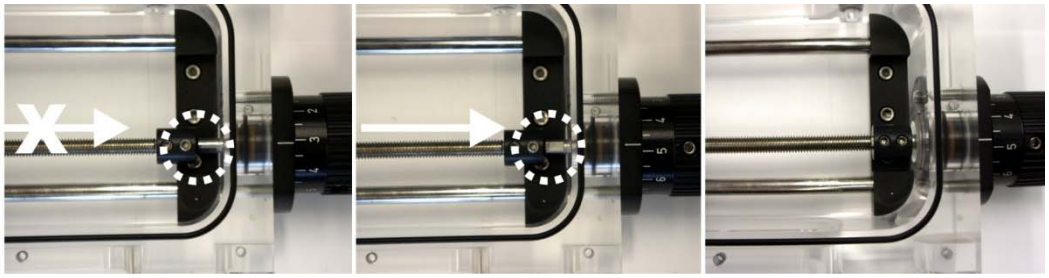

5. Gently slide sled and axle away from handle. **Warning:** Never remove handle and axle from the gastight axle seal
6. With 2.5 mm Allen key ® remove the 6 screws attaching the sled bars to the body
7. Carefully remove sled bars with sled from the body, exert special care not to damage the axle seal.
8. The cell body and parts can be cleaned with sparse Ethanol (never use Acetone) and optical grade tissue

9. For reassembling place sled bars back into the cell and attach it with the 6 screws
10. Turn handle until flat side of the axle is facing upward
11. Carefully slide back the sled until axle is inside the axle joint, lock the screw
12. Put back sample support and affix the sample holders back onto the sled

5.5. Exchanging gas outlet connector

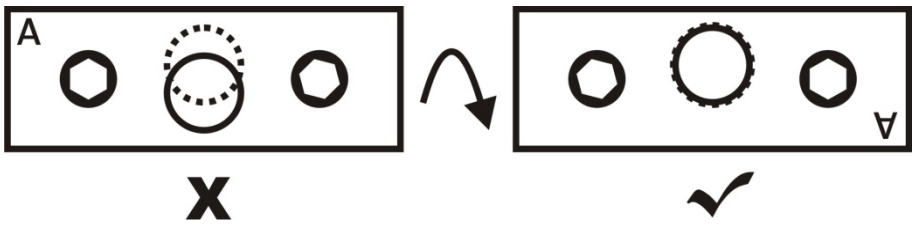

- **Required tools**

Allen key ® 2 mm

- **Procedure**

1. Remove gas outlet connector from cover plate with 2 mm Allen key ®
2. Correct placement of the connector is important for optimal gas flows and illustrated in the Figure where the gas flow path matching exactly in the configuration on the right hand side (dashed and solid circle in the center)
3. Attach connector

6. Contact

For ordering spare parts or other inquiries please contact Dr. Bodo Hattendorf via email.

Dr. Bodo Hattendorf

ETH Zurich
Department of Chemistry and Applied Biosciences
Laboratory of Inorganic Chemistry
HCI G 105
Wolfgang-Pauli-Str. 10
8093 Zurich
Switzerland
bodo@inorg.chem.ethz.ch

10.3 Appendix C: STALQUANT manual

ETH
Eidgenössische Technische Hochschule Zürich
Swiss Federal Institute of Technology Zurich

Trace Element and
Micro Analysis

User manual for

STALQUANT

Data quantification software for LA-ICP-MS bulk and imaging analysis

Manual Version 4

Program concept
and user manual by
Mattias B. Fricker

Python code by
Thomas Philippe

June 2012

Group of
Prof. Dr. Detlef Günther

Trace Element and Micro Analysis

ETH Zurich
Department of Chemistry and Applied Biosciences
Laboratory of Inorganic Chemistry
HCI G 113
Wolfgang-Pauli-Str. 10
8093 Zurich
Switzerland
http://www.guenther.ethz.ch/

ETH
Eidgenössische Technische Hochschule Zürich
Swiss Federal Institute of Technology Zurich

Table of Contents

1. About this manual

This manual describes scope, use, structure and formulas of STALQUANT data reduction for LA-ICP-MS.

Use STALQUANT is intended for reduction of transient signal data acquired by laser ablation (LA) system coupled to Inductively Coupled Plasma-Mass Spectrometry (ICP-MS). Rawdata from four ICPMS manufacturer models (PE ELAN 6x00, Agilent 7500, Spectro MS, ~~Thermo element2~~) are supported. STALQUANT was specifically developed to quantify rawdata and assemble line scans or mapping, furthermore it can also be used for bulk analysis (single hole drilling or line scans). It was designed for rapidly quantifying the large amounts of data acquired with the low dispersion high capacity laser ablation cell (LDHCLAC [1]), however use of this program is not limited by the ablation cell utilized.

Registered trademarks used in this manual are exerted for identification purposes and remain property of their owner.

For a quick start using this program go to page 144. Calculations and formulas are discussed in detail starting from page 155, chapter 6.

This program was developed at ETH Zurich as part of the author's doctoral thesis and the Python code was written by Thomas Philippe.

ETH Zurich and all persons involved in developing, testing, improving, and using this program and manual are gratefully acknowledged, especially Daniel Tabersky and Dr. Sebastian Breitenbach for working out functions and calculations and continuously contributing to the progress, and Steffen Allner for the Windows-port.

2. System and requirements

This program is written using the Python programming language, which runs in several operating systems, using appropriate Python interpreters. The current version was optimized to run in Linux, Mac OS and MS Windows after installing the required packages and libraries. Using modern hardware will significantly increase swiftness of displaying the plots, however it runs on most types of hardware.

Linux installation:

- Install Python 2.6 (Python 3.0 not preferred)
- Install packages
  - numpy
  - scitools (scipy)
  - wxpython
  - matplotlib
  - matplotlib-data
- Extract the zipped folder containing all STALQUANT files into a directory of your choice

Windows installation:

- Download a Python distribution for MS Windows, e.g. from http://enthought.com/repo/free/
- Install interpreter
- Extract the zipped folder containing all STALQUANT files into a directory of your choice

Mac OS X installation:

- Download a Python distribution for Mac OS, e.g. from http://enthought.com/repo/free/
- Install interpreter
- Extract the zipped folder containing all STALQUANT files into a directory of your choice

3. Introduction

3.1. Overview

The quantification protocol is entirely based on calculations reported by Longerich et al. 1996 [2] and maintains many useful features of LAMTRACE [3], such as linear interpolation between external standards as instrumental drift correction, etc. However the following crucial features are not limited using STALQUANT:

a) Number of data files in a series

b) Number of series calculated simultaneously

c) Number of isotopes monitored by the MS

d) Number of data points per file

e) Different IS elements possible for the data files within a series

External standard acquisition at the beginning and at the end of a series are mandatory for successful quantification using STALQUANT, however, the program considers additional external standard acquisition at any position within a series as long as they are acquired in pairs. Moreover it allows assigning quality control measurements (i.e. a well known reference material for validation) within a series.

3.2. Principle

Major attributes for this software are a simple user interface and easy data handling as well as increased efficiency in data reduction and thereby reducing user errors. With the easily operated graphical user interface, handling STALQUANT follows a straightforward procedure:

a) import rawdata

b) set parameters

c) save project

d) calculate

e) export results

3.3. Capability

After development of a large LA cell (LDHCLAC [1]) in our labs, it became feasible to analyze large samples. Performing a large number of short line scans across the entire surface yields the trace element profile of a sample while parallel line scans can be used for mapping element distribution of the sample surface. Nonetheless, assembling all these short line scans is tedious, time consuming and a tremendous source of user errors. Consequently STALQUANT was initially developed for rapid quantification of such type of analyses. However, it swiftly handles also other applications, such as bulk analysis of solid samples.

STALQUANT works with transient signals obtained from homogenous as well as heterogeneous samples to quantify the bulk or 'data point per data point' (BORE) and assemble the results to yield a profile or map across a heterogeneous sample. The output files provide the user with the freedom to use a program of his choice for further calculations, plotting and presenting the results.

On the other hand, STALQUANT was not designed for quantification of Fluid Inclusion nor dating, for such data analysis, the user is referred to SILLS and GLITTER, UPb.age (or others) respectively, nine of such programs are summarized in [4].

4. Using STALQUANT

4.1. Launch the program (Linux)

1. Open a terminal shell
2. Switch to the folder where STALQUANT is installed
   Type `cd Desktop/stalquant3`↵
3. Type `python main.py` ↵

4.2. Launch the program (MS Windows)

1. Switch to the folder where STALQUANT is installed
2. Double click the file `main.py`

4.3. Launch the program (Mac OS X)

1. Switch to the folder where STALQUANT is installed
2. Double click the file `main.py`

4.4. Menus

A previously saved project may be opened instead of starting a new project, using the menu button **open** and selecting a zipped project folder.

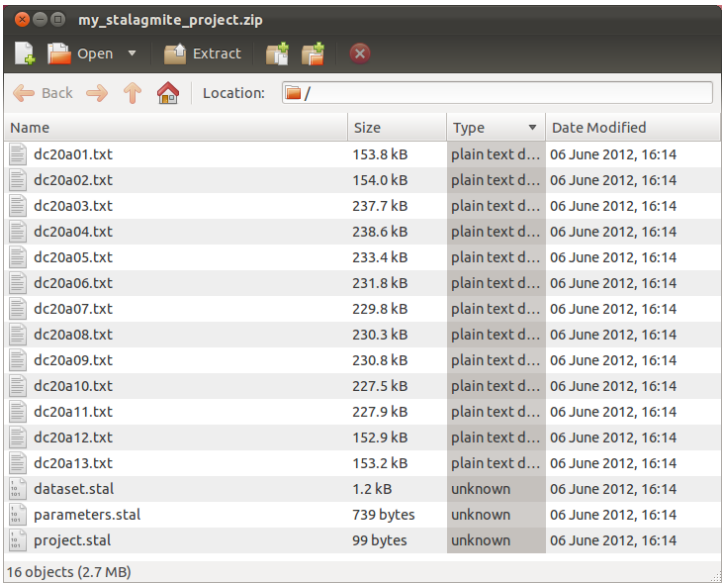

A project may be saved at any time by clicking the button **save**  , creating a zipped folder containing all imported rawdata files and all user input.

a) `dataset.stal` (everything entered in the **initialization** tab)

b) `project.stal`

c) all of the imported rawdata textfiles (listed in the **initialization** tab)

d) `parameters.stal` (everything entered in the **parameters** tab)

Important: no output data (results) at all are saved in the project. For saving results, they must be exported using commands in the **processing** tab, see page 149.

Exiting the project by clicking the button **exit**  prompts whether to save the project or discard. By exiting the project, STALQUANT is reset and ready for another set of rawdata. To quit STALQUANT close the window or click **File - Quit**. Clicking the window close button  results in immediate loss of all data that were not saved.

4.5. Starting a new project

The program comprises four tabs, to be followed from left to right in a comprehensive manner. Furthermore these tabs comprise frames to be followed from left to right.

4.5.1. The Parameters tab

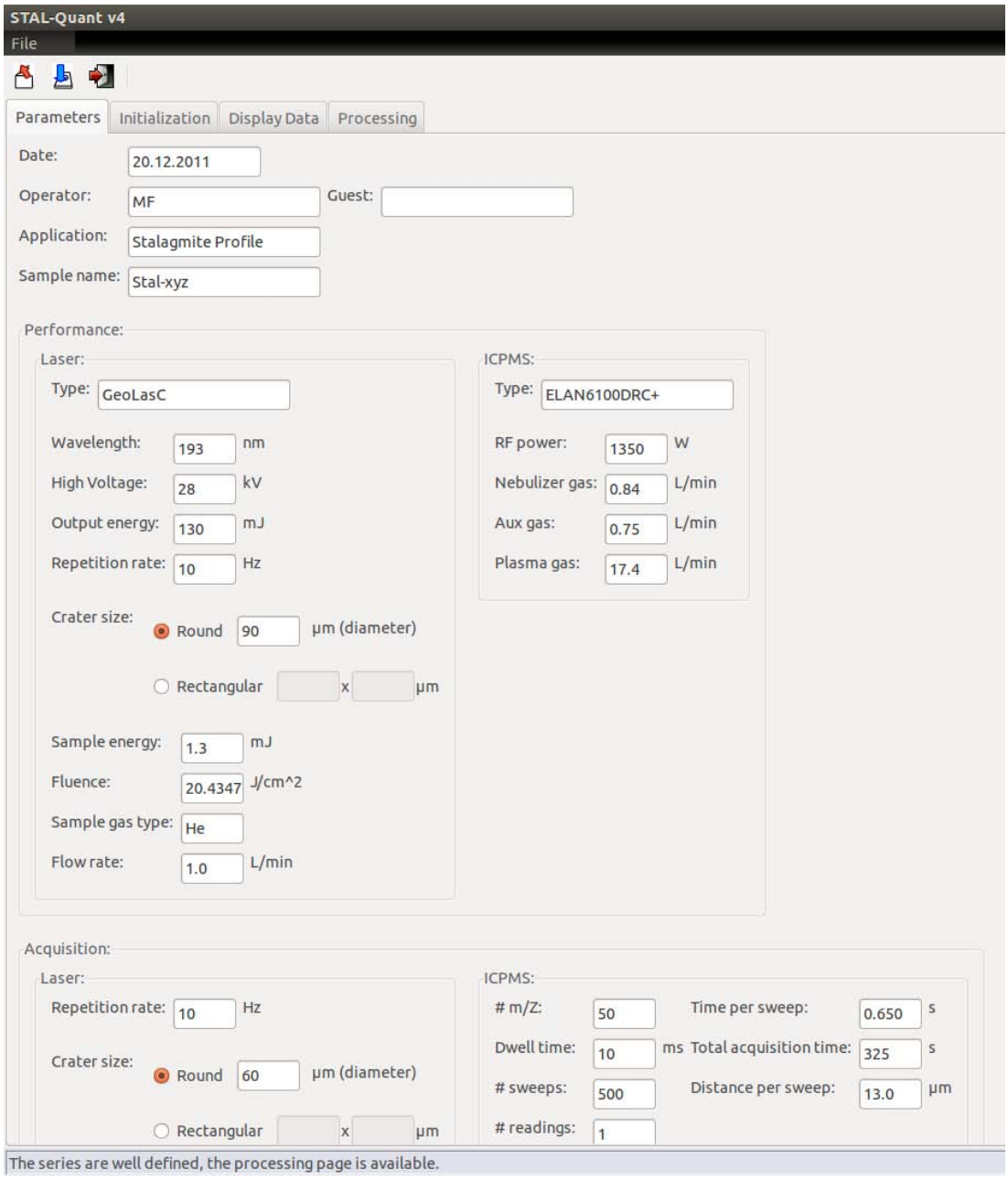

Enter detailed information like performance and acquisition parameters of the laser and the ICP-MS. All information given here will

be saved together when saving the project and exporting the output. Empty fields in this tab are ignored when advancing further through the tabs.

Please consider these facts:

- The **fluence** is calculated (Equation 5, Equation 6) instantaneously from the **crater size** and **sample energy**.
- The **distance per sweep** is calculated (Equation 2) instantaneously from **scanning speed** and **time per sweep**. Furthermore this calculated value is used later on for the conversion of time-domain data to distance-domain, where required.
- **Dwell time** must be given, in case the LOD are to be estimated via Poisson statistics. The dwell time given here is set as default for all *m/Z*. Assigning isotope-specific dwell times is possible in the **processing** tab when clicking on **Poisson**.

4.5.2. The Initialization tab

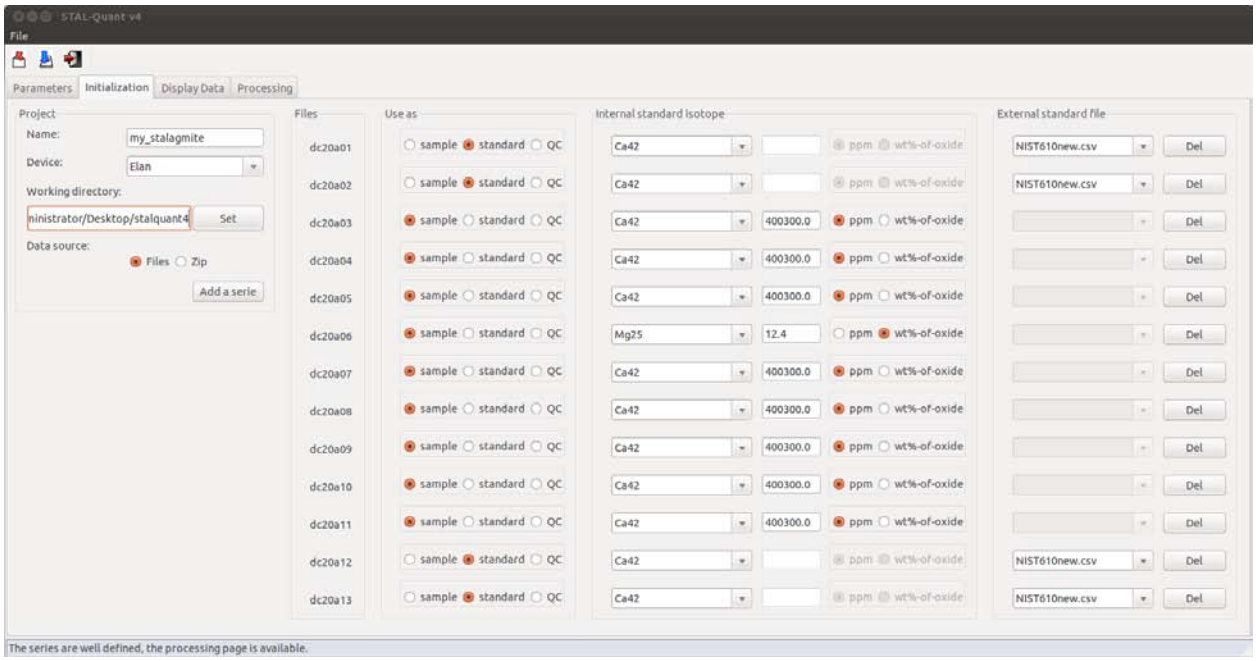

Enter project name, it appears later as part of the file name of a saved project and output results.
Do NOT use spaces nor mutated vowels, e.g. ä, ö, ü in project name!

Choose **device** (currently supported: Agilent 7500, PE ELAN6x00, Spectro MS).

Select **working directory**.

Choose **data source** File or Zip (Agilent data: all subfolders can be zipped and the zip-file can be transferred from the lab to the data reduction software for analyzing data without extraction).

Click **add a series**.

Use the cursor and holding *shift* or *ctrl*, to highlight all files to be added to the current project, highlight only those files required for analysis. With filenames according to Longerich et al. 1996 [2], it is possible to add multiple such series. On the other hand a series may comprise more than 20 datafiles. Rawdata files from ELAN6x00 can be imported directly without renaming of the `*.xl` suffix, `*.txt` suffix works as well. It is possible to import several series, furthermore it is possible to import stepwise series from multiple instruments for simultaneous calculations (provided each of the series include their own set of external standard measurements).

Wait a few seconds.

Four frames with your data and parameters appear.

Data files are alphanumerically ordered upon import (in case rawdata were not acquired using consecutive filenames, they must be changed prior to importing data). After successful import of the datafiles, unwanted files can be removed by clicking the **Del** button

By default the first two and last two files are set to **standard**, while **standard** refers to external standard used for quantification and instrument drift correction. All others are set to **samples** by default. Additional **standards** between the first two and last two files can be selected, however the **standards** must appear in pairs and constitute the first two and the last two of a series. A series can be subdivided with pairs of **standards**. Multiple series may be imported and calculated at once.

In case other external standards were analyzed as samples, they need to be marked **QC** (quality control). All **QC** are considered for **bulkquant** but are ignored for **cpsprofile**, **BOREquant** and **BOREquant100%norm** (see chapter 4.5.4).

Internal standard element may vary for the **samples** within a series, the selection of internal standard (IS) element for the external standards determines the internal standard applied for the calculations of the external standard (ES). For the quantification of a sample with a selected IS, the same IS for the ES is automatically used for calculations. Therefore it is possible to calculate different samples with different internal standards, while the same external standards are employed.

Concentration values can be entered individually (must be followed by ↵) or applied to all, as well as the units. The unit wt% refers to the oxide of the element. STALQUANT converts all units to µm/g before calculations.

External standard type must be the identical for a series, however it may differ between series. See chapter 5.1 for importing your own external standard reference values.

4.5.3. The display data tab

Choose isotopes to be plotted for selecting intervals of background and signal. Marking and unmarking isotope changes the line color in the plot. Isotope ratios can be plotted by clicking **add ratio** and selecting the two desired isotopes for the ratio. The number of ratios added to the plot is not limited, however ratios are not saved, when saving the project or exporting the output.

By moving the cursor onto the plot, a vertical bar appears in order to assist selecting proper intervals. Clicking onto the plot (or double-clicking into the table row) selects intervals in this order

1. **BG Start**
2. **BG End**
3. **SG Start**
4. **SG End**

Caution: by clicking onto a curve the click is not registered, take care clicking anywhere on the vertical line but not on a data line (curve)! The following two conditions for the time values must be considered: **BG Start**<**BG End** and **SG Start**<**SG End**.

For changing a single value, it can be activated in the frame **intervals** and then clicked on the plot or double-clicked in the table **raw data**.

Likewise it is possible to enter numerical values for selecting intervals, entering a digit must be followed by ↵ . From an entered numeral the program selects automatically the closest data point (no need to enter all decimals).

The third way of selecting intervals is by double clicking on the corresponding row in the table of the **raw data**.

After intervals for one file are selected, click on the next one in the frame **files** and repeat selecting intervals, or click **apply to all** in the **intervals** frame in the case that all data files use the same intervals.

By clicking **Add ratio**, the user can add unlimited ratios of his choice to the plot, on the secondary axis. Ratios appear in the **isotopes** list and can be shown and hidden like isotopes.

4.5.4. The processing tab

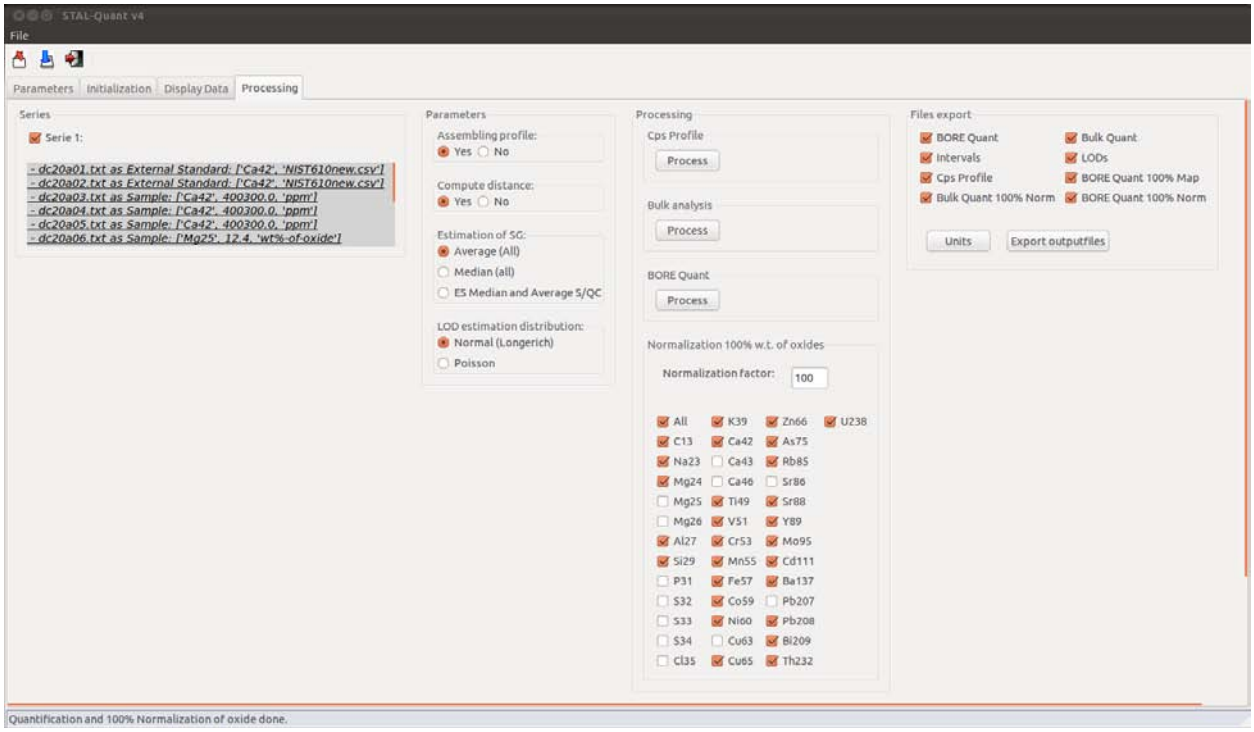

Proceed from left to right.

First select the **series** to be processed. Marking one series will mark automatically all series with the same element menu. Undesired marked series can be unmarked. For the case of two or more series

present with different element menus, only one (or all of those having equal element menus) can be marked and processed. To process the first set, complete all of the steps below, finishing with **export output files**. Then return to the **series** frame, unmark it, then mark the next one. Again complete all of the steps below, save output files using a different filename.

Select **yes** or **no** for assembling profiles. **Yes** assembles all BORE results in alphanumerical order given in the **initialization** tab. **No** creates BORE results separately. For the case **no** is selected, the cpsprofile and all BORE results are reported with distance axis (converted from time, see chapter 6).

No spike correction to the signal is applied in this version of the program.

Spikes in rawdata can be overcome by using median (more robust with outliers) instead of average for the calculations.

However, because median is not useful when analyzing heterogeneous samples, three options are available for using proper estimation of SG intervals (for BG intervals average is used, median is not available).

a) **Average (all)** uses average only for all calculations, careful selection of intervals is necessary.

b) **Median (all)** uses median only for all calculations, useful only for analysis of homogeneous samples with stable signals and allows only bulk quantification.

c) **Median ES/average Sample** is used for analyzing line scans on heterogeneous samples having spikes during externals standards acquisition, but no spikes during sample acquisition.

The user is offered a selection of three types of LOD estimation. Due to the ongoing discussion in the literature on the use of Poisson statistics for low BG counts, it is possible to do LOD estimation based on Poisson statistics. Details are given in chapter 6.

a) **Normal (Longerich)** as published by Longerich et al. [2]

b) **Poisson** derived from oral comm. Martin Tanner 2012 and Currie 1995 [5] considering Poisson distribution for low BG counts, which is valid for both low and high counts.

Clicking **process** in **Cps Profile** calculates point per point background subtracted intensities when line scans were acquired. Assembled or not assembled depending on the selection made above.

In the list *normalization to 100% w.t. of the oxides*, mark all of the isotopes to be included (i.e. unmarking those to be excluded, such as nonmetals). Only one isotope per element may be included in 100% normalization. Clusters are neglected from this list, as they must not be included in the 100% normalization. The default value, set to 100 %, can be changed by entering the desired value. A proper selection here is required to continue with **Bulk analysis** and **BORE Quant**, if normalization to 100 wt% is not desired, unmark **Bulk Quant 100% Norm**, **BORE Quan 100% Map** and **BORE Quant 100% Norm** before **exporting the outputfiles** (see below).

Clicking **process** in **Bulk Analysis** calculates average (or median) concentrations.

Clicking **process** in **BORE Quant** calculates point per point quantification, when line scans were acquired and BORE results are desired.

In the **file export** frame, mark all of the results files to be written in the output, select results **units** for each isotope (wt% of oxide or ppm) in the report and press **export output files**.

A zipped file containing all of the marked results files (comma separated) is created.

a) `bulkquant.csv:` quantified averages (or median) as in LAMTRACE.

b) `bulkquant100.csv:` like bulkquant additionally normalized to 100% w.t. of oxides.

c) `intervals.csv:` List of integration intervals, BG and SG duration, number of datapoints of BG and SG.

d) `LODs.csv:` List of limits of detection for Bulk and BORE (for formulas see **Equation 3**, page 159), BG average, BG standard deviation, SG average (or median), SG standard deviation, BG subtracted SG, RSD of SG, sensitivity, and abundance normalized sensitivity, coefficients *a* and *b* of the linear regression.

e) `cpsprofile.csv:` Background corrected intensities (each data point of signal interval).

f) `borequant.csv:` quantified each data point (as BORE in LAMTRACE).

g) `borequant100.csv:` like borequant additionally normalized to 100% w.t. of oxides.

h) `borequant100map.csv:` like borequant100, sorted per element instead of data file, i.e. ready for creating surface plots.

i) `parameters.csv:` all information on instrumental parameters entered in the **parameters** tab are saved in this file.

j) constant data: `conversion.csv`, `abundance.csv`, `external standard.csv,` all constant data values used for the calculations are saved with the output files.

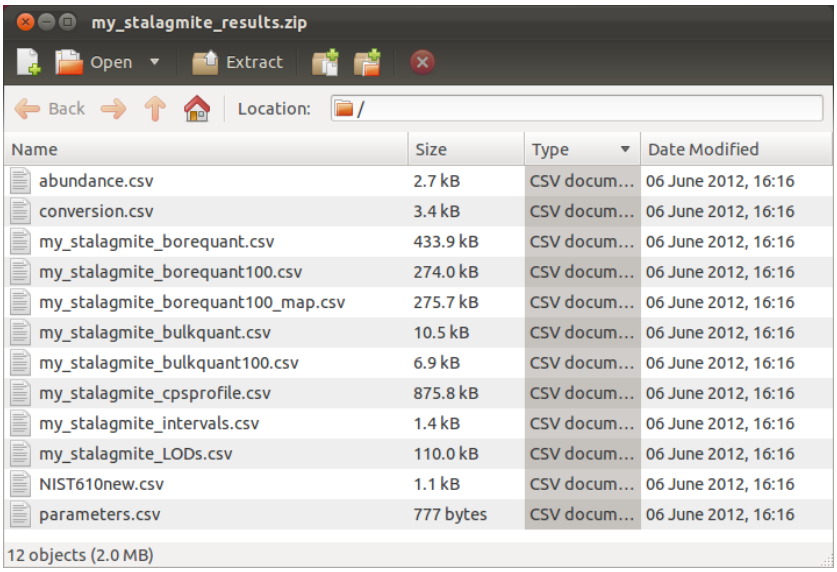

The results files are now subject to the user's choice of plotting software for visualization and assembling the line scans to create images/maps rather than a 2D profile or further statistical data analysis.

5. Customizing STALQUANT

5.1. Import external standard reference values

Go to the subfolder `<stalquantfolder>/constant_data/ext_std/` found in the working directory of the program. Any files placed here will appear in the context menu **external standard type** in the **initialization** tab after restart of STALQUANT. Your own external standard reference value files must have the same format as the default files in order to run properly (element names without oxygen). See page 161 about errors concerning this topic.

5.2. Update constant data

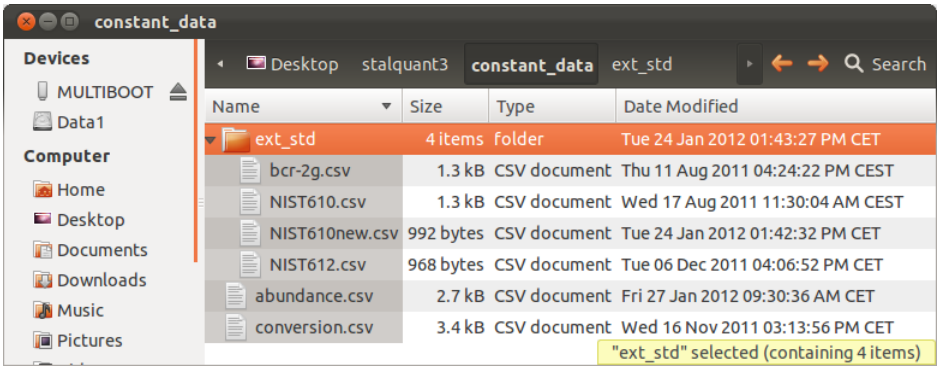

Isotopic abundances for the abundance correction are taken from LAMTRACE 2.16 and listed in the file `abundance.csv`. Conversion factors for transferring ppm of metal values to wt% of oxides and vice versa are taken from LAMTRACE 2.16 and listed in the file `conversion.csv` including stoichiometry of the oxides

6. Calculations and formulas

All calculations throughout the program are performed using cps and µg g^{-1} units, i.e. ppm, except for the normalization to 100% of oxides, for which the concentrations are converted. Internal standard values inserted in wt% of oxides by the user are converted to µg g^{-1} prior to calculations, as well as reference values for the external standards given in wt % of oxides. For the two results files `borequant100.csv` and `borequant100map.csv` the units are converted to wt % of the oxides and also reported in the output file using wt % of the oxides.

Some of the formulas in this chapter are not simplified for better understanding of their derivation.

Background subtraction

The average of the intensities in the background (BG) interval for each data file are subtracted from the average (or median) of the respective signal (SG) intensities, for background correction. Median may be used instead of average for the signals of both ES and SMP, or only ES when heterogeneous samples (imaging) are analyzed, because median is not successful with unstable signals. So far, no spike correction is implemented in STALQUANT. The background subtracted intensities are then abundance corrected (dividing it by the natural isotopic abundance and multiplied by 100) to yield element intensities.

Cpsprofile

To generate the cps profiles, the average of BG is subtracted from each data point within the SG interval and all data points outside of the SG interval are discarded. In case the option **assemble** is set to **yes**, the resulting background corrected intensities from each sample data file are assembled in alphanumerical order of the data files. In case the **assemble** option is set to **no**, all of the data files appear separately in the output file.

Series definition

There are no limits for the number of series calculated simultaneously, nor in the number of SMP and QC within a series. However practical limits as to how many series measurements acquired during a day will be routinely applied by the user. Furthermore the user is free to decide how many SMP and QC are acquired before recording the last pair ES of a series. Considerations of instrumental drift over time among others have to be taken into account and are the responsibility of the user.

$ES_a\ ES_a\ SMP_1\ SMP_2 \ldots SMP_m\ SMP_n\ ES_a\ ES_a\ SMP_x \ldots SMP_z\ ES_a\ ES_a$

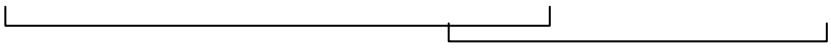

1. series 2. series

$ES_a\ ES_a\ SMP_1\ SMP_2 \ldots SMP_m\ SMP_n\ ES_a\ ES_a\ ES_b\ ES_b\ SMP_q \ldots SMP_z\ ES_b\ ES_b$

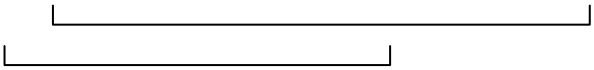

1. series 2. series

With ESa and ESb being two different external standards, and a number of SMP analyzed between two pairs of ES analyses.

Linear interpolation of sensitivity

The first two and the last two data files of a series must be external standard measurements and are necessary for successful linear interpolation (assumed linear drift) of the sample intensities. The program discovers these two pairs to proceed with calculations of that series. In case there were additional pairs of external standards measured during a series, the program will subdivide the dataset to smaller series and process them one by one automatically. Linear interpolation of sample intensities is performed in the smallest series, then quantified, after which calculations continue with the next series, and so forth. Within a series the different internal standard isotope can be chosen for all SMP, ES and QC, those specified for ES are used to calculate ES concentrations while those specified for SMP and QC are used to calculate concentrations using the same specified isotope from ES data. Furthermore the 4 external standard types of one series must be identical. The BG corrected and abundance

normalized I_X^{CAL} of all data files in a series (ES, QC, SMP) are plotted on an integer timeline to run a linear regression through the four ES values of each analyte x. The time-integer of the data file is inserted into the regression linear equation to compute the interpolated value of I_X^{CAL} which is used in the quantification equation.

Quantification

Quantification is based on formulas reported by Longerich et al., 1996 [2], i.e. identical to the formulas used with LAMTRACE [3]. Absolute element concentrations are obtained using internal and external standardization, summarized [2] below.

Equation 1

$$C_X^{SMP} = C_{IS}^{SMP} \cdot \frac{I_X^{SMP}}{I_{IS}^{SMP}} \cdot \frac{I_{IS}^{CAL}}{I_X^{CAL}} \cdot \frac{C_X^{CAL}}{C_{IS}^{CAL}}$$

- C_X^{SMP} Final result, concentration of analyte x in sample
- C_{IS}^{SMP} Concentration of internal standard in sample (obtained from independent measurements)
- I_X^{SMP} Signal of analyte x in sample (BG subtracted, abundance normalized)
- I_{IS}^{SMP} Signal of internal standard in sample (BG subtracted, abundance normalized)
- I_{IS}^{CAL} Signal of internal standard in external standard (BG subtracted, abundance normalized, linearly interpolated)
- I_X^{CAL} Signal of analyte x in external standard (BG subtracted, abundance normalized, linearly interpolated)
- C_X^{CAL} Concentration of analyte x in external standard (certificate)
- C_{IS}^{CAL} Concentration of internal standard in external standard (certificate)

For bulk quantification the BG-subtracted and abundance-normalized average (or median) signals are inserted, whereas for BORE quantification each data point of the SG (BG subtracted, abundance normalized) is quantified individually to obtain a distribution profile.

Time to distance conversion

When for assembling **no** is selected, the time domain data is converted to distance domain of the lines cans for cpsprofile and all BORE output, i.e. between each data point is the distance *d*.

Equation 2

$$d = \mathrm{v} \cdot T$$

d	Distance per sweep [µm]
v	Scanning speed [µm s^{-1}]
T	Time per sweep [s]

Limits of detection (LOD)

Limits of detection are estimated per data file and all results lower than that are blanked for `bulkquant.csv`, `bulkquant100.csv`, `borequant.csv`, `borequant100.csv` and `borequant100_map.csv`. The term for ablation yield, as used by Longerich et al. [2], is omitted, because this is regarded for by using sample sensitivity rather than sensitivity of ES.

Ongoing discussions on limits of detection (LOD) estimation considering normal distribution (ND) or Poisson distribution (PD) have lead to the incorporation of several formulas into STALQUANT and let the operator decide upon which one to use. The LOD in LA-ICP-MS is a function of the standard deviation of the background (blank) measurement and the instrument sensitivity. As it is common in LA-ICP-MS to have close to or zero backgrounds for the heavy isotopes, it is important to employ the proper statistics to estimate the standard deviation of the background. For zero or close to zero counts the standard deviation of the background follows counting statistics, i.e. Poisson distribution. The four cases for LOD estimation are listed below. The user defines whether the LODs are to be estimated using Normal or Poisson distribution. STALQUANT then uses the corresponding formula for the BULK and the BORE calculations.

The formula for ND is from Longerich et al. [2], for PD they are based on Currie [5] and personal communication with Tanner 2012.

Equation 3

	BULK	BORE
ND **Normal distribution**	$\mathrm{LOD_x} = \frac{3\sigma_{\mathrm{BG,x}}}{\mathrm{S_x}}\sqrt{\frac{1}{m}+\frac{1}{n}}$	$\mathrm{LOD_x} = \frac{3\sigma_{\mathrm{BG,x}}}{\mathrm{S_x}}$
PD **Poisson distribution**	$\mathrm{LOD_x} = \frac{3.29\cdot\sqrt{\mu_{counts,BG,x}}\cdot\frac{1}{\sqrt{n}}+2.71}{\mathrm{S_x}\cdot\mathrm{DT_x}}$	$\mathrm{LOD_x} = \frac{3.29\cdot\sqrt{\mu_{counts,BG,x}}+2.71}{\mathrm{S_x}\cdot\mathrm{DT_x}}$

$\sigma_{BG,x}$	BG standard deviation of analyte x
S_x	Average Sample Sensitivity of analyte x
n	# of data points of BG
m	# of data points of SG
$\mu_{counts,BG,x}$	$meancps_{BG}*DT_x$ (after Poisson: $\sigma^2=\mu$)

Normalization to 100% wt of oxides

For normalization of the bore results, only one Isotope per element may be included while cluster *m/Z* are ignored. First, all µg/g values are converted to wt% of the corresponding oxide. Then the concentration values of all selected istotopes of one datapoint (sweep) are multiplied by a factor to yield 100%.

Equation 4

$$C_{xt}^{N} = C_{xt}\cdot\left(\frac{\sum_{x=1}^{m/Z} C_{xt}}{100}\right)$$

C_{xt}^{N}	100% wt of oxide normalized value of analyte *x* at time *t*
C_{xt}	value of analyte *x* at time *t* before normalization
m/Z	Only for the isotopes selected for 100% normalization
x	Running variable for analyte
t	Running variable for time

Clusters formed in the ICP

Formation of clusters in the ICP is known and occasionally such *m/Z* are monitored to provide an estimate of various plasma effects. However, such *exotic m/Z* in the rawdata disturb quantification formulas and are consequently neglected from quantification.

STALQUANT supports notation in rawdata for *m/Z* generally arranged as X*** or Xx***, with X being a single capital character element symbol, Xx a two character element symbol and *** 1-3 digits of isotope mass. Cases listed below are ignored from quantification: $^{++}$Xx***, XxAa*** or single character variations thereof, e.g. XxO***, XxAr***, etc are: doubly charged-, oxide-, and argidespecies.

Calculation of the laser fluence in the parameter tab

Round crater

Equation 5

$$F = \frac{E}{1000 \cdot \pi \cdot \left(\frac{\varnothing}{2 \cdot 10000}\right)^2}$$

F	Fluence [J cm^{-2}]
E	Energy on sample [mJ]
∅	Crater diameter [µm]

Rectangular (square) crater

Equation 6

$$F = \frac{E}{1000 \cdot \frac{L}{10000} \cdot \frac{W}{10000}}$$

F	Fluence [J cm^{-2}]
E	Energy on sample [mJ]
L, W	Length and width of the crater [µm]

7. Errors

For some of the errors a message appears in a red box at the bottom of a tab explaining the problem.

As long as series are ill-defined, it is not possible to continue, i.e. ES always in pairs, and at least the first two and last two data files.

The most frequent error is caused by improper selection of intervals. Go to **display** tab and check all intervals. Accidentally clicking on a data line will not select the data point and proceeding selection will screw up interval selection.

It was reported a few times, that scrolling was not possible running STALQUANT in Windows. In that case change the size of the window, which will force the scroll bars to reappear.

In the initialization tab, be careful when using the scroll wheel of your mouse, sometimes this action will unwillingly change selection of internal standard or external standard.

At least one series must be selected to continue with processing.

Before processing **BORE Quant**, multiple isotopes of an element must be unmarked. Only one isotope per element can be normalized to 100% w.t. This step is necessary for processing all **BORE Quant**, even though it only affects **BORE Quant 100** which might not always be desired.

All of the isotopes appearing in your rawdata files must be listed in the isotope abundance table. Find the resource file `abundance.csv` in the `'stalquantfolder'/constant_data/` and add the missing isotopes without changing the layout, only insert a line where necessary. Clusters and other plasma generated exotic *m/Z*, e.g. $^{+}NaAr^{63}$, $^{++}Ba^{69}$ unnecessary to be listed in `abundance.csv`, because they are ignored for quantification. Furthermore all of the isotopes to be quantified must be listed in the external standard resource a file `nameofstandard.csv` in `'stalquantfolder'/constant_data/ext_std/` with a concentration and units.

8. Glossary and references

Frame	Specific area in a tab, see screenshots in chapter 4.5
Series	Logic group of measurements (individual rawdata files) in alphanumerical order, usually with consecutive numbering and a letter for each series [2]. This program allows analyzing multiple series at once, furthermore number of rawdatafiles is not limited
BG	Background, first ~30 s of recorded signal, before LA
SG	Signal, intensities recorded from LA on a sample
ES	External standard, certified reference material for calibration
IS	Internal standard, concentration determined prior to LA-ICP-MS by an independent method
QC	Quality control, well known reference material treated as a sample to validate calibration
SMP	Sample, measurements on an unknown
C	Concentration (ppm or wt%) of the analyte in the sample
I	Intensity (cps, counts per second), response of the analyte in the detector

References:

1. M. B. Fricker, D. Kutscher, B. Aeschlimann, J. Frommer, R. Dietiker, J. Bettmer, and D. Günther, *Int. J. of Mass Spectr.*, 2011, **307**, 39-45.
2. H. P. Longerich, S. E. Jackson, and D. Günther, *J. Anal. At. Spectrom.*, 1996, **11**, 899-904.
3. S. E. Jackson, LAMTRACE user manual, 2005, Department of Earth and Planetary Sciences, Macquarie University, Australia.
4. P. Sylvester, Ed., Laser Ablation–ICP–MS in the Earth Sciences CURRENT PRACTICES AND OUTSTANDING ISSUES, Mineralogical Association of Canada, 2008, vol. **40**.
5. L. A. Currie, *Pure and Applied Chemistry*, 1995, **67**, 1699–1723.
6. W. M. Haynes, Ed., in Atomic Masses and Abundances, CRC Handbook of Chemistry and Physics, 2012, 92nd edition.

9. Contact

For bug reports, questions, suggestions or other inquiries, please contact Mattias Fricker via email.

Mattias B. Fricker

ETH Zurich
Department of Chemistry and Applied Biosciences
Laboratory of Inorganic Chemistry
HCI G 120
Wolfgang-Pauli-Str. 10
8093 Zurich
Switzerland
mfricker@gmx.ch

10.4 Appendix D: FIJI macro

A macro for FIJI, generating map surface plots for STALQUANT map output

```
// written by Luca Flamigni and Mattias Fricker 25. April 2012
// macro to generate images from stalquant mapping output
*_map.csv
// in this case the line and column and element numbers are
chosen for // processing the mapping data. preparation of the
file 'find and
// replace' all spaces with zeros in the data (i.e. those
below LOD)
// be careful whether the file is , or ; delimited

setBatchMode(true);

// File input and reading ----------------------------------
--------

run("Clear Results");
run("Set Measurements...", "  mean redirect=None decimal=9");
dirout = getDirectory("Output directory");
text = File.openAsString("");

// Split lines and import file
lines = split(text,"\n");
text = "";

h=newArray(483);
for(i=0;i<483;i++){
     h[i]=i+1;
}

for(el=0;el<20;el++){

currentline=split(lines[30*el+2],",");
name=currentline[0];

for(i=(30*el+3);i<(30*el+29+3);i++){
     currentline=split(lines[i],",");
     for(n=0;n<483;n++){
          setResult(h[n],(i-
(30*el+3)),10000*currentline[n+1]);
```

```
     }
}
updateResults();

newImage("Untitled", "16-bit Black", 483, 29, 1);

for(i=0;i<29;i++){
     for(n=0;n<483;n++){
          setPixel(n, i, getResult(h[n],i));
     }
}

run("Flip Vertically");
run("Enhance Contrast...", "saturated=0.35 normalize
equalize");
run("Size...", "width=483 height=493 average
interpolation=None");

rename(name);
saveAs("PNG", dirout+name+".png");
run("Select All");
run("Copy");
run("Internal Clipboard");
rename(name+"color");
run("physics");

run("RGB Color");

setColor(255, 255, 255);
setFont("SansSerif", 40, " antialiased");
drawString(name, 360, 40);
saveAs("PNG", dirout+name+"color.png");
close();
close();
```

11 References

[1] A. L. Gray, *Analyst* **1985**, *110*, 551–556.
[2] S. E. Jackson, H. P. Longerich, G. R. Dunning, B. J. Fryer, *Can Mineral* **1992**, *30*, 1049–1064.
[3] B. J. Fryer, S. E. Jackson, H. P. Longerich, *Can Mineral* **1995**, *33*, 303–312.
[4] D. Günther, R. Frischknecht, C. A. Heinrich, H.-J. Kahlert, *J. Anal. At. Spectrom.* **1997**, *12*, 939–944.
[5] S. M. Eggins, L. P. J. Kinsley, J. M. G. Shelley, *Applied Surface Science* **1998**, *127-129*, 278–286.
[6] M. Guillong, I. Horn, D. Günther, *Journal of Analytical Atomic Spectrometry* **2003**, *18*, 1224.
[7] M. Guillong, D. Günther, *J. Anal. At. Spectrom.* **2002**, *17*, 831–837.
[8] D. B. Aeschliman, S. J. Bajic, D. P. Baldwin, R. S. Houk, *J. Anal. At. Spectrom.* **2003**, *18*, 1008.
[9] J. Koch, D. Günther, *Appl. Spectrosc.* **2011**, *65*, 155A–162A.
[10] V. Margetic, A. Pakulev, A. Stockhaus, M. Bolshov, K. Niemax, R. Hergenröder, *Spectrochimica Acta Part B: Atomic Spectroscopy* **2000**, *55*, 1771–1785.
[11] I. Horn, F. von Blanckenburg, R. Schoenberg, G. Steinhoefel, G. Markl, *Geochimica et Cosmochimica Acta* **2006**, *70*, 3677–3688.
[12] J. Koch, S. Schlamp, T. Rösgen, D. Fliegel, D. Günther, *Spectrochimica Acta Part B: Atomic Spectroscopy* **2007**, *62*, 20–29.
[13] J. Koch, M. Wälle, S. Schlamp, T. Rösgen, D. Günther, *Spectrochimica Acta Part B: Atomic Spectroscopy* **2008**, *63*, 37–41.
[14] J. Koch, S. Heiroth, T. Lippert, D. Günther, *Spectrochimica Acta Part B: Atomic Spectroscopy* **2010**, *65*, 943–949.
[15] C. C. Garcia, H. Lindner, K. Niemax, *Spectrochimica Acta Part B: Atomic Spectroscopy* **2007**, *62*, 13–19.
[16] C. C. Garcia, M. Wälle, H. Lindner, J. Koch, K. Niemax, D. Günther, *Spectrochimica Acta Part B: Atomic Spectroscopy* **2008**, *63*, 271–276.
[17] J. Koch, M. Wälle, R. Dietiker, D. Günther, *Analytical chemistry* **2008**, *80*, 915–921.
[18] S. F. Durrant, *J. Anal. At. Spectrom.* **1999**, *14*, 1385–1403.
[19] A. Plotnikov, C. Vogt, K. Wetzig, *J. Anal. At. Spectrom.* **2002**, *17*, 1114–1120.
[20] G. Fontaine, K. Hametner, A. Peretti, D. Günther, *ABC* **2010**, DOI 10.1007/s00216-010-4245-z.
[21] J. M. Cottle, M. S. A. Horstwood, R. R. Parrish, *J. Anal. At. Spectrom.* **2009**, *24*, 1355–1363.
[22] J. Wirth, S. Poletti, B. Aeschlimann, N. Yakandawala, B. Drosse, S. Osorio, T. Tohge, A. R. Fernie, D. Günther, W. Gruissem, et al., *Plant Biotechnology Journal* **2009**, *7*, 631–644.
[23] D. J. Sinclair, L. P. J. Kinsley, M. T. McCulloch, *Geochimica et Cosmochimica Acta* **1998**, *62*, 1889–1901.
[24] A. J. Campbell, M. Humayun, *Analytical Chemistry* **1999**, *71*, 939–946.
[25] M. Bi, A. M. Ruiz, I. Gornushkin, B. W. Smith, J. D. Winefordner, *Applied Surface Science* **2000**, *158*, 197–204.
[26] A. Raab, B. Ploselli, C. Munro, J. Thomas-Oates, J. Feldmann, *ELECTROPHOR* **2009**, *30*, 303–314.
[27] P. Treble, J. M. G. Shelley, J. Chappell, *Earth and Planetary Science Letters* **2003**, *216*, 141–153.

[28] D. Mattey, D. Lowry, J. Duffet, R. Fisher, E. Hodge, S. Frisia, *Earth and Planetary Science Letters* **2008**, *269*, 80–95.
[29] P. C. Treble, J. Chappell, J. M. G. Shelley, *Geochimica et Cosmochimica Acta* **2005**, *69*, 4855–4863.
[30] J. S. Becker, M. V. Zoriy, C. Pickhardt, N. Palomero-Gallagher, K. Zilles, *Anal. Chem.* **2005**, *77*, 3208–3216.
[31] J. D. Woodhead, J. Hellstrom, J. M. Hergt, A. Greig, R. Maas, *Geostand Geoanalyt Res* **2007**, *31*, 331–343.
[32] M. Thompson, J. E. Goulter, F. Sieper, *The Analyst* **1981**, *106*, 32.
[33] J. W. Carr, G. Horlick, *Spectrochimica Acta Part B: Atomic Spectroscopy* **1982**, *37*, 1–15.
[34] T. Ishizuka, Y. Uwamino, *Spectrochimica Acta Part B: Atomic Spectroscopy* **1983**, *38*, 519–527.
[35] P. Arrowsmith, *Anal. Chem.* **1987**, *59*, 1437–1444.
[36] P. Arrowsmith, S. K. Hughes, *Appl. Spec.* **1988**, *42*, 1231–1239.
[37] C. Geertsen, A. Briand, F. Chartier, J.-L. Lacour, P. Mauchien, S. Sjöström, J.-M. Mermet, *J. Anal. At. Spectrom.* **1994**, *9*, 17–22.
[38] T. E. Jeffries, W. T. Perkins, N. J. G. Pearce, *The Analyst* **1995**, *120*, 1365.
[39] S. Shuttleworth, *Applied Surface Science* **1996**, *96-98*, 513–517.
[40] A. J. G. Mank, P. R. D. Mason, *J. Anal. At. Spectrom.* **1999**, *14*, 1143–1153.
[41] I. Horn, M. Guillong, D. Günther, *Applied Surface Science* **2001**, *182*, 91–102.
[42] D. Günther, C. A. Heinrich, *Journal of Analytical Atomic Spectrometry* **1999**, *14*, 1363–1368.
[43] M. Guillong, C. A. Heinrich, *Journal of Analytical Atomic Spectrometry* **2007**, *22*, 1488.
[44] P. M. Outridge, W. Doherty, D. C. Gregoire, *Spectrochimica Acta Part B: Atomic Spectroscopy* **1996**, *51*, 1451–1462.
[45] Z. Chen, *Journal of Analytical Atomic Spectrometry* **1999**, *14*, 1823–1828.
[46] D. J. Figg, J. B. Cross, C. Brink, *Applied Surface Science* **1998**, *127–129*, 287–291.
[47] D. Günther, S. E. Jackson, H. P. Longerich, *Spectrochimica Acta Part B: Atomic Spectroscopy* **1999**, *54*, 381–409.
[48] H. P. Longerich, D. Günther, S. E. Jackson, *Analytical and Bioanalytical Chemistry* **1996**, *355*, 538–542.
[49] H.-R. Kuhn, D. Günther, *Anal. Chem.* **2003**, *75*, 747–753.
[50] S. E. Jackson, D. Günther, *Journal of Analytical Atomic Spectrometry* **2003**, *18*, 205–212.
[51] J. Košler, M. Wiedenbeck, R. Wirth, J. Hovorka, P. Sylvester, J. Míková, *J. Anal. At. Spectrom.* **2005**, *20*, 402–409.
[52] I. Kroslakova, D. Günther, *Journal of Analytical Atomic Spectrometry* **2007**, *22*, 51.
[53] R. E. Russo, X. L. Mao, O. V. Borisov, H. Liu, *J. Anal. At. Spectrom.* **2000**, *15*, 1115–1120.
[54] Q. Z. Bian, J. Koch, H. Lindner, H. Berndt, R. Hergenröder, K. Niemax, *Journal of Analytical Atomic Spectrometry* **2005**, *20*, 736.
[55] Q. Bian, C. C. Garcia, J. Koch, K. Niemax, *Journal of Analytical Atomic Spectrometry* **2006**, *21*, 187.
[56] V. Mozna, J. Pisonero, M. Hola, V. Kanicky, D. Günther, *Journal of Analytical Atomic Spectrometry* **2006**, *21*, 1194.
[57] H. Wiltsche, D. Günther, *ABC* **2010**, *399*, 2167–2174.
[58] R. E. Russo, X. Mao, J. J. Gonzalez, S. S. Mao, *Journal of Analytical Atomic Spectrometry* **2002**, *17*, 1072–1075.

[59] K. Birbaum, Capabilities and Limitations of Inductively Coupled Plasma Mass Spectrometry-analyses on Engineered and Laser-generated Nanoparticles, ETH Zurich, **2011**.
[60] R. Glaus, R. Kaegi, F. Krumeich, D. Günther, *Spectrochimica Acta Part B: Atomic Spectroscopy* **September**, *65*, 812–822.
[61] R. E. Russo, X. Mao, H. Liu, J. Gonzalez, S. S. Mao, *Talanta* **2002**, *57*, 425–451.
[62] M. Guillong, D. Günther, *Spectrochimica Acta Part B: Atomic Spectroscopy* **2001**, *56*, 1219–1231.
[63] A. M. Leach, G. M. Hieftje, *Journal of Analytical Atomic Spectrometry* **2002**, *17*, 852–857.
[64] M. Tanner, D. Günther, *J. Anal. At. Spectrom.* **2005**, *20*, 987–989.
[65] A. Malsy, L. Klemm, *CHIMIA International Journal for Chemistry* **2010**, *64*, 741–746.
[66] H. P. Longerich, S. E. Jackson, D. Günther, *J. Anal. At. Spectrom.* **1996**, *11*, 899–904.
[67] A. M. Leach, G. M. Hieftje, *Anal. Chem.* **2001**, *73*, 2959–2967.
[68] M. Guillong, K. Hametner, E. Reusser, S. A. Wilson, D. Guenther, *Geostandards and Geoanalytical Research* **2005**, *29*, 315–331.
[69] L. Chen, Y. Liu, Z. Hu, S. Gao, K. Zong, H. Chen, *Chemical Geology* **2011**, *284*, 283–295.
[70] M. S. Roberts, P. L. Smart, C. J. Hawkesworth, W. T. Perkins, N. J. G. Pearce, *The Holocene* **1999**, *9*, 707–713.
[71] M. Sanborn, K. Telmer, *J. Anal. At. Spectrom.* **2003**, *18*, 1231–1237.
[72] R. Kovacs, D. Günther, *J. Anal. At. Spectrom.* **2008**, *23*, 1247–1252.
[73] D. A. Frick, D. Günther, *Journal of Analytical Atomic Spectrometry* **2012**, *27*, 1294.
[74] J. Feldmann, A. Kindness, P. Ek, *J. Anal. At. Spectrom.* **2002**, *17*, 813–818.
[75] A. Plotnikov, C. Vogt, V. Hoffmann, C. Taschner, K. Wetzig, *J. Anal. At. Spectrom.* **2001**, *16*, 1290–1295.
[76] J. Pisonero, J. Koch, M. Wälle, W. Hartung, N. D. Spencer, D. Günther, *Anal. Chem.* **2007**, *79*, 2325–2333.
[77] W. Schrön, G. Bombach, P. Beuge, *Spectrochimica Acta Part B: Atomic Spectroscopy* **1983**, *38*, 1269–1276.
[78] W. Müller, M. Shelley, P. Miller, S. Broude, *J. Anal. At. Spectrom.* **2009**, *24*, 209–214.
[79] T. E. Cerling, Z. D. Sharp, *Palaeogeography, Palaeoclimatology, Palaeoecology* **1996**, *126*, 173–186.
[80] Y. Liu, Z. Hu, H. Yuan, S. Hu, H. Cheng, *J. Anal. At. Spectrom.* **2007**, *22*, 582–585.
[81] D. Bleiner, D. Gunther, *J. Anal. At. Spectrom.* **2001**, *16*, 449–456.
[82] D. Bleiner, H. Altorfer, *J. Anal. At. Spectrom.* **2005**, *20*, 754–756.
[83] D. Monticelli, E. L. Gurevich, R. Hergenroder, *J. Anal. At. Spectrom.* **2009**, *24*, 328–335.
[84] J. Pisonero, D. Fliegel, D. Gunther, *J. Anal. At. Spectrom.* **2006**, *21*, 922–931.
[85] H. Lindner, D. Autrique, J. Pisonero, D. Gunther, A. Bogaerts, *J. Anal. At. Spectrom.* **2010**, *25*, 295–304.
[86] E. L. Gurevich, R. Hergenroder, *J. Anal. At. Spectrom.* **2007**, *22*, 1043–1050.
[87] M. S. A. Horstwood, G. L. Foster, R. R. Parrish, S. R. Noble, G. M. Nowell, *J. Anal. At. Spectrom.* **2003**, *18*, 837–846.
[88] M. Tanner, Fundamental Studies on Fast Signal Generation Without an Aerosol Transport System for Laser Ablation Inductively Coupled Plasma Mass Spectrometry, DISS. ETH NO. 17456, ETH Zurich, **2007**.

[89] M. Tanner, D. Günther, *J. Anal. At. Spectrom.* **2006**, *21*, 941–947.
[90] D. Günther, M. Gäckle, *Z. Chem.* **1988**, *28*, 227–228.
[91] W. Devos, C. Moor, P. Lienemann, *J. Anal. At. Spectrom.* **1999**, *14*, 621–626.
[92] B. Wagner, W. Jędral, *J. Anal. At. Spectrom.* **2011**, DOI 10.1039/c1ja10137d.
[93] D. Asogan, B. L. Sharp, C. J. P. O. Connor, D. A. Green, R. W. Hutchinson, *J. Anal. At. Spectrom.* **2009**, *24*, 917–923.
[94] R. Kovacs, K. Nishiguchi, K. Utani, D. Günther, *J. Anal. At. Spectrom.* **2010**, *25*, 142.
[95] D. Tabersky, I. de Maddalena, M. B. Fricker, R. Dietiker, D. Günther, **2012**.
[96] I. Feldmann, C. U. Koehler, P. H. Roos, N. Jakubowski, *J. Anal. At. Spectrom.* **2006**, *21*, 1006.
[97] H. Reinhardt, M. Kriews, H. Miller, O. Schrems, C. Lüdke, E. Hoffmann, J. Skole, *Fresenius' Journal of Analytical Chemistry* **2001**, *370*, 629–636.
[98] H. Reinhardt, M. Kriews, H. Miller, C. Lüdke, E. Hoffmann, J. Skole, *Analytical and Bioanalytical Chemistry* **2003**, *375*, 1265–1275.
[99] W. Müller, J. M. G. Shelley, S. O. Rasmussen, *J. Anal. At. Spectrom.* **2011**, DOI 10.1039/C1JA10242G.
[100] J. Gonzalez, D. D. Oropeza, X. Mao, H. P. Longerich, R. E. Russo, *J. Anal. At. Spectrom.* **2012**, DOI 10.1039/C2JA10368K.
[101] "RESONETICS," can be found under http://www.resonetics.com/la/?p=prod_fets, **2012**.
[102] "New Wave Research," can be found under http://www.esi.com/Products/NewWaveResearch/LaserAblation/SampleChambers.aspx, **2012**.
[103] "CETAC," can be found under http://www.cetac.com/laser_ablation/samplecells.asp, **2012**.
[104] G. Carugati, S. Rauch, M. E. Kylander, *Microchim Acta* **2010**, *170*, 39–45.
[105] M. B. Fricker, D. Kutscher, B. Aeschlimann, J. Frommer, R. Dietiker, J. Bettmer, D. Günther, *International Journal of Mass Spectrometry* **2011**, *307*, 39–45.
[106] ANSYS® Academic Research, *Release 12.1, CFX, ANSYS, Inc.* **2009**.
[107] D. Bleiner, A. Bogaerts, *Spectrochimica Acta Part B: Atomic Spectroscopy* **2007**, *62*, 155–168.
[108] D. Autrique, A. Bogaerts, H. Lindner, C. C. Garcia, K. Niemax, *Spectrochimica Acta Part B: Atomic Spectroscopy* **2008**, *63*, 257–270.
[109] B. Hattendorf, Ion Molecule Reactions for the Suppression of Spectral Interferences in Elemental Analysis by Inductively Coupled Plasma Mass Spectrometry, DISS. ETH NO. 14926, **2002**.
[110] Z. Hu, Y. Liu, S. Gao, S. Hu, R. Dietiker, D. Günther, *J. Anal. At. Spectrom.* **2008**, *23*, 1192–1203.
[111] D. Bleiner, A. Bogaerts, *J. Anal. At. Spectrom.* **2006**, *21*, 1161.
[112] M. Aghaei, H. Lindner, A. Bogaerts, *J. Anal. At. Spectrom.* **2012**, DOI 10.1039/C2JA10341A.
[113] J. Triglav, J. T. van Elteren, V. S. Selih, *Analytical Chemistry* **2010**, *82*, 8153–8160.
[114] J. Lear, D. Hare, P. Adlard, D. Finkelstein, P. Doble, *J. Anal. At. Spectrom.* **2011**, DOI 10.1039/C1JA10301F.
[115] G. A. Jenner, H. P. Longerich, S. E. Jackson, B. J. Fryer, *Chemical Geology* **1990**, *83*, 133–148.
[116] B. Hattendorf, C. Latkoczy, D. Günther, *Anal. Chem.* **2003**, *75*, 341 A–347 A.
[117] H. P. Longerich, *J. Anal. At. Spectrom.* **2012**, *27*, 1181.

[118] R. S. Houk, V. A. Fassel, G. D. Flesch, H. J. Svec, A. L. Gray, C. E. Taylor, *Anal. Chem.* **1980**, *52*, 2283–2289.
[119] A. N. Halliday, D.-C. Lee, J. N. Christensen, M. Rehkämper, W. Yi, X. Luo, C. M. Hall, C. J. Ballentine, T. Pettke, C. Stirling, *Geochimica et Cosmochimica Acta* **1998**, *62*, 919–940.
[120] J. Mattauch, R. Herzog, *Z. Phys.* **1934**, *89*, 786–795.
[121] G. D. Schilling, S. J. Ray, A. A. Rubinshtein, J. A. Felton, R. P. Sperline, M. B. Denton, C. J. Barinaga, D. W. Koppenaal, G. M. Hieftje, *Analytical Chemistry* **2009**, *81*, 5467–5473.
[122] J. A. Felton, G. D. Schilling, S. J. Ray, R. P. Sperline, M. B. Denton, C. J. Barinaga, D. W. Koppenaal, G. M. Hieftje, *Journal of Analytical Atomic Spectrometry* **2011**, *26*, 300.
[123] M. Resano, K. S. McIntosh, F. Vanhaecke, *J. Anal. At. Spectrom.* **2011**, DOI 10.1039/C1JA10193E.
[124] D. A. Frick, *in prep.* **2012**, DOI in prep.
[125] D. P. Myers, G. M. Hieftje, *Microchemical Journal* **1993**, *48*, 259–277.
[126] P. P. Mahoney, G. Li, G. M. Hieftje, *Journal of Analytical Atomic Spectrometry* **1996**, *11*, 401.
[127] M. Guilhaus, *Spectrochimica Acta Part B: Atomic Spectroscopy* **2000**, *55*, 1511–1525.
[128] O. Borovinskaya, *in.prep.* **2012**, DOI in.prep.
[129] T. Jilbert, G.-J. Reichart, B. Aeschlimann, D. Günther, W. Boer, G. de Lange, *Geology* **2010**, *38*, 19–22.
[130] R. Ma, C. W. McLeod, K. Tomlinson, R. K. Poole, *Electrophoresis* **2004**, *25*, 2469–2477.
[131] S. J. Becker, R. Lobinski, J. Sabine Becker, *Metallomics* **2009**, *1*, 312.
[132] M. Tanner, D. Günther, *Anal Bioanal Chem* **2008**, *391*, 1211–1220.
[133] H. Lindner, D. Autrique, C. C. Garcia, K. Niemax, A. Bogaerts, *Analytical Chemistry* **2009**, *81*, 4241–4248.
[134] D. Pozebon, V. L. Dressler, M. F. Mesko, A. Matusch, J. S. Becker, *J. Anal. At. Spectrom.* **2010**, *25*, 1739–1744.
[135] M. Senoner, T. Wirth, W. E. S. Unger, *J. Anal. At. Spectrom.* **2010**, *25*, 1440.
[136] D. J. Kutscher, M. E. del Castillo Busto, N. Zinn, A. Sanz-Medel, J. Bettmer, *J. Anal. At. Spectrom.* **2008**, *23*, 1359–1364.
[137] T. Pettke, C. Heinrich, A. Ciocan, D. Günther, *J. Anal. At. Spectrom* **2000**, *15*, 1149–1155.
[138] T. Hirata, *Anal. Sci.* **2007**, *23*, 1195–1201.
[139] J. A. Saba, X. Shen, J. C. Jamieson, H. Perreault, *J. Mass Spectrom.* **2001**, *36*, 563–574.
[140] J.-L. Todoli, J.-M. Mermet, *Spectrochimica Acta Part B: Atomic Spectroscopy* **1998**, *53*, 1645–1656.
[141] F. Vanhaecke, M. Resano, J. Koch, K. McIntosh, D. Günther, *J. Anal. At. Spectrom.* **2010**, *25*, 1259–1267.
[142] P. Sylvester, Ed., *Laser Ablation–ICP–MS in the Earth Sciences, PRINCIPLES AND APPLICATIONS*, Mineralogical Association Of Canada, Short Course 29, **2001**.
[143] P. Sylvester, Ed., *Laser Ablation–ICP–MS in the Earth Sciences, CURRENT PRACTICES AND OUTSTANDING ISSUES*, Mineralogical Association Of Canada, Short Course 40, **2008**.
[144] C. Paton, J. Hellstrom, B. Paul, J. Woodhead, J. Hergt, *Journal of Analytical Atomic Spectrometry* **2011**, *26*, 2508–2518.

[145] T. Osterholt, D. Salber, A. Matusch, J. S. Becker, C. Palm, *International Journal of Mass Spectrometry* **2011**, *307*, 232–239.
[146] L. A. Solari, M. Tanner, *Revista mexicana de ciencias geológicas* **2011**, *28*, 83–91.
[147] T. Parkin, *Python 2.6*, Python Software Foundation, Http://www.python.org/, **2012**.
[148] S. E. Jackson, *LAMTRACE user manual* **2005**, Department of Earth and Planetary Sciences, Macquarie University, Australia.
[149] L. Halicz, D. Günther, *J. Anal. At. Spectrom.* **2004**, *19*, 1539–1545.
[150] *Fiji*, http://fiji.sc/wiki/index.php/Fiji, **2012**.
[151] W. S. Rasband, *ImageJ 1.45s*, U.S. National Institutes Of Health, Bethesda, Maryland, USA, Http://imagej.nih.gov/ij/, **1997**.
[152] T. Vaculovic, T. Warchilova, T. Simo, O. Matal, V. Otruba, P. Mikuska, V. Kanicky, *J. Anal. At. Spectrom.* **2012**, DOI 10.1039/C2JA30037K.
[153] B. Paul, C. Paton, A. Norris, J. Woodhead, J. Hellstrom, J. Hergt, A. Greig, *J. Anal. At. Spectrom.* **2012**, DOI 10.1039/C2JA10383D.
[154] P. S. Garofalo, M. B. Fricker, D. Günther, P. Forti, A.-M. Mercuri, M. Loreti, B. Capaccioni, *Earth and Planetary Science Letters* **2010**, *289*, 560–569.
[155] M. B. Fricker, P. S. Garofalo, D. Günther, *CHIMIA International Journal for Chemistry* **2011**, *65*, 620.
[156] "Industrias Peñoles S. A. B.," can be found under http://www.penoles.com.mx, **2012**.
[157] G. Badino, "La Venta Esplorazioni Geografiche," can be found under http://www.laventa.it/index.php?lang=en, **2011**.
[158] "Naica Project," can be found under http://naica.com.mx/english/index.htm, **2012**.
[159] "CProducciones," can be found under http://merhill.com/mexicoantiguo/english/index.htm, **2009**.
[160] G. Giovine, G. Badino, A. De Vivo, F. Lomastro, G. Casagrande, A. Davila, G. Gonzalez Hidalgo, in *2009 ICS Proceedings*, **2009**, pp. 1980–1984.
[161] E. Roedder, *Fluid Inclusions*, Mineralogical Society Of America, Washington, D. C., USA, **1984**.
[162] R. J. Bodnar, in *Fluid Inclusions, Analysis and Interpretation*, Mineralogical Association Of Canada, Short Course 32, Vancouver, B.C., **2003**, pp. 1–8.
[163] T. J. Shepherd, A. H. Rankin, D. H. M. Alderton, *A Practical Guide to Fluid Inclusion Studies*, Blackie & Son Limited, **1985**.
[164] R. C. Burruss, in *Fluid Inclusions, Analysis and Interpretation*, Mineralogical Association Of Canada, Short Course 32, Vancouver, B.C., **2003**, pp. 279–290.
[165] S. Salvi, A. E. Williams-Jones, in *Fluid Inclusions, Analysis and Interpretation*, Mineralogical Association Of Canada, Short Course 32, Vancouver, B.C., **2003**, pp. 247–278.
[166] D. Derome, M. Cathelineau, C. Fabre, M.-C. Boiron, D. Banks, T. Lhomme, M. Cuney, *Chemical Geology* **2007**, *237*, 240–254.
[167] D. Günther, in *Laser Ablation–ICP–MS in the Earth Sciences, PRINCIPLES AND APPLICATIONS*, Mineralogical Association Of Canada, Short Course 29, Victoria, B. C., **2001**, pp. 47–61.
[168] J. E. Gagnon, I. Samson, B. J. Fryer, in *Fluid Inclusions, Analysis and Interpretation*, Mineralogical Association Of Canada, Short Course 32, Vancouver, B.C., **2003**, pp. 291–318.
[169] M. Aerts, A. C. Hack, E. Reusser, P. Ulmer, *AMERICAN MINERALOGIST* **2010**, *95*, 1523–1526.
[170] T. Pettke, W. E. Halter, J. D. Webster, M. Aigner-Torres, C. A. Heinrich, *Lithos* **2004**, *78*, 333–361.
[171] M. Guillong, T. Pettke, *J. Anal. At. Spectrom.* **2012**, DOI 10.1039/C2JA10147E.

[172] P. Forti, E. Galli, A. Rossi, *Acta Carsologica* **2007**, *36*, 379–388.
[173] D. Günther, A. Audétat, R. Frischknecht, C. A. Heinrich, *J. Anal. At. Spectrom.* **1998**, *13*, 263–270.
[174] C. A. Heinrich, T. Pettke, W. E. Halter, M. Aigner-Torres, D. Günther, B. Hattendorf, D. Bleiner, M. Guillong, I. Horn, A. Audétat, *Geochim. Cosmochim. Acta* **2003**, *67*, 3473–3497.
[175] W. E. Halter, T. Pettke, C. A. Heinrich, B. Rothen-Rutishauser, *Chemical Geology* **2002**, *183*, 63–86.
[176] S.-E. Lauritzen, in *International Geological Conference*, Oslo, Norway, **2008**.
[177] Y. Yechieli, A. Starinsky, E. Rosenthal, *Applied Geochemistry* **1992**, *7*, 361–374.
[178] S. Metcalfe, A. Say, S. Black, R. McCulloch, S. O'Hara, *Quaternary Research* **2002**, *57*, 91–101.
[179] L. Sanna, F. Saez, S. Simonsen, S. Constantin, J. M. Calaforra, P. Forti, S.-E. Lauritzen, *International Journal of Speleology* **2010**, *39*, 35–46.
[180] L. C. Peterson, G. H. Haug, K. A. Hughen, U. Röhl, *Science* **2000**, *290*, 1947–1951.
[181] G. H. Haug, D. Günther, L. C. Peterson, D. M. Sigman, K. A. Hughen, B. Aeschlimann, *Science* **2003**, *299*, 1731–1735.
[182] D. S. Gholap, A. Izmer, B. De Samber, J. T. van Elteren, V. S. Šelih, R. Evens, K. De Schamphelaere, C. Janssen, L. Balcaen, I. Lindemann, et al., *Analytica Chimica Acta* **2010**, *664*, 19–26.
[183] H. A. O. Wang, D. Grolimund, L. R. Van Loon, K. Barmettler, C. N. Borca, B. Aeschlimann, D. Gunther, *Anal. Chem.* **2011**, *83*, 6259–6266.
[184] Roentgenanalytik Systeme GmbH & Co. KG, **2010**.
[185] E. F. Stoermer, M. B. Edlund, C. H. Pilskaln, C. L. Schelske, *Journal of Paleolimnology* **1995**, *14*, 69–82.
[186] D. J. Conley, R. W. Johnstone, *Mar Ecol Prog Ser* **1995**, *122*, 265–276.
[187] Federal Office of Meteorology and Climatology, "MeteoSwiss temperatures Fluntern, Zurich, Switzerland," can be found under http://www.meteoschweiz.admin.ch/web/de/klima/klima_heute/homogene_reihen.Par.0046.DownloadFile.ext.tmp/zuerich.txt, **2012**.
[188] G. Friedl, *EAWAGnews* **2001**, *52*.
[189] I. J. Fairchild, C. L. Smith, A. Baker, L. Fuller, C. Spötl, D. Mattey, F. McDermott, E.I.M.F., *Earth-Science Reviews* **2006**, *75*, 105–153.
[190] F. McDermott, *Quaternary Science Reviews* **2004**, *23*, 901–918.
[191] S. Breitenbach, Changes in Monsoonal Precipitation and Atmospheric Circulation During the Holocene Reconstructed from Stalagmites from Northeastern India, University of Potsdam, **2009**.
[192] K. P. Jochum, "GeoReM," can be found under http://georem.mpch-mainz.gwdg.de/, **2012**.
[193] M. Anklin, J. Barnola, J. Beer, T. Blunier, J. Chappellaz, H. Clausen, D. Dahljensen, W. Dansgaard, M. Deangelis, R. Delmas, et al., *Nature* **1993**, *364*, 203–207.
[194] "Greenland Icecore Project," can be found under http://www.iceandclimate.nbi.ku.dk/research/drill_analysing/history_drilling/central_ice_cores/, **1993**.
[195] J. Laskar, "Compute insolation quantities derived from the orbital and precessional quantities," can be found under http://www.imcce.fr/Equipes/ASD/insola/earth/online/index.php, **2010**.
[196] S. F. M. Breitenbach, J. F. Adkins, H. Meyer, N. Marwan, K. K. Kumar, G. H. Haug, *Earth and Planetary Science Letters* **2010**, *292*, 212–220.

[197] J. Laskar, P. Robutel, F. Joutel, M. Gastineau, A. C. M. Correia, B. Levrard, *Astronomy and Astrophysics* **2004**, *428*, 261–285.
[198] D. Yuan, H. Cheng, R. L. Edwards, C. A. Dykoski, M. J. Kelly, M. Zhang, J. Qing, Y. Lin, Y. Wang, J. Wu, et al., *Science* **2004**, *304*, 575–578.
[199] A. Lückge, H. Doose-Rolinski, A. A. Khan, H. Schulz, U. von Rad, *Palaeogeography,Palaeoclimatology,Palaeoecology* **2001**, *167*, 273–286.
[200] M. Staubwasser, H. Weiss, *Quaternary Research* **2006**, *66*, 372–387.
[201] "Global Volcanism Program," can be found under http://www.volcano.si.edu/world/largeeruptions.cfm, **2007**.
[202] C. Gao, A. Robock, C. Ammann, *J. Geophys. Res.* **2008**, *113*, 15 PP.
[203] E. Strack, *Pearls*, Rühle - Diebener Verlag, Stuttgart, Germany, **2001**.
[204] K. Schlossmacher, *Edelsteine und Perlen*, E. Schweizerbart'sche Verlagsbuchhandlung (Nägele U. Obermiller), Stutt, **1969**.
[205] Y. Dauphin, A. Ball, M. Cotte, J.-P. Cuif, A. Meibom, M. Salomé, J. Susini, C. Williams, *Analytical and Bioanalytical Chemistry* **2008**, *390*, 1659–1669.
[206] Y. Dauphin, P. Gautret, J. P. Cuif, *Bull. Soc. Geol. Fr.* **1996**, *167*, 247–256.
[207] F. Chang, G. Li, M. Haws, T. Niu, *Food Chemistry* **2007**, *104*, 1171–1176.
[208] J. D. Milliman, in *Marine Carbonates*, Springer-Verlag, Berlin Heidelberg New York, **1974**, pp. 107–108.
[209] P. M. Outridge, G. Veinott, R. D. Evans, *Environ. Rev.* **1995**, *3*, 160–170.
[210] R. A. Lutz, D. C. Rhoads, in *Skeletal Growth of Aquatic Organisms*, Plenum Press, New York and London, **1980**, pp. 203–254.
[211] G. D. Schilling, F. J. Andrade, Barnes, R. P. Sperline, M. B. Denton, C. J. Barinaga, D. W. Koppenaal, G. M. Hieftje, *Analytical Chemistry* **2007**, *79*, 7662–7668.
[212] E. Moreno-Gordaliza, D. Esteban-Fernández, C. Giesen, K. Lehmann, A. Lázaro, A. Tejedor, C. Scheler, B. Cañas, N. Jakubowski, M. Linscheid, et al., *J. Anal. At. Spectrom.* **2012**, DOI 10.1039/C2JA30016H.
[213] R. Glaus, J. Koch, D. Günther, *Anal. Chem.* **2012**, DOI 10.1021/ac3008626.